12-15-2014

Comprehensive Joint Time-Frequency Analysis Toward Condition Based Maintenance Regimes for Electrical and Mechanical Components

David Lee Coats
University of South Carolina - Columbia

Comprehensive Joint Time-Frequency Analysis toward Condition Based Maintenance Regimes for Electrical and Mechanical Components

by

David Lee Coats

Bachelor of Science
University of South Carolina, 2009

Master of Engineering
University of South Carolina, 2012

Submitted in Partial Fulfillment of the Requirements

for the Degree of Doctor of Philosophy in

Electrical Engineering

College of Engineering and Computing

University of South Carolina

2014

Accepted by:

Yong-June Shin, Major Professor

Mohammod Ali, Committee Member

Roger Dougal, Committee Member

Abdel-Moez Bayoumi, Committee Member

Lacy Ford, Vice Provost and Dean of Graduate Studies

DEDICATION

To my wife Bianca and my parents Eddie and Faye for all of their support.

ACKNOWLEDGMENTS

I would like to thank all of those who took time to help me. A special thanks goes to my advisor Dr. Yong-June Shin who approached me with a topic of research while I was still an undergraduate, enabled many defining research experiences of my graduate career including technical conferences and research trips, guided me along in my studies and research, provided an opportunity to travel to the Republic of Korea and continue research with international collaboration, and helped me in the arduous process of completing this dissertation document. Dr. Abdel-Moez Bayoumi also supported me from the start of my research contributing full access to the resources and teststand of the CBM@USC research center, academic, financial, and moral support for attending a number of conferences and presentations, and most of all an attitude of intellectual collaboration in interdisciplinary research. Both professors along with Drs. Koley and Dougal, were instrumental in my receiving the National Science Foundation Graduate Research Fellowship who by providing their supervision and reference letters. I would also like to thank Dr. Mohammod Ali who served as my advisor locally when Dr. Shin pursued expanded research opportunities at Yonsei University. I would additionally like to thank Drs. Dougal, Ali, Shin, and Bayoumi for participating in my dissertation committee and mentoring me in the formative stages of my dissertation.

I would like to thank the members of the Power IT group both in South Carolina and in South Korea. I would like to thank Drs. Phillip E. C. Stone and Jing Jiang Wang for helping me out in my first studies. I also thank Dr. Bin Zhang for the use of his lab space, tutorials in psuedo-noise generation, and motivational discussions in the laboratory. Patrick Mitchell, Nazmul Alam, Major Kwangik Cho, Chunkwon Lee, and Mohammed Hassan

have been some of my closest collaborators. Moinul Islam, Qiu Deng, Paul Young, Cuong Nguyen, Ryan Lukens, Hossein Ali Mohammedpour, Amin Ghaderi, and John Abrams were all members of the same research team and gave me helpful advice and suggestions throughout my studies. In South Korea, I would like to thank Chun Ku Lee, Sin Ho Lee, Seung Jin Chang, Jong Min Jeong, Han Sol Kim, and Chunkwon Lee of Power IT group. I would like to thank Jin Bae Park at Yonsei University for sponsoring me for my visit in 2013. I would like to thank all CBM staff: General Lester Eisner, Lemuel Grant, Tim Cook, Adam Miracle, Nick Goodman, Lee Goodman, Tanzina Zaman, Andrew Patterson, Jake McVay, Travis Edwards, Huston Bokinsky, Rhea McCaslin, Erin Ballentine, Thomas Hartmann, Alistair McNear, Alex Cao, and even Kareem Gouda. Last, but not least, I would like to thank all of my family and close friends who sacrificed time for me: my wife, Bianca, who helped read through my dissertation document and witnessed many practice presentations; my best friend, Will, who helped me focus; my two sisters, Mary Alice and Katie, who supported me and laughed with me and at me; my parents who always trusted me.

The projects that make up this dissertation document have been supported in part by the U.S. Office of Naval Research, Electric Ship Research and Development Consortium (ESRDC) under Grant #N00014-00-0368 and also by the National Science Foundation under Grant #0747681, "CAREER: Diagnostics and Prognostics of Electric Cables in Aging Power Infrastructure." Segments of this work accomplished in South Korea were supported by the National Research Foundation of Korea (NRF) grant funded by the Korean government (MEST) #2012-M2-A8A405236. This work is also supported by the NSF Graduate Research Fellowship Program (GFRP) in behalf of David Coats.

ABSTRACT

Based upon a framework of time-frequency analysis, we outline condition based maintenance (CBM), or maintenance only upon evidence of need, for both electrical and mechanical systems. We apply novel time-frequency cross-correlation metrics to helicopter drivetrain systems and electrical cables as remaining useful life assessments by non-destructive and non-invasive tests. In both cases, these metrics for health assessment provide a basis for diagnostic and prognostic analysis of underlying systems and components by performing accelerated condition tests on actual mechanical and electrical systems.

We present novel time-frequency domain vibration analysis of a gearbox failure in an AH-64 Apache drivetrain testbed and quantify transient precursors of failure where previous diagnostic methods rely on stationary power spectrum analysis to analyze non-stationary signals. Using time-frequency representations of the vibration signals, a shift in energy is seen from the first harmonic of the gearmesh frequency to the third and fourth harmonics in intermittent patterns indiscernible by the standard power spectrum over the course of 4 days leading to gearbox failure due to grease lubrication drought. We demonstrate a new form of Rényi entropy-based mutual information measure based upon Shannon and Hartley entropy and derived from a cross-time-frequency distribution of separate accelerometer vibration signals for comparing rotational harmonics from multiple bearings to create new condition indicators of damage in rotorcraft drivetrains. Baseline, unbalanced, and misaligned experimental settings of helicopter drivetrain bearings and shafts are quantitatively distinguished by the proposed techniques. With unbalance quantifiable by variance in the in-phase mutual information and misalignment quantifiable by variance in the quadrature mutual information, machine health classification is accomplished by use

of statistical bounding regions.

Utilizing similar methods to form a time-frequency cross-correlation derived metric, a process for non-invasively assessing the health of low voltage instrumentation cables and medium to high voltage feeder and underground transmission cables is proposed by way of Joint Time-frequency Domain Reflectometry (JTFDR). We introduce a new standardized method for determination of the optimal reference signal for reflectometry to allow implementation of a stand-alone reflectometer device for cable testing and provide theoretical background for a more generalized time-frequency enveloping function of this reference. Fault location and life estimation methods are verified in networks of instrumentation cable, cable tray and conduit systems, multiple localized fault scenarios, simulations of faults on endless lines, and three separate thermal accelerated aging tests of low to high voltage cables. A 24 hour thermal aging test of underground 15kV, tree-resistant cross-linked polyethylene (TR-XLPE) cable simulates 90 years of service life and shows a monotonic increase in the measured JTFDR metric. This is compared to aging of similar duration for other cables utilizing silicon rubber (SIR), cross-linked polyethylene (XLPE), and ethylene propylene rubber (EPR) insulation types. Expanding on this preliminary aging, we present a 916 hour extended accelerated aging test of XLPE insulated RG-58 instrumentation cable at reduced and more realistic temperatures to simulate 30 years of service. The time-frequency optimal reference signal is updated with a separated spectrum as enveloped by a Gaussian derivative function. Lastly, we utilize a single broadband monopole surface wave launcher and receiver in combination with the JTFDR algorithm to obtain fault location and health assessment metrics non-invasively and provide fault assessment in unshielded concentric neutral cables.

TABLE OF CONTENTS

DEDICATION iii

ACKNOWLEDGMENTS iv

ABSTRACT vi

LIST OF TABLES xi

LIST OF FIGURES xii

CHAPTER 1 INTRODUCTION 1

1.1 Preventative Maintenance Concept and Analysis 1

1.2 Health Monitoring of Rotorcraft Drivetrain 5

1.3 Health Monitoring of Electric Cable 9

1.4 Joint Time-Frequency Tools for Condition Based Maintenance 11

1.5 Summary of Original Contributions 16

1.6 Summary of Document Organization 18

CHAPTER 2 HEALTH MONITORING OF ELECTRICAL CABLE 20

2.1 Introduction and State of the Art 20

2.2 Experimental Setup 23

2.3 Joint Time-Frequency Domain Reflectometry Optimal Reference 24

2.4 Automated Selection of Optimal Reference by Fuzzy Logic Decision 27

2.5 Results Using Standardized Reference 31

2.6 Diagnostics and Prognostics 33

2.7 Practical Implementation of Time-Frequency Domain Reflectometry 39

2.8 Conclusion 45

CHAPTER 3 IMPEDANCE ASSESSMENT, FAULT SIMULATION, AND EXTENDED ACCELERATED AGING IN CABLE SAMPLES 46

3.1 Hard and Soft Faults 47

3.2 Variation of Reference Envelope 55

3.3 Improvements of Experimental Set-up 59

3.4 Imaging of Baseline and Aged Samples 62

3.5 Measuring and Monitoring Multiple Faults 65

3.6 Conclusion 66

CHAPTER 4 DESIGNING TIME-FREQUENCY DOMAIN REFLECTOMETRY SIGNAL FOR SURFACE WAVE PROPAGATION 67

4.1 Implementation of Time-Frequency Domain Reference in Dispersive Environments 67

4.2 Reference Signal for Surface Wave Propagation 68

4.3 Implementation of Cable Health Assessment by Surface Wave Injection . . 70

4.4 Surface Wave Implementation 72

4.5 Surface Wave Monitoring of Accelerated Thermal Aging Testing 74

4.6 Discussion and Summary 75

4.7 Conclusion 77

CHAPTER 5 HEALTH MONITORING OF ROTORCRAFT DRIVETRAIN BY MUTUAL INFORMATION 78

5.1 Introduction 78

5.2 Theory of Mutual Information for Condition Based Maintenance 86

5.3 Analysis of Hanger Bearing Vibration Signals in Tail Rotor Gearbox Case Study 89

5.4 Analysis of Hanger Bearing Vibration Signals in Baseline Measurements . . 95

5.5 Conclusions 101

BIBLIOGRAPHY 102

APPENDIX A SMART WIRING GUI OVERVIEW 110

APPENDIX B AUTOMATED DETERMINATION OF OPTIMAL REFERENCE - MEMBERSHIP FUNCTIONS FOR FUZZY LOGIC 113

LIST OF TABLES

Table 2.1 Summary of Inference Rules for Automated Optimal Reference Determination 30

Table 4.1 Explanation of sample peaks data 75

Table 5.1 Loading profile for a 30 minute baseline test run 79

Table 5.2 Tail Rotor Driveshaft Experimental Settings 82

Table 5.3 Rotating Frequencies of TRDT Components Provided by AED 90

Table 5.4 Statistical Summary of Mutual Information Measure 100

LIST OF FIGURES

Figure 1.1 Paradigm for Condition Based Maintenance in rotorcraft using vibration sensors, time-frequency analysis, and developing health and prognostic indicators. This is an example of the process for refining an existing prognostic and health monitoring system. 4

Figure 1.2 A typical legend for Condition Indicator (CI) status as shown in PC Ground Based Station (PC-GBS) fleet monitoring software for military rotorcraft. 6

Figure 1.3 An example of a rotorcraft component level CI statistical summary given by PC Ground Based Station (PC-GBS) showing component values. 7

Figure 1.4 Labeled picture of tail rotor drivetrain testbed at CBM Research Center at the University of South Carolina. 8

Figure 1.5 Cables damaged by corrosion and abrasion exposing shielding and insulation. 10

Figure 2.1 Experimental setup is shown with a (a) labeled figure of the laboratory setup and (b) a system function diagram 23

Figure 2.2 Time-frequency distribution of various optimal reference options with differing center frequency (CF), bandwidth (BW), sweeping frequency, and time duration (TD): (a) $CF = 175MHz$, $BW = 50MHz$, and $TD = 80ns$, (b) $CF = 175MHz$, $BW = 100MHz$, and $TD = 80ns$, (c) $CF = 175MHz$, $BW = 100MHz$, and $TD = 60ns$, and (d) $CF = 125MHz$, $BW = 100MHz$, and $TD = 60ns$ 26

Figure 2.3 The time-bandwidth product for a sweeping of the optimal reference signal in time duration and bandwidth (second moments of time and frequency respectively) with (a) full representation of the range of time duration and bandwidth and (b) limited to the bounds of 0.5 and 3 in time bandwidth product. 27
Figure 2.4 A summary of the pre-processing of the time-frequency cross correlation algorithm. 27
Figure 2.5 A summary of the post-processing of the time-frequency cross correlation algorithm. 28
Figure 2.6 Simplified diagram of fuzzy logic used to identify the proper optimal reference values with crisp inputs, inference rules, and a reference suitability crisp output (overall validity of a signal for time-frequency domain reflectometry.) 30
Figure 2.7 (Sweeping of the optimal reference in center frequency, bandwidth, and time duration compared using fuzzy logic rule set for standardized determination of the best reference signal for an RG-58 instrumentation cable.) 31
Figure 2.8 The two most optimal reference values determined by a standardized fuzzy logic inference while sweeping the optimal reference from 75MHz to 300MHz: (a) 175MHz and (b) 300 MHz. 31
Figure 2.9 Comparisons of low voltage cables with cross-linked polyethylene (XLPE), ethylene propylene rubber (EPR), and silicone rubber (SIR) insulation types to tree-resistant medium voltage cable (TR-XLPE) . . . 35
Figure 2.10 Abraded 15 meter segment of Rockbestos Firewall III XHHW cable with 1.4cm cutaway of jacket and exposed insulation before and after soaking in water. 36

Figure 2.11 JTFDR metrics for an XLPE insulated Rockbestos Firewall III cable (a) before submerging in water and (b) after submerging in water 37
Figure 2.12 Cross correlation peak curves at progressive aging values exhibited in a sample of medium voltage MV-90 TR-XLPE insulated cable shown during temperature based accelerated aging. 38
Figure 2.13 Summary of peak growth over time exhibited in a sample of medium voltage MV-90 TR-XLPE insulated cable shown during temperature based accelerated aging. 39
Figure 2.14 Peak ratios of incident and reflected peaks for perturbation estimate of line attenuation for 50-300MHz center frequency with 100MHz bandwidth and 60ns time duration. 40
Figure 2.15 JTFDR signal is transmitted along the length of a cable spool to simulate a fault where the end of cable is not measurable, simulating an endless line. 41
Figure 2.16 JTFDR signal is transmitted along the length of a 7 meter segment of cable to measure the closest detectable fault. The time frequency cross correlation value is shown for segments with faults at 1, 2, and 3 meters compared to the unfaulted segment. 43
Figure 2.17 JTFDR signal is transmitted to a cable network, a T-connection of 9, 7, and 20 meter segments with an abrasion fault at 4 meters along the 7 meter segment of cable. A schematic of the wiring network is seen below the TFCC metric scaled to match the adjusted time-delay values scaled by the propagation velocity. 44
Figure 2.18 JTFDR signal is transmitted to a cable network of 9 and 20 meter connected segments with multiple simulated faults. 45

Figure 3.1 Schematic model of a cable with defect or hot-spot. 47

Figure 3.2 Incident and reflected signals in the event of open and short circuit faults using the optimal reference signal show a difference in phase . . . 48
Figure 3.3 Time-frequency cross-correlation metric used for JTFDR falls short when comparing open and short faults due to a lack of phase information in the typical representation. 48
Figure 3.4 Measurement of the growth of the TFCC with a linear increase in a fault simulated at 5 meters. The fault signal for the 5 meter region is simply a scaling of the actual signal obtained from the aging of an XLPE insulated sample by a linearly increasing multiplier. 49
Figure 3.5 Measurement of the growth of the TFCC with a linear increase in a fault simulated at 5 meters. The fault signal for the 5 meter region is simple a scaling of the actual signal obtained from the aging of an XLPE insulated sample by a linearly increasing multiplier. 50
Figure 3.6 Measurement of the growth of the TFCC with a linear increase in a fault simulated at 5 meters. The fault signal for the 5 meter region is simple a scaling of the actual signal obtained from the aging of an LSTSGU insulated sample by a linearly increasing multiplier. 51
Figure 3.7 Measurement of the growth of the TFCC with a linear increase in a fault simulated at 5 meters. The fault signal for the 5 meter region is simple a scaling of the actual signal obtained from the aging of an TXW4 insulated sample by a linearly increasing multiplier. 51
Figure 3.8 Alternative enveloping functions for the chirp signal based on the derivative of the gaussian function. (a) gaussian envelope, (b) first derivative of gaussian, (c) second derivative of gaussian, and (d) third derivative of gaussian 56

Figure 3.9 Alternative reference signals for JTFDR with an enveloped chirp signal based on the derivative of the gaussian function. (a) gaussian envelope, (b) first derivative of gaussian, (c) second derivative of gaussian, and (d) third derivative of gaussian 57
Figure 3.10 Time-frequency distribution of (a) optimal reference and (b) reference with derivative of gaussian function as envelope. 57
Figure 3.11 Time-frequency distribution of (a) optimal reference with second derivative of gaussian function as envelope and (b) reference with third derivative of gaussian function as envelope 58
Figure 3.12 Summary and visualization of the new time-frequency cross-correlation algorithm obtained for the variation of the Gaussian envelope. 58
Figure 3.13 Time-frequency cross correlation peaks generated by measure between individual windowed reference peaks and the reflected signal for 20 meter undamaged RG-58 cable segment (a) with the left-most reference peak (b) with the right-most reference peak with overlayed reflected signal. 60
Figure 3.14 A closer view of the time-frequency cross correlation peaks generated by the measure between individual windowed left-most and right-most reference peak and the reflected signal. 60
Figure 3.15 Experimental setup for JTFDR in a nuclear plant environment including conduit and cable tray segments. 61
Figure 3.16 X-ray CT images of the RG-58 cable comparing baseline sample and a segment aged at an accelerated rate to simulate 9 years of service. 63
Figure 3.17 Cross-sectional 3-dimensional x-ray CT images of the RG-58 cable comparing baseline sample and a segment aged at an accelerated rate to simulate 9 years of service. 64

Figure 3.18 Transversal 3-dimensional x-ray CT images of the RG-58 cable comparing baseline sample and a segment aged at an accelerated rate to simulate 9 years of service. 64
Figure 3.19 JTFDR Metric value for average of 20 acquisitions of baseline or unaged cable. 65
Figure 3.20 JTFDR Metric value for average of 20 acquisitions after 412 hours of accelerated aging simulating 9 years of service. 65
Figure 3.21 JTFDR Metric value for average of 20 acquisitions of an accelerated aging test simulating 30 years of cable life (916 hours of testing). 66

Figure 4.1 Optimal reference signal compared to reflected signal obtained by surface wave reflectometry 69
Figure 4.2 (a) Experimental setup for Surface Wave Optimized and (b)Simulated defect on 10m segment of cable using the surface wave optimized reference shown in time domain (top)and by comparison using JTFDR (bottom). 70
Figure 4.3 Time-frequency cross correlation metric for open end measurement on 2 meter segment of (a) cable in low voltage unshielded case and (b) cable in medium voltage shielded case with stripped injection point. . 72
Figure 4.4 Generation and acquisition system for JTFDR. 72
Figure 4.5 JTFDR system function diagram including surface wave launcher. . . . 73
Figure 4.6 Experimental setup for surface wave optimized JTFDR and TM Surface wave fields in insulated power line. 73
Figure 4.7 JTFDR algorithm updated to measure multiple reflection peaks and total reflected energy 74

Figure 4.8 The JTFDR cross-correlation peaks (blue) are shown here with the autocorrelation (red) and highlighted segment illustrating the peak growth with increased thermal stress over the course of 12 hours of accelerated aging. 76

Figure 5.1 Schematic representation of AH-64 helicopter tail rotor drivetrain test stand (a) and actual test stand (b) with labeled components for comparison. 79

Figure 5.2 Primary accelerometer sensor locations on the tail rotor drivetrain test stand on a per component basis for hanger bearings (FHB and AHB) and intermediate and tail rotor gearboxes (IGB and TGB). 81

Figure 5.3 Unbalance force distribution over the shaft supported at the S_1 and S_2 accelerometers locations (a) cross-section of a bearing and the shaft at the S_1 accelerometer location (b) shaft centerline orbits at the S_1 and S_2 accelerometer locations, and (c) displacement or vibration components in the x and y axis directions (D_u, D_{m1} orbits when $\varphi_y - \varphi_x = 90^\circ$, D_{m1} when $\varphi_y - \varphi_x = 120^\circ$) 82

Figure 5.4 Spectrogram of S_1 for (a) baseline (B/A), and (b) misaligned-unbalanced (MA/UB 3-5). 84

Figure 5.5 Images of the inside of the intermediate gearbox taken by a borescope (a) in a healthy gearbox and (b) after a grease starvation experiment provides significant damage to the gear teeth. 85

Figure 5.6 Time-frequency representation with Zhao-Atlas-Marks kernel showing the time-varying spectrum of a vibration signature near the end of life (4 days before failure) in a Tail Rotor Gearbox case study. 85

Figure 5.7 Time-frequency representation with Zhao-Atlas-Marks kernel showing the time-varying spectrum of a vibration signature near the end of life (2 days before failure) in a Tail Rotor Gearbox case study. Data acquisition surveys are taken at (a) start of run and (b) under torque load from absorption motor 91

Figure 5.8 Time-frequency representation with Zhao-Atlas-Marks kernel showing the time-varying spectrum of a vibration signature near the end of life (1 day before failure) in a Tail Rotor Gearbox case study. Data acquisition surveys are taken at (a) start of run and (b) under torque load from absorption motor 91

Figure 5.9 Time-frequency representation with Zhao-Atlas-Marks kernel showing the time-varying spectrum of a vibration signature near the end of life (day of failure) in a Tail Rotor Gearbox case study. Data acquisition surveys are taken at (a) start of run and (b) under torque load from absorption motor 92

Figure 5.10 Time-frequency distributions of vibration signals from (a) data set 1, and (b) data set 2 with WV distribution, illustrating the potentially negative impact of cross terms in vibration analysis. 93

Figure 5.11 (a) Rényi metric comparison, and (b) sequential sorting of metric for the CW. 94

Figure 5.12 Self Rényi information measure of S_1 and S_2 for baseline in (a)$\sim$(b), and self Rényi information measure of S_1 and S_2 for misalignment in (c)$\sim$(d) 96

Figure 5.13 Mutual Rényi information measure of S_1 and S_2 for (a) Baseline-Aligned, (b) Aligned-Unbalanced, (c) Misaligned-Balanced, and (d) Misaligned-Unbalanced 96

Figure 5.14 Baseline comparisons of the mutual information measure (a) Aligned-Unbalanced, (b) Misaligned-Balanced, (c) Misaligned-Unbalanced 3-5, and (d) Misaligned-Unbalanced 4-5 with the Aligned-Balanced Case 99

Figure A.1 Graphical user interface of the smart wiring program. 111

Figure B.1 Membership function for the estimated cable length from JTFDR for a baseline cable sample. 113

Figure B.2 Membership function for the peak width resolution of TFCC peaks for a baseline cable sample. 114

Figure B.3 Membership function for the summation of the noise or false peaks between reflection at the end of a baseline cable sample. 114

Figure B.4 Membership function for the number of reflections of the end of a baseline cable sample measurable by JTFDR above a user specified threshold. 114

Figure B.5 Membership function for the time-bandwidth product obtained for a given time duration, bandwidth and center frequency of the optimal reference signal. 115

Figure B.6 Membership function for the time-frequency cross correlation magnitude at the end of a baseline cable sample. 115

CHAPTER 1

INTRODUCTION

1.1 PREVENTATIVE MAINTENANCE CONCEPT AND ANALYSIS

Standard maintenance practices in most industries involve replacing existing components after a certain time period or a certain number of operational hours, often preemptive of potential failures. This practice is called time-based maintenance (TBM) and often leads to unexpected failures in critical parts due to unexpected wear and unforeseen physical stresses. Most time-based standards are based on either statistical precedent from historical samples or qualified testing in simulated conditions of typical usage or worst case scenario stresses. On one extreme, usage patterns not previously encountered or addressed in historical life cycles or standardized tests may lead to operational downtime and potential safety hazards [1]. On the other end of the spectrum of cautionary TBM practices, the standards of time-based replacement can be too conservative and focus on disqualifying components for safe use based on a minimum number of hours. We see economic and safety disadvantages in systems that have secondary mechanical and electrical interactions other than electromechanical energy conversion. One such example is the vibration from rotorcraft which can contribute to abrasion of wired components or heat and radiation sources exacerbating aging conditions in nuclear power plants. Likewise, electrical sensors such as accelerometers, load cells, thermocouples, and tachometers on mechanical systems experience failure conditions such as drift or decoupling leading to added noise or signal loss that affect both control and diagnostics in mechanical systems. Therefore, instead of TBM, we consider use-based maintenance practices in both mechanical and electrical components.

This allows for critical part replacement or repair before their full lifetimes on a variable basis balancing and optimizing both economic and safe operating conditions [2]. Concepts of condition-based maintenance will be applied to health monitoring of rotorcraft and rotational electromechanical systems as well as power instrumentation and distribution, or to generalize further, cable systems. We present a set of time-frequency and digital signal processing techniques that can be seen as a toolbox for implementation of system-wide condition-based maintenance.

One example of a condition-based maintenance (CBM) practice is presented by the army's Vibration Management Enhancement Program (VMEP) and Health Usage Monitoring System (HUMS) infrastructure for military aviation fleet management, which fits within the existing framework of vibration management. Vibration analysis techniques developed herein are meant to supplement existing condition monitoring methods and metrics without gathering additional data. However, the techniques could be separated into a separate stand-alone product without dependency on existing infrastructure. This condition-based strategy will be employed for both helicopter hanger bearings and gearboxes based on vibration analysis from accelerometers embedded in a complex mechanical testbed for an Apache AH-64 drivetrain system. We outline general health practices for Apache AH-64 drivetrain systems in Section 5. For health assessment and management of cable systems, we posit new theory and applied examples for Joint Time-Frequency Domain Reflectometry (JTFDR) to help realize a practical implementation of the technology. Elements of cumulative condition based indicator metrics based on multiple assessment methods utilized in the analyses of hanger bearing and gearbox vibration analysis (in Section 5.4) will further the existing state of the art in this field. The overarching goal of both research topics is advancing the time- and reaction-based maintenance schedules typically offered in electrical and mechanical systems toward ones that are predictive and proactive [3, 4].

This introductory chapter will focus on the concepts, significant previous works, current challenges, and overarching goals of maintenance in both electrical and mechanical

systems. We summarize a typical course of action toward this overarching goal of generalized condition-based maintenance to establish the background for unified condition-based maintenance. Further, we generalize this background for other systems with complicated electrical and mechanical systems such as helicopter drivetrain systems, wind farm systems, nuclear instrumentation, control fuel rod systems, and energy generation/distribution systems.

In order to achieve this innovative maintenance practice, we suggest that data be collected from vital operational components and analyzed in order to determine the current (diagnostic) state of the baseline case and later the future (prognostic) health of these same critical components. Moreover, aging or conditioning must be simulated in a controlled testbed and monitored to identify progressive degradation trends using heath assessment metrics. If we compare testbed trends to existing historical component data from active articles, where such data is available, we start the process of forming characteristic prognostic functions. As more failure data is collected from both in-service components and retired or test components, we can increase safety and confidence levels for prognostic functions and analyze root causes from sensor data which are then incorporated into future prognostic indicators for maintainer decision-making. Once we create effective diagnostic and prognostic health assessment monitoring models, condition indicator (CI) or health indicator (HI) single or multiple dimensional metrics operators and maintainers can gather and package useful health indicators from one or more components into a monitoring unit.

Prognostic indicators can be categorized into three separate types: reliability or historical data-driven (Type I), stressor-based (Type II), or degradation-based (Type III) prognostic techniques [5]. Techniques in Type I classification utilize historical failure data to generate failure distributions and an expected value for the behavior of a typical component under average conditions (often TBM practices). These often utilize the Weibull distribution to provide a time to failure estimation where a rate constant shows that failure decreases over time (in the case of high "infant mortality" from components), increases

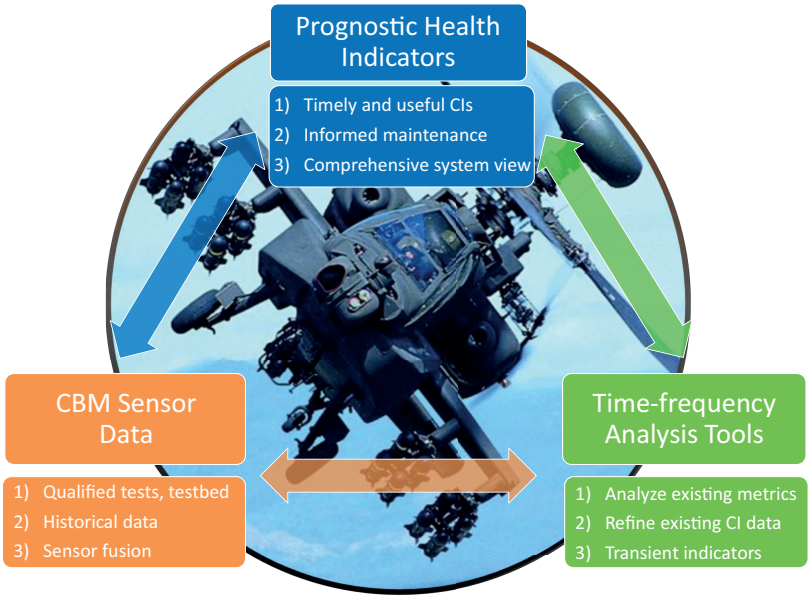

Figure 1.1: Paradigm for Condition Based Maintenance in rotorcraft using vibration sensors, time-frequency analysis, and developing health and prognostic indicators. This is an example of the process for refining an existing prognostic and health monitoring system.

over time (an aging process is present), or a combination of both forming a bath tub shaped curve [6]. Type II classifiers are different in that they attempt to quantify the overall effect of stressing parameters, conditions, and environments on a typical or averaged case component. The last set of techniques, Type III, focuses on predictions based on specific components under specific conditions featuring a corresponding prognostic parameter (CI or HI) and a degradation path [7] to predict end of useful life. Often over the course of a component's life it will transition from Type I to Type II and then from Type II to Type III prognostics over the course of operating time [8]. A transition period often exists between each transition in prognostic indicator where for example Type I and Type II indicators are both actively considered. An example of this overlap is found in the first operational hours where manufacturing defects may lead to infant mortality rates of new components and Type II stressor indicators are taken into consideration near the edge of suspected Type I historical averages of failure. Within the Type III class, the General Path Model (GPM) is a common used prognostic model proposed by Lu and Meeker [7] for reliability engineering to shift to failure-process analysis from the more standard failure-time analysis.

The ideal practice for part health maintenance is summarized in Figure 1.1 with time-frequency analysis used as the main qualifying analysis method for refining of CI/HIs and assessment of CBM sensor data. Other data analysis techniques may be employed to verify prognostic methods and gather useful new CIs from sensor data, however, the emphasis in this research is to provide more relevant information for maintainers from preexisting sensor data. In the case of vibration analysis, interesting and defining characteristics of vibration signatures appear in both the frequency domain and as aperiodic, transient, or sporadic time domain events. The proposed research will focus on developing metrics for health assessment of rotational components in helicopter drivetrain systems from an existing testbed and developing an accelerated aging testbed for instrumentation cable and medium voltage distribution systems. This will be accomplished by focusing on vibration time-frequency analysis of multiple accelerators and with a practical implementation of non-invasive insulation health monitoring in wiring systems.

1.2 Health Monitoring of Rotorcraft Drivetrain

In order to monitor the health status of drivetrain systems, vibration [17, 18], acoustic [19], temperature or infrared, and additional sensor data are useful for a comprehensive part health monitoring status. Over the past decades, great advancements have been made in health diagnostics and vibration management in military helicopters in terms of both progression of metric indicators and cost benefits to the US Army helicopter fleet maintainers [1]-[4]. Changes in maintenance strategy were necessitated by the age of helicopters in army fleets and the sheer volume of operational hours logged in missions. The successes, to date, of pilot programs for prognostic and health monitoring systems and qualified tests of components and systems in university or corporate research facilities and national laboratories have resulted in the large-scale deployment of increasingly useful monitoring systems for helicopters. These include systems such as HUMS (Health and Usage Monitoring Systems) and Vibration Management Enhancement Program (VMEP) in use in the army,

Figure 1.2: A typical legend for Condition Indicator (CI) status as shown in PC Ground Based Station (PC-GBS) fleet monitoring software for military rotorcraft.

national guard, and other military organizations which use hardware such as the Modern Signal Processing Unit (MSPU) for data collection and subsequent mining. Health and usage monitoring systems and their related hardware platforms have generated a wide range of benefits in both domestic and military sectors ranging from increased safety to reduced maintenance costs and better performance [10] along with intangible benefits such as overall sense of safety to pilots [11] and ease of diagnosis for mechanics [12].

Most CBM tools such as HUMS for Apache and Blackhawk helicopters assist machinery maintainers in identifying faulted components through the use of simple visual interfaces and indicators. The most commonly utilized functions are condition indicators (CI), which output a dimensioned or dimensionless single scalar value to monitor key factors most frequently related to frequency analysis of vibration signature. Condition indicators need not be based upon vibration analysis alone and may include component temperatures or acoustic data for separate or fused CIs. Examples of common indicators in machine diagnostics and prognostics include: spectral peak analysis, envelope analysis, energy ratio, crest factor, sideband index, and kurtosis of residual signals [20]. Typically CI values are

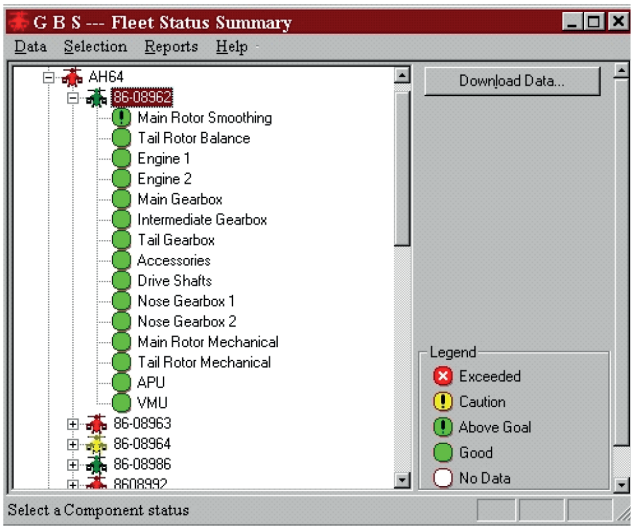

Figure 1.3: An example of a rotorcraft component level CI statistical summary given by PC Ground Based Station (PC-GBS) showing component values.

compared with pre-established thresholds in a simple decision tree classifier which assign the CI some form of ranked class such as "Good," "Caution," or "Exceeded" as shown in Figure 1.2, and maintainers utilize indicators in vital decision-making processes for part change-outs and repair. A given component can have several CIs which may additively form a health indicator (HI). Additionally, CIs or HIs are not fault-specific; multiple fault types can affect the value of a single CI, and a single fault could affect multiple CIs. Another issue to note is that several CIs and HIs can be gathered together to form a prognostic management system. One such system is the PC Ground Based Station (PC-GBS) designed by Intelligent Automation Corporation (IAC) shown in Figure 1.3 which gives feedback on entire fleets of helicopters.

While various condition and health indicators do exist, the proposed work improves their effectiveness by developing new general methods for fault analysis based around time-frequency analysis that could be used in existing or new CIs for indication of machinery failure. Previous studies on CBM from diverse applications [21, 22] have shown that abnormality of the system is characterized by transient precursors in the signals. Through

Figure 1.4: Labeled picture of tail rotor drivetrain testbed at CBM Research Center at the University of South Carolina.

their use in detecting transient precursors, advanced signal processing techniques have contributed to develop diagnostics and prognostics algorithms for aging aircraft [23]. The classical methods for vibration analysis such as spectral analysis or time-frequency distributions represent frequency or time and frequency localized energy. However, it is not expedient to analyze multiple signals that have been simultaneously collected from systems under test. In particular, time-frequency analysis is extremely useful to analyze the transient signature of the abnormality and its precursors [24]. Previous convention dictated that time-frequency based applications were difficult to implement in real-time, however, methods [25] have been proposed to accomplish time-frequency algorithms feasible for the constant monitoring required for CBM [26]. We present a path toward using time-frequency analysis and specified metrics based on time-frequency representations for condition and health monitoring, advancing the analysis of data from existing condition monitoring systems without the use of additional hardware.

We propose a new concept of non-parametric detection and classification of signals. We define time-frequency based self and mutual information in order to classify the health

status of the system components in Sections 1.4 and5.2. Other methods [18], [27], [28] have been proposed to use either classical methods or neoclassical methods moving toward the use of both time- and frequency-based information. Additional methods focus on the non-linear interactions of frequency components such as harmonic frequencies of component fault frequencies and are useful for analysis of periodic faults at steady state [13]-[16]. The proposed method takes advantage of both time and frequency domain transients to establish a complexity measurement for potential assessment of component health. We provide experimental setup and data description in Section 5, results and discussions in Section 5.4, and conclusions of the condition monitoring study in rotorcraft in Section 5.5. Based on the time-frequency based mutual information theory, we present applications of the proposed technique to real-world vibration data and provide a path for future research in Section 5.4.

1.3 Health Monitoring of Electric Cable

The state of the art for non-destructive detection of defects in wiring and cable is divided into two primary categories: time-domain reflectometry (TDR) and frequency-domain reflectometry (FDR). Although these techniques can successfully assess hard defects, they fall short in the detection and location of soft defects, or defects that are typically not visible by inspection, an essential prognostic capability. The limitations of both TDR and FDR are come from a reference signal that uses information from only one domain at a time. While methods of TDR exist that convert time-domain data into frequency information, this conversion is typically only used for filtering noise or other undesirable signals. Likewise, many FDR methods involve picking a set of frequencies of interest in a reflected signal and then converting this information into a time-domain signal for processing of a time delay value. A time delay can then be scaled by a known cable propagation velocity to provide a defect location, however, this time transformation is not used for indication time-based or intermittent faults. Therefore, a key point of this work is that the processing

Figure 1.5: Cables damaged by corrosion and abrasion exposing shielding and insulation.

of the reflected signal in TDR and FDR is less effective in certain instances and would be benefited by a view of both domains simultaneously. Additionally, resolution of fault events can be seen in some cases by viewing the reference signal as a joint time-frequency distribution. We seek an innovative, optimal type of reflectometry that simultaneously uses the time and frequency domains and provide a method called Joint Time-Frequency Domain Reflectometry (JTFDR). The JTFDR technique exhibits its efficacy in cable diagnostics and prognostics such as communication, electric power, and nuclear control and instrumentation (C and I) cables [55].

Searching for a more universal method of signal injection for reflectometry-based assessment, particularly in cases of prognostic remaining useful life indicators, we sought a method that could couple to the cable in question: (1) without requiring removal of the cable under test from a given system, (2) without damaging instrumentation or transmission cables, and (3) sensitive enough to enable assessment of impedance of the cable by reflectometry. Surveying options of implementation in these three key areas, we desired a means to further adjust the optimal reference to account for non-idealities in the frequency response of the injection method. We will focus on the theory of surface wave injection of reflectometry signals, a method for optimizing a reflectometry signal in time and frequency domains, and practical optimizations in narrowband segments or slices of a larger bandwidth. These efforts will cumulatively add to the assessment of health assessment of

insulation materials in real-world electric power systems.

1.4 Joint Time-Frequency Tools for Condition Based Maintenance

The goal of this section is to establish some necessary theoretical background for the time-frequency applications addressed in these CBM practices. Time-frequency analysis will be addressed as it applies in the following two applications: the time-frequency cross correlation forming the base for JTFDR reflectometry (applied in the health monitoring of electric cables) and the time-frequency mutual information measure (used in health monitoring of helicopter drivetrains). The theory explored herein forms a toolbox of theoretical concepts that is common to both forms of maintenance with time-frequency and cross time-frequency distributions forming the basis for both works.

Time-Frequency Distribution

All time-frequency distributions can be obtained from the definition of Cohen's class:

$$TFD_x(t,\omega;\phi) = \frac{1}{4\pi^2}\int\int\int x^*(u-\frac{\tau}{2})x(u+\frac{\tau}{2})\phi(\theta,\tau)e^{-j\theta t-j\tau\omega+j\theta u}d\theta d\tau du \qquad (1.1)$$

Where $x(t)$ is the analytic representation of a signal, $x^*(t)$ is the complex conjugate of $x(t)$, and $\phi(\theta,\tau)$ is a two-dimensional function known as a kernel. The choice of kernel has an effect on marginals, total energy, realness, time shift, frequency modulation, scaling invariance, and cross term minimization [35]. This time frequency distribution can be seen as the Fourier transform of the instantaneous autocorrelation function. The $\tau/2$ terms represent the instantaneous sliding window for the correlation about a central instant u. The kernel selection generalizes the filtering of the time-frequency plane while actual windowing can be provided for the time domain signal such as Hamming or Hanning windows [31],[32]. Among the various types of time-frequency distributions, the spectrogram, the Wigner Ville (WV) distribution, Choi-Williams (CW) distribution, and reduced inter-

ference distribution (RID) have been shown to exhibit the most suitable properties for the analysis of the time-varying frequency characteristics of a disturbance and provide common solutions to the time frequency kernel selection. For this preliminary analysis we will consider the selection of these three kernels along with Zhao-Atlas-Marks (ZAM) kernel to see which kernel performs the best for vibration signal analysis. The kernels for the distributions are given as follows:

$$\phi(\theta,\tau)_{SP} = \int h^*(u-\frac{1}{2}\tau)h(u-\frac{1}{2}\tau)e^{-j\theta u}du \tag{1.2}$$

$$\phi(\theta,\tau)_{WV} = 1 \tag{1.3}$$

$$\phi(\theta,\tau)_{CW} = e^{\frac{-\theta^2\tau^2}{\sigma}} \tag{1.4}$$

$$\phi(\theta,\tau)_{ZAM} = g(\tau)|\tau|\frac{\sin a\theta\tau}{a\theta\tau} \tag{1.5}$$

Where $\phi(\theta,\tau)_{SP}$, $\phi(\theta,\tau)_{WV}$, $\phi(\theta,\tau)_{CW}$, and $\phi(\theta,\tau)_{ZAM}$ are kernels for SP, WV, CW, and ZAM distributions, respectively. These Choi-Williams and Zhao-Atlas-Marks kernels may be classified generally as reduced interference distributions (RID) designed with the intent of reducing the "cross-terms" or inter-harmonic noise introduced by computation of the time-frequency distribution on multi-component signals. To obtain the time-frequency distribution of the optimal reference, we take the Wigner Transform defined for a generic time-domain function, $s(t)$, as follows:

$$W(t,\omega) = \frac{1}{2\pi}\int_{-\infty}^{\infty} s^*(t-\frac{1}{2}\tau)\cdot s(t+\frac{1}{2}\tau)e^{-j\tau\omega}d\tau \tag{1.6}$$

The Wigner-Ville kernel typically forms the simplest example of the time-frequency distribution as a solution of equation 1.1 and will be used in many hand calculations. Further utility will be provided by other reduced interference distributions in software environments such as MATLAB or Octave. We provide the subsequent distribution equations for the spectrogram, Choi-Williams, and Zhao-Atlas-Marks kernels solving for Cohen's class.

$$C(\theta,\tau)_{SP} = |\frac{1}{2\pi}\int e^{-j\omega\tau}s(\tau)h(\tau-t))d\tau|^2 \tag{1.7}$$

$$C(\theta,\tau)_{CW} = \frac{1}{4\pi^{\frac{3}{2}}}\int\int \frac{1}{\tau^2/\sigma} e^{-\sigma(u-t)^2/\tau^2 - j\omega\tau} s^*(u-\frac{1}{2}\tau)s(u+\frac{1}{2}\tau)dud\tau \tag{1.8}$$

$$C(\theta,\tau)_{ZAM} = \frac{1}{4a}\int g(\tau)e^{j\omega\tau}\int_{t-|\tau|a}^{t+|\tau|a} s^*(u-\frac{1}{2}\tau)s(u+\frac{1}{2}\tau)dud\tau \tag{1.9}$$

Time-Bandwidth Product

The time-bandwidth product or uncertainty principle, as it is also called, applies to Fourier transform pairs, $s(t) \rightleftharpoons S(\omega)$, and places limits on the time duration and bandwidth of signals based on the confines of the linear transform associated with these pairs. The uncertainty principle always relates to two variables whose operators don't commute, in this case time and frequency variable which are inversely related [35]. The relationship assures that each of these variables cannot become increasingly narrow at the same time. This narrowness will be summarized in terms of the marginals in time and frequency. Marginals for each variable are the standard deviations or second moments of time and frequency: duration, σ_t, and bandwidth, σ_ω. The variances of these depend on a selection of kernel function that satisfies the conditions of the marginal in both time and frequency domains and the over all time, bandwidth, and product equations are provided in (1.10), (1.12), and (1.14).

$$T^2 = \sigma_t^2 = \int (t - \langle t \rangle)^2 |s(t)|^2 dt \tag{1.10}$$

where the time average is given as:

$$\langle t \rangle = \int t|s(t)|^2 dt \tag{1.11}$$

$$B^2 = \sigma_\omega^2 = \int (\omega - \langle \omega \rangle)^2 |S(\omega)|^2 d\omega \tag{1.12}$$

where the frequency average can be given in terms of frequency or solved in terms of the time variable by substitutions:

$$\langle \omega \rangle = \int \omega |S(\omega)|^2 d\omega = \int s^*(t) \frac{1}{j} \frac{d}{dt} s(t) dt \tag{1.13}$$

The uncertainty principle or time bandwidth product is finally given as:

$$TB \geq \frac{1}{2} \tag{1.14}$$

or more generally,

$$\sigma_t \sigma_\omega \geq \frac{1}{2} \sqrt{1 + 4Cov_{t\omega}^2} \tag{1.15}$$

One example of this time-bandwidth product is given for the instance of a chirp signal within a gaussian envelope. This specific time-bandwidth product will prove important in Sections 2.3 and 2.4. The chirp signal is given as $s(t)$ while the gaussian envelope function is given as $h(t)$.

$$s(t) = (\alpha/\pi)^{\frac{1}{4}} e^{-\alpha t^2/2 + j\beta t^2/2 + j\omega_0 t}; \;\; h(t) = (a/\pi)^{\frac{1}{4}} e^{-at^2/2} \tag{1.16}$$

$$T_t B_t = \frac{1}{2} \sqrt{1 + \frac{\beta^2}{(\alpha + a)^2}} \tag{1.17}$$

The minimum value of this time-bandwidth product is given by a signal [35] such that:

$$-cts(t) = s^{'}(t) \tag{1.18}$$

$$s(t) = (\alpha/\pi)^{\frac{1}{4}} e^{-a(t - \langle t \rangle)^2/2 + j\langle \omega \rangle t} \tag{1.19}$$

Time-Frequency Cross Correlation

JTFDR computes the time-frequency cross correlation between an incident signal and the reflected signal through a propagating medium with the following equation:

$$C_{sr}(t) = \frac{1}{E_s E_r(t)} \int_{t'=t-T_s}^{t'=t+T_s} \int W_r(t', \omega) W_s(t' - t, \omega) d\omega dt' \tag{1.20}$$

where $W_r(t,\omega)$ is the Wigner distribution of the reflected signal; $W_s(t,\omega)$ is the Wigner distribution of incident signal; and E_s and $E_r(t)$ are normalization factors factors related to signal energy simple given as:

$$E_s = \int |s(t)|^2 dt \tag{1.21}$$

Time-Frequency Rényi Information Measure

This section is adapted from a previously submitted paper produced by the author [30]. The classical information measure of a continuous stochastic process is known as Shannon information [33] given as:

$$H_x = -\int_{-\infty}^{\infty} f(x)\log_2 f(x)dx \tag{1.22}$$

where the continuous function $f(x)$ is a probability density function which is positive and bounded between 0 and 1. Williams, Brown, and Hero proposed a measure of time-frequency information by use of the generalized Rényi information [33]. The definition of the generalized Rényi information [34] of a continuous bivariate distribution $P(x,y)$ is defined as follows:

$$H_\alpha(P) = \frac{1}{1-\alpha}\log_2 \frac{\int\int P^\alpha(x,y)dxdy}{\int\int P(x,y)dxdy} \tag{1.23}$$

The definition of the generalized Rényi information can be extended by replacing the bivariate distribution $P(x,y)$ with a Cohen's class [36] time-frequency distribution $C_s(t,\omega)$ of signal $s(t)$ with the following definition:

$$C_s(t,\omega;\phi) = \frac{1}{4\pi^2}\int\int\int s^*(u-\frac{\tau}{2})s(u+\frac{\tau}{2}) * \phi(\theta,\tau)e^{-j\theta t - j\tau\omega + j\theta u}d\theta d\tau du \tag{1.24}$$

Use of the Cohen's class distribution permits a more general solution allowing for variable kernel selection. The kernel function of the distribution is described by the $\phi(\theta,\tau)$

term in (1.24). In other words, the theory described in this section presents analysis for the general case of the Cohen's class time-frequency distribution while any distribution kernel could be selected when applying the time-frequency mutual information measure including, but not limited to, the general (Cohen's class), spectrogram, Zhao-Atlas-Marks, Wigner-Ville, Choi-Williams, or reduced interference distribution (RID) kernel [36]. We selected the spectrogram kernel for the time-frequency information because it has the desirable property of nonnegativity forwarded by Williams, et.al in [33] for all time and frequency variables. We seek to provide consistency of discussion with time-frequency analysis in Section 2 and further utilize the Cohen's class in defining the spectrogram. We define the spectrogram here as a Cohen's class distribution as seen in (1.24) where the kernel function $\phi(\theta,\tau)$ is specified as the spectrogram kernel given by:

$$\phi(\theta,\tau) = \int h^*(u-\frac{1}{2}\tau)h(u+\frac{1}{2}\tau)e^{-j\theta u}du \tag{1.25}$$

The order of the generalized Rényi information determined by parameter α for the time-frequency distribution has been investigated in [45] so that $\alpha = 3$ is a reasonable selection, with the exception of contrived counterexamples [33]. Hence, the following information measure of time-frequency distribution will be utilized:

$$H_\alpha(C_s) = \frac{1}{1-\alpha}\log_2 \frac{\int\int C_s^\alpha(t,\omega)dtd\omega}{\int\int C_s(t,\omega)dtd\omega} \tag{1.26}$$

1.5 Summary of Original Contributions

Based on the previous theoretical framework, we now focus on the original contributions of this work. Our overall goal in health monitoring of electrical cables is to provide the work prerequisite to producing a stand-alone time-frequency based reflectometry device. With all original contributions, we further this main goal by either verifying Joint Time-Frequency Domain Reflectometry, implementing new practices to standardize the results of the time-frequency cross-correlation, or providing less invasive means of testing cables. We enumerate these original contributions to health monitoring of electrical cable below:

1. Automated solution of the optimal time-frequency reflectometry signal to allow a technician-level sweep of time and frequency parameters, without strict knowledge of cable frequency response.

2. Verification of time-domain reflectometry by three separate accelerated aging tests and for varying operational levels of cable voltage (600V I&C, 15kV Underground, and concentric neutral).

3. Derivation of new reference signal using the first derivative of the Gaussian function to envelope a chirp signal. With this new reference, we provide notch filtering of the center frequency and a phase shift discontinuity for easier diagnosis of fault impedance within two separate chirp packets, one of higher frequency and one of lower frequency.

4. Application of sub-wavelength dimension non-intrusive wave launcher for reflectometry monitoring of cable faults. We design a reference signal to fit bandwidth constraints of the surface wave injecting launcher and see varying severity of faults over the course of thermal aging without direct electrical contact to the cable under test.

Our main goal for health monitoring of the tail rotor drivetrain is to provide effective condition or health indicators by use of time-frequency analysis. We present the original works related to these goals as follows:

1. Provide time-to-failure time-frequency analysis of drivetrain gearbox with summarizing condition indicator in the form of Rényi information measure. We further develop this summary metric for the time-frequency representations of vibration data into the Mutual Information Measure (MIM) as cross-time-frequency representations are analyzed by Rényi information.

2. Derivation and demonstration of time-frequency Mutual Information Measure (MIM).

3. Qualification and quantification of drivetrain health by means of time-frequency Mutual Information Measure in terms of balance and alignment of rotorcraft drivetrain shafts.

1.6 Summary of Document Organization

An introduction has been presented to basic concepts of time-frequency analysis vital to condition monitoring in both electrical wiring and rotorcraft components such as bearings and gearboxes. Maintenance practices for both systems utilize time-frequency analysis as well as auto- and cross-correlations and filtering techniques. We provide a brief outline of concepts for each remaining chapter to summarize the concepts presented and direct readers to relevant theoretical or topical sections.

In chapter 2, we present the basic concepts of joint time-frequency domain reflectometry including a reference signal partially localized in both the time- and frequency- domains. We derive the time-frequency cross-correlation and provide practical and experimental results for comparison of low and medium voltage cables. We present an optimal time-frequency reference signal for both control and instrumentation and transmission level wiring. Practical considerations such as minimum and maximum distance of fault estimation, detection of faults in networks of connected cables, and non-aging related faults will also be discussed in Chapter 2. Continuing a focus on the optimal reference signal, in Chapter 3 we describe additional verification of the time-frequency cross correlation by extended aging while also presenting further updates to the time-frequency domain reflectometry theory that include the generalization of the time-frequency envelope of the optimal reference. In chapter 4, we utilize a surface wave launcher to provide non-contact implementation of a subset JTFDR. Using this non-intrusive signal launcher, we provide a method of assessing aging in cables without the need to remove the sample under test in some cases. This set non-invasive test methods allows to provide new implementation of non-invasive monitoring of the health of vital segments of cable.

In chapter 5, we provide further theoretical explanation of the Rényi information of time-frequency representations as applied to helicopter vibration analysis or vibration signature analysis in general. We use vibration analysis to focus on individual component fault diagnostics and case studies for drivetrain hanger bearings and gearboxes. Classification of faults of varying degrees of misalignment and unbalance in the drivetrain is possible using mutual information measures developed from the time-frequency representations of the vibration signals gathered from a tail rotor drivetrain teststand. Additional conclusions, future work, and references are then provided.

CHAPTER 2

HEALTH MONITORING OF ELECTRICAL CABLE

2.1 INTRODUCTION AND STATE OF THE ART

In order to prevent electrical outages and to save maintenance expenses, a prognostic technique is needed which can quantify the degradation of the insulation in cable systems and predict the remaining life of the cable. Ideally, the technique should be non-destructive, non-intrusive, and applicable to cable types and insulation materials commonly used. Furthermore, the ideal scenario is to be able to accurately monitor the health status of cable in real-time. Existing methods for obtaining health diagnostics of cable infrastructure may be categorized as mechanical, chemical, or electrical in nature, with further subdivisions within these categories for description of destructive, potentially destructive, and non-destructive tests.

Several testing standards exist within these different categories. Standard IEC 62582 relates mechanical and chemical tests for instrumentation and control important to safety in Nuclear Power Plants (NPP) with subsections for elongation at break [38], indenter modulus and and insulation recovery time testing [39, 57], and oxidation induction techniques [40]. Of these the classical assessment methods, none meet the ultimate goals of embedded sensor based real time condition health assessment. Elongation at break methods destructively test a representative sample to measure the amount of bending a sample can undertake before breaking and measure stress-strain relationships. Indenter modulus tests are typically not destructive but involve testing a localized spot by pressing into the cable insulation material and assessing the recovery time or depth of the indented segment.

These indenters give a general idea of the health of the cable without providing a clear determination of any specific faults. Oxidation induction time involves heating a sample well beyond the allowable range of oxidation and measuring the oxidation time or temperature of the cable decomposition and is naturally destructive in nature. Additional mechanical and chemical test methods include thermogravimetric analysis (TGA) and density measurement, infrared spectroscopy (FTIR and NIR) [41], and ultra sonic velocity. General electrical methods of cable health assessment in low to medium voltage systems include insulation resistance measurement, tan delta testing, broadband impedance spectroscopy, and time, frequency, or time-frequency reflectometry. Very low frequency (VLF), AC or DC voltage withstand, and partial discharge tests [42] are also common in medium to high voltage systems. Instructions for these tests are provided under IEEE 400 series standards. It is important to remember that all withstand tests work on the principle of applying a voltage at some value either a high percentage of or percentage over the rated voltage, potentially damaging even to a healthy cable. In order to present a novel approach to cable monitoring, the method should focus on non-destructive and non-invasive test methodology informed by a basis in, or comparison to, existing or established test methods.

One potential method of addressing these concerns of non-invasive and in-situ testing methodology would be focusing on reflectometry techniques. The field of reflectometry-based cable health or fault assessment is wide, with examples in categories such as time-domain (TDR), frequency-domain (FDR), and hybrid methodologies such as time-frequency domain reflectometry (TFDR), each presented with distinct subclassifications. The NRC and Brookhaven National Laboratory have been working on the diagnostics and prognostics of electric cables with the Broadband Impedance Spectroscopy (BIS) technique developed by Boeing [54]. On an international scale, the OECD Halden Reactor Project in Norway is researching similar issues in monitoring the condition of electric cables; their method is known as Line Resonance Analysis (LIRA) [55]. The purpose of these techniques is to detect and locate defects before they cause a component to fail. These

two methods both monitor impedance of faults caused by insulation degradation using frequency-domain reflectometry (FDR). Methods within the time domain reflectometry subset exist such as the In-Situ Wire Damage Detection System (ISWDDS) developed by NASA/ASRC Aerospace. The ISWDDS integrates a specialized wire within the conductor core and a conductive layer covering the inner insulation film to monitor defects in wiring and insulation using TDR [57]. This method depends on installation of conductive monitoring devices at the manufacturing level and does not have much application for existing aging cable infrastructure.

Additional notable subcategories of reflectometry include sequence and spread spectrum time-domain refelctometry (STDR and SSTDR) and joint time-frequency domain reflectometry [53, 56] which both utilize cross-correlations of incident and reflected signals. Previous comparisons completed in other works [62] outline more tangible qualities of reflectometry metrics such as cost, accuracy, size, and convenience as well as intangible such as the reduction of noise which contributes to the accuracy of the overall system. This work and others suggested that minor changes such as insulation damage may be difficult to interpret [61]. Time-frequency domain reflectometry techniques are forwarded as a means of assessing cable insulation damage as evidenced by accelerated aging. In our tests, accelerated aging is primarily performed by thermal means, utilizing activation energy of insulation materials as a determining factor for heating profiles which simulate degradation. Other methods of accelerated aging or qualifying tests include high voltage withstand, nuclear exposure, vibration induced abrasion, or moisture and environmental tests.

In practice however, there are no condition monitoring techniques available that have all the above attributes. The capability of joint time-frequency domain reflectometry (JTFDR) to monitor the status of cable insulation is evaluated in an effort to predict the remaining life of power cables. JTFDR captures the advantages of both TDR and FDR while avoiding some of their limitations by using a reference signal simultaneously optimized in both

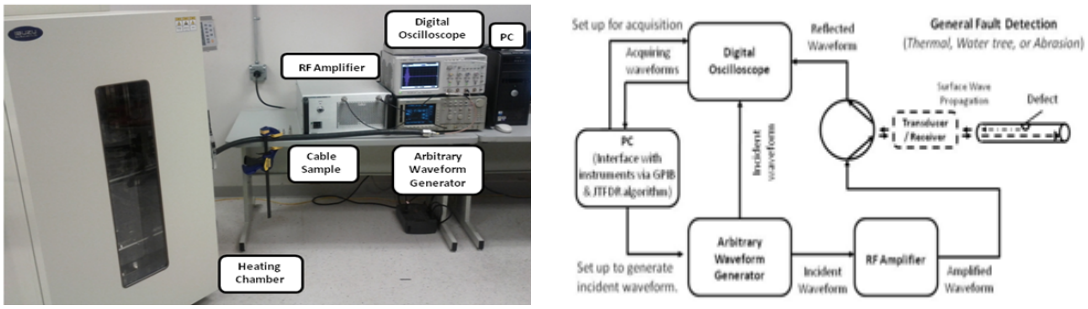

(a) (b)

Figure 2.1: Experimental setup is shown with a (a) labeled figure of the laboratory setup and (b) a system function diagram

time and frequency domains [53]. A distinct advantage of this reference signal is its configurability; the user can select appropriate parameters of the reference signal, including frequency bandwidth, center frequency, and time duration, by considering the frequency characteristics of the wire being tested. JTFDR has been proven to be able to accurately and sensitively detect both hard and incipient defects on coaxial cables [54]. The unique features of the time-frequency cross-correlation function employed by JTFDR also allow it to monitor the minor changes in cable insulation which indicate the health status of the cable with a high degree of sensitivity.

2.2 Experimental Setup

Shown in Figure 2.1(b) is the system function diagram that describes the configuration and function of the experimental devices of the JTFDR wiring test bed. The computer (PC) instructs the arbitrary waveform generator to produce the Gaussian-chirp incident signal based upon the input center frequency, bandwidth, and time duration with optional variations in reference signal such as sinusoidal modulation. This incident signal propagates into the target cable via the RF amplifier in cases of longer cable lengths, is reflected at the fault location, and travels back to the signal launcher/receiver. The signal launcher/receiver should be seen as a general implementation with a circulator or switch being used for this task in laboratory settings while future work would implement a wireless sensor for insu-

lation assessment. The reflected signal is redirected to the digital oscilloscope. The smart wiring program (shown in more detail in Appendix A.1) acquires both the incident and reflected signals from the oscilloscope, calculates the time-frequency distribution of the incident and reflected signals, and executes the time-frequency cross-correlation algorithm. This algorithm is used to detect, locate, and assess or quantify any defects on the cable. The heat chamber used for accelerated thermal aging is also shown in Figure 2.1(a). For longer or more dispersive cable media, we make use of an RF amplifier (up to 120W ouput power) to provide increased range of detection while keeping a l meter or better resolution for the JTFDR method. This helps stabilize against instrumentation noise for the AWG and oscilloscope while also providing sufficient resolution for detection of multiple reflections of the incident reference signal.

2.3 Joint Time-Frequency Domain Reflectometry Optimal Reference

To produce an optimal reference signal we must optimize a balance between time domain resolution and frequency domain resolution. In order to optimize the resolution in both domains, we consider a signal that satisfies the uncertainty principle (derived from the product of time and bandwidth variances and meeting the Cauchy-Schwarz inequality as described in (1.14)). In this, case we have chosen a Gaussian envelope due to its functionality as an eigenfunction of the Fourier transform and its similar variance in both the time and frequency domain. This Gaussian envelope encloses a chirp signal which provides a specified frequency bandwidth and the overall equation is provided below:

$$s(t) = \left(\frac{\alpha}{\pi}\right)^{1/4} e^{-\frac{\alpha(t-t_0)^2}{2} + j\frac{\beta(t-t_0)^2}{2} + j\omega_0(t-t_0)} \tag{2.1}$$

The equation provided here follows that of previous work in time-frequency domain reflectometry [46], [53]-[56], however this signal can be further generalized to allow for selection of different time-frequency enveloping functions for different situation. The generalized equation follows:

$$s(t) = \left(\frac{\alpha}{\pi}\right)^{1/4} \psi(t,\omega) e^{j\frac{\beta(t-t_0)^2}{2} + j\omega_0(t-t_0)} \tag{2.2}$$

where $\psi(t,\omega)$ provides the enveloping function:

$$\psi(t,\omega) = e^{-\frac{\alpha(t-t_0)^2}{2}} \tag{2.3}$$

Additionally, the use of the Gaussian envelope provides the added benefit of having well-established background in general statistics and statistical signal processing of jointly random bivariate distributions. In proposed research, Gaussian properties typically used for statistical hypothesis tests will be used for identification of envelope center and outer boundaries (used in detection of fault location and automated determination of optimized reference). In this study, we will work with the function under the simplifying assumption that time center t_0 is neglected (or centered at zero). This yields the following equation:

$$s(t) = \left(\frac{\alpha}{\pi}\right)^{1/4} e^{-\frac{\alpha t}{2} + j\frac{\beta t^2}{2} + j\omega_0 t} \tag{2.4}$$

As such, the first step in applying JTFDR is optimizing the reference signal used in reflectometry for the given cable. This is done by first performing a frequency sweep with a network analyzer or similar measurement configuration and then running a loop through time duration, bandwidth, and center frequency properties of the optimal reference to obtain the raw data and cross correlation peak data for a range of references. From there, an operator must parse through a table of values collected from the looping operation and visual inspection of waveforms to determine a proper selection. A simplified diagram of the process of determining the time-frequency cross-correlation (described in more detail in Section 1.4) between the optimal reference or incident signal and the reflected signal is shown in Figure 2.4 and 2.5.

One of the proposed tasks for improvement of this process is to base optimal reference selection around key parameters identified by visual inspection to provide a good indication of spatial resolution in fault location and sensitivity to changes in the metric. Parameters

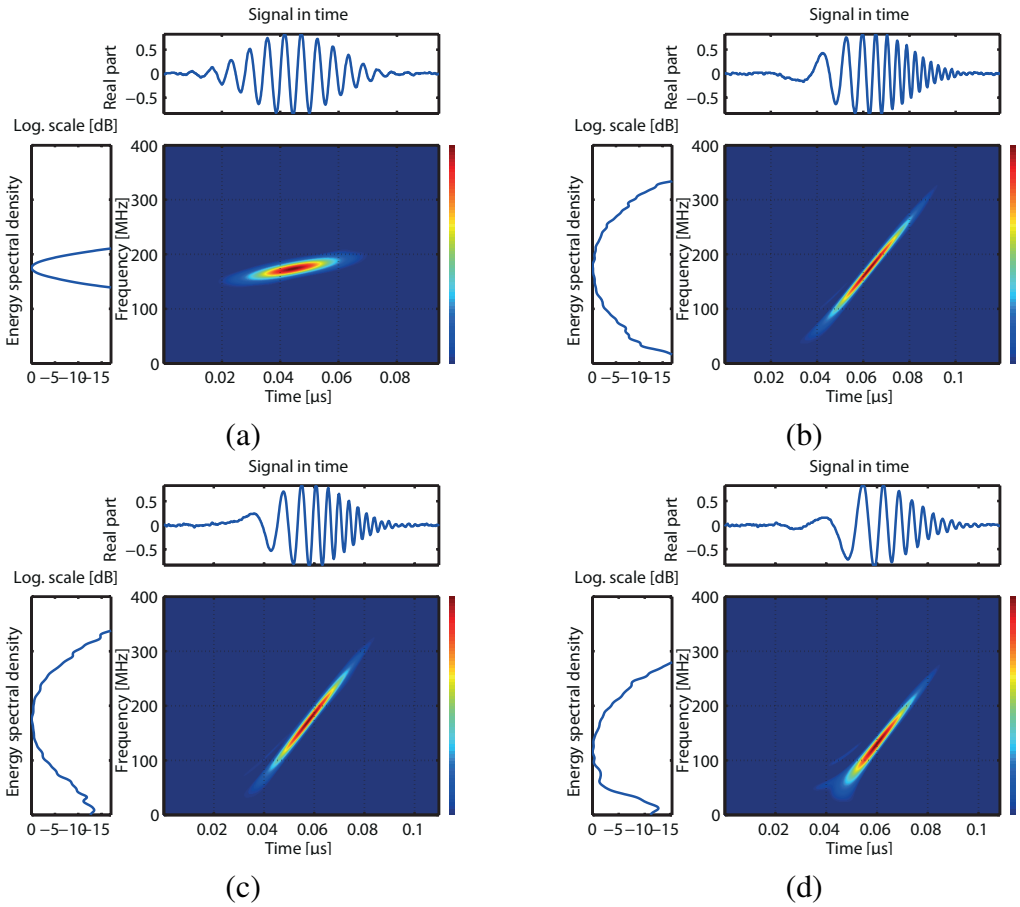

Figure 2.2: Time-frequency distribution of various optimal reference options with differing center frequency (CF), bandwidth (BW), sweeping frequency, and time duration (TD): (a) $CF = 175MHz$, $BW = 50MHz$, and $TD = 80ns$, (b) $CF = 175MHz$, $BW = 100MHz$, and $TD = 80ns$, (c) $CF = 175MHz$, $BW = 100MHz$, and $TD = 60ns$, and (d) $CF = 125MHz$, $BW = 100MHz$, and $TD = 60ns$

to optimize the reference include the width of peak pulses, where shorter width typically indicates better spatial resolution. Additionally, minimal noise between peaks and a higher number of reflections along with a higher sweeping frequency typically indicate better accuracy in measurement. From these factors, an algorithm can then be derived along with optimizing equations relating the bandwidth and sweeping frequency of the reference signal.

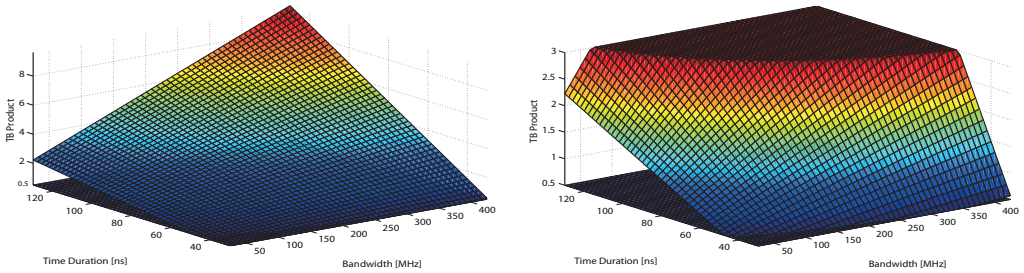

(a) (b)

Figure 2.3: The time-bandwidth product for a sweeping of the optimal reference signal in time duration and bandwidth (second moments of time and frequency respectively) with (a) full representation of the range of time duration and bandwidth and (b) limited to the bounds of 0.5 and 3 in time bandwidth product.

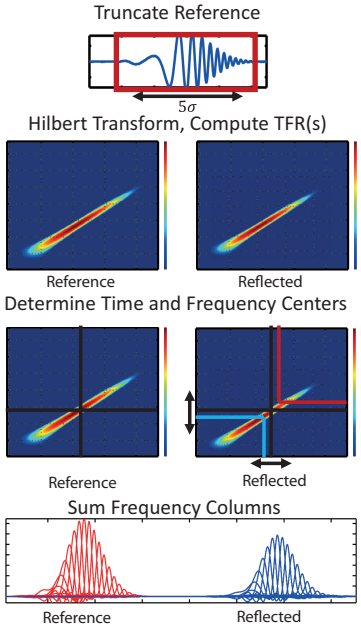

Figure 2.4: A summary of the pre-processing of the time-frequency cross correlation algorithm.

2.4 Automated Selection of Optimal Reference by Fuzzy Logic Decision

One strength of JTFDR is the adaptability of the optimal reference signal in terms of center frequency, bandwidth, chirp sweeping frequency, modulation of chirp, and time duration of envelope to specifically suit a cable type without even necessarily having a priori knowledge of the cable frequency response. However, this adaptability can also lead to poor results if the optimal reference is poorly selected or differing results if the reference signal

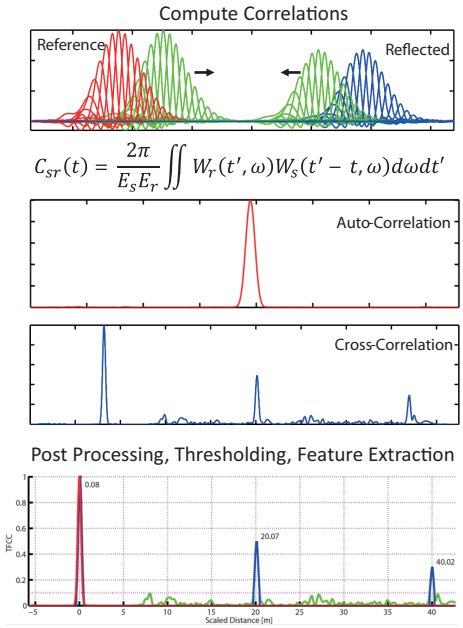

Figure 2.5: A summary of the post-processing of the time-frequency cross correlation algorithm.

is chosen in a nonstandardized way. Mostly, the selection of optimal reference has been left to a human user with subjective determination parameters. A simplified fuzzy logic inference set is proposed to quantify previously subjective optimal parameters and standardize a means of selecting reference signals for the determination of possible prognostic indicators.

The first step of using a fuzzy logic inference set is initialization of crisp (or unclassified) variables. Here we define the crisp variables most important to our overall outcome and then assess linguistic terms such as “Good,” “Caution,” and “Exceeded” for example. Then we construct membership functions such as triangular, trapezoidal, gaussian, singleton, or piecewise linear (custom) probability functions which define where on our continuum of linguistic terms the crisp variable falls [43]. The three previously mentioned linguistic terms may have actual ranges where “Good” corresponds to a gaussian distribution between 0.60 and 1, “Caution” from 0.30 to 0.66, and “Exceeded” below 0.33. These ranges may overlap or be a single discrete value or range of values. The final step of initialization is the construction of logic based rules for the inference of a final output or set

of outputs.

Once membership of different fuzzy categorizations is derived we have a fuzzy or "fuzzified" input set [44]. The exact determination of the "fuzzification" and related membership functions for our specific variables are provided in Appendix B. These are fuzzy variables to which our previously initialized set of rules can be applied. For the purpose of optimal reference classification by fuzzy inference, we chose gaussian membership functions due to the relatively small ranges in our classifications and the amount of overlap between optimal, fair, and marginal statuses. For the most part, a correct or known optimal value exists for each each crisp input and values within a small tolerance on either side provide fair boundaries. We then apply the rules to our fuzzified input set, evaluating using fuzzy set operations and combine the values given by rules. Fuzzy set operations are essentially union (OR), intersections (AND), and probability negation or complement (NOT) combinations using the accumulation of the membership function, μ. For example the most common cases for union and intersect (the ones used in this study) are maximum and minimum values. Equations for these set operators are given below for separate membership functions of example fuzzy sets, A and B:

$$OR : Max\{\mu_A(x), \mu_B(x)\} \tag{2.5}$$

$$AND : Min\{\mu_A(x), \mu_B(x)\} \tag{2.6}$$

Rule combinations can be weighted sums that stress importance of certain parameters to the overall output. Using the rules to make our inference, we then "defuzzify" the outputs to obtain a crisp output set. Defuzzification is determined by a center of gravity function given in 2.7.

$$U = \frac{\int_{min}^{max} u \cdot \mu(u) du}{\int_{min}^{max} \mu(u) du} \tag{2.7}$$

This overall inference process is shown in Figure 2.6. The crisp inputs are the estimated cable length given by TFCC, the width of half of a TFCC peak, the noise between peaks (or

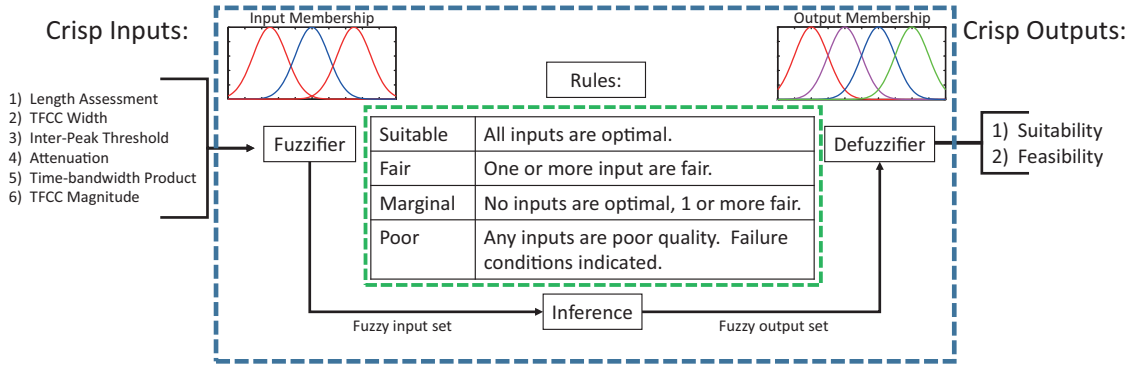

Figure 2.6: Simplified diagram of fuzzy logic used to identify the proper optimal reference values with crisp inputs, inference rules, and a reference suitability crisp output (overall validity of a signal for time-frequency domain reflectometry.)

false peaks) on a baseline cable sample, attenuation of the cable as determined the number of reflections of the end of the cable visible in the TFCC plot, time-bandwidth product, instantaneous bandwidth, and the overall maximum magnitude of reflected TFCC peaks. The rules are summarized in Figure 2.6, however, more detailed rules are provided in Table 2.1. These rules will be applied for an RG-58 cable sample in Section 2.5.

Table 2.1: Summary of Inference Rules for Automated Optimal Reference Determination

Length Estimate (m)	*Resolution Peak (m)*	*SNR*	*Attenuation (Peaks)*	*TB Product*	*TFCC*	*Optimal*
AND						
Good	Good	Sub Threshold	Good	Super Optimal	Good	Suitable
Good	Okay	Threshold	Good	Sub Optimal	Okay	Fair
Way Over/ Way Under	Marginal	Exceeded	Bad	Bad	Bad	Bad
OR						
Over/ Under	Marginal	Exceeded	- -	Sub Optimal	- -	Marginal
Way Over/ Way Under	- -	- -	- -	Bad	Bad	Bad

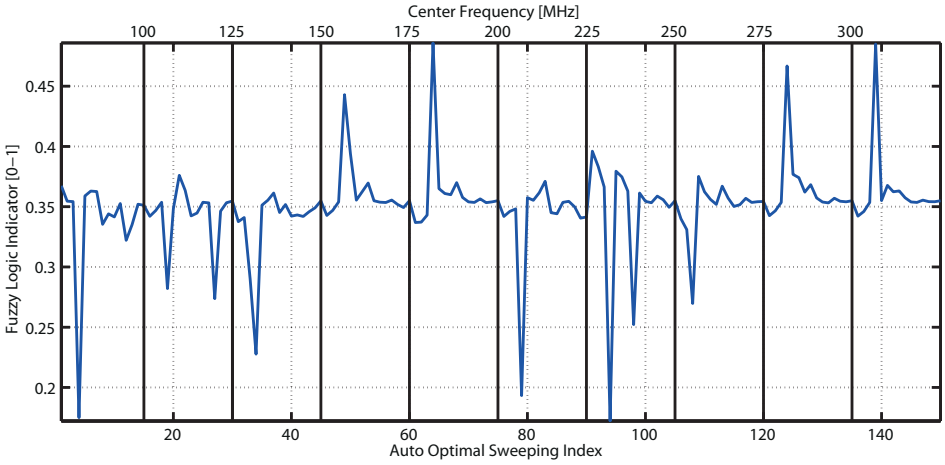

Figure 2.7: (Sweeping of the optimal reference in center frequency, bandwidth, and time duration compared using fuzzy logic rule set for standardized determination of the best reference signal for an RG-58 instrumentation cable.)

2.5 Results Using Standardized Reference

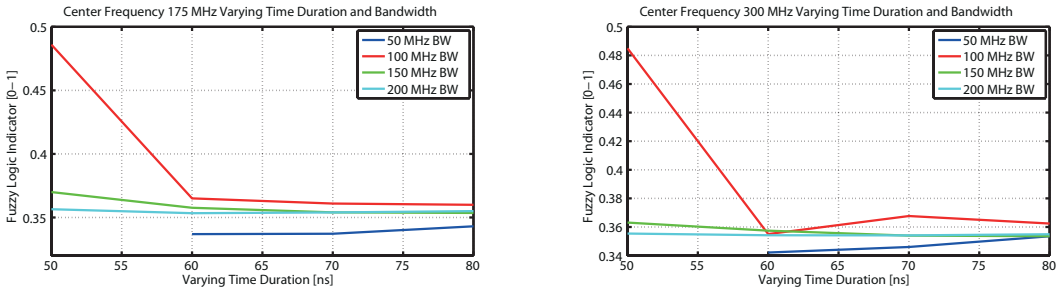

(a) (b)

Figure 2.8: The two most optimal reference values determined by a standardized fuzzy logic inference while sweeping the optimal reference from 75MHz to 300MHz: (a) 175MHz and (b) 300 MHz.

The automated selection criteria for optimal reference provide a means of finding the best reference signal for transmission in a given cable type and length. Fuzzy logic inference rules also allow for a consistent selection of a signal that meets the desired properties of the end user. An example will be shown of the sweeping process for finding the optimal reference value and resulting time-frequency cross correlation peaks associated with the best results.

A sweep was performed with a varying time duration, center frequency, and bandwidth using the experimental setup described in Section 2.2 and Figure 2.1. Sweeping for center frequency in the case of the RG-58 cable sample tested ranged from 75MHz to 300MHz with intervals of 25MHz. This frequency region was selected by performing an initial sweep of the cable with a simple sinusoidal signal to find its typical frequency response and a region with minimal attenuation in the frequency domain. The datasheet for a given cable will typically provide relevant data for the average cable, however, this data is not strictly necessary. The time duration was swept from 50 to 80ns with the lower bound being chosen for it's reproducibility in simpler signal generation systems such as Field Programable Gate Array (FPGA), Application Specific Integrated Circuits (ASIC), or other minimally sized topologies. The upper limit of time duration is chosen particularly based on limiting the time-bandwidth product to its minimal allowable amount of 0.5 and allowing a good resolution of fault detection in the TFCC. Lastly, bandwidth was varied from 50 to 200MHz in increments of 50MHz with values also chosen to limit the time-bandwidth product. At each step interval of time duration, center frequency, and bandwidth, the time-bandwidth product is first evaluated to determine whether the potential reference signal is valid. Any signal with a time-bandwidth product less than 0.5 is immediately disqualified for consideration and calculations skipped.

With a sweeping of the optimal reference parameters provided by the arbitrary waveform generator and collected in the testing PC, a collection of the crisp inputs is summarized in an output file with the signal parameters of interest. These include the estimated length to end of cable, inter-peak noise threshold, attenuation, time-bandwidth product, and magnitude of TFCC metric. The inference set from Figure 2.6 is then applied to the output summary file and the sequential results of the sweeping can be seen in Figure 2.7. The major parameter for ordering the resultant data utilized here is the center frequency with variations in time duration and bandwidth being hard to distinguish. Figure 2.8 highlights the two highest values for the optimal fuzzy logic index in terms of center frequency at

175MHz and 300MHz respectively and shows the results they yielded for variation in time duration and bandwidth. The optimal reference at 175MHz was chosen as the standardized reference due to its high optimal suitability index.

2.6 Diagnostics and Prognostics

The Modified Arrhenius Equation

Typically aging of a cable is defined as any process electrical, mechanical, thermal, or environmental which might reduce the overall effectiveness of the cable for power or signal transmission. An alternative, and broader, definition of aging would describe the process as any condition over the duration of cable life that leads to increased susceptibility to hardware faults or that might otherwise lead to premature failure. In our case, actual aging is represented broadly by a simulation of thermal stress and in particular by uniform heating of a section of cable at a constant temperature above the normal thermal capacity. Multistress aging of electrical insulation in radiation environment by IEEE 775 standard or qualification of electrical equipment by IEC60780 standard would be ideal, however, additional equipment is required for tests of this nature. Testing by IEEE 775 requires radiation handling equipment or transport of irradiated cable materials. Standard IEC 60780 requires an environmental heating chamber too extensive for our setting. Therefore, our tests will be based off of IEEE 1064. As defined by IEEE 1064 standard, aging is the occurrence of irreversible deleterious changes that critically affect performance and shorten useful life [48].

The well known Arrhenius model is used to determine the aging test parameters such as thermal stress and time duration. The Arrhenius model is based on chemical rate theory and has been verified to be effective for many solid materials. The equation of the Arrhenius model describes the relationship between the reaction rate and the temperature of a chemical reaction [65]. One key point to remember is that this reaction rate and tem-

perature correlation only applies to a single reaction, while insulation degradation is not a single chemical process, but rather more complicated with multiple reactions and often nonlinear deleterious effects. This model has however become accepted as an indicator and metric for cable aging as outlined in the IEEE standard. The modified Arrhenius equation for an accelerated aging test follows:

$$\frac{t_s}{t_a} = e^{[E_a/B(1/T_s - 1/T_a)]} \tag{2.8}$$

where the following hold true:

T_s is the service temperature;

T_a is the accelerated aging temperature;

t_s is the aging time at service temperature;

t_a is the aging time at acceleration temperature;

E_a is the activation energy of the material;

B is the Boltzmann's constant (given below),

$$B = 8.617 \times 10^{-5}[eV/K] \tag{2.9}$$

This equation equates the heating of a material at temperature T_a for time t_a to the aging of the material at the service temperature T_s over a time t_s.

Accelerated Aging Test with Various Low Voltage Insulation Types

Using the previously described modified Arrhenius equation as a guide for accelerated aging, and utilizing standard activation energy values for various cable types, tests were performed on low voltage control and instrumentation cable to simulate 120 years of service life at 50 degrees Celsius, nearly double the expected service life of a typical cable. During the accelerated aging tests, JTFDR is employed to assess the various states of the cables during the aging process and growth in measured time-frequency cross correlation

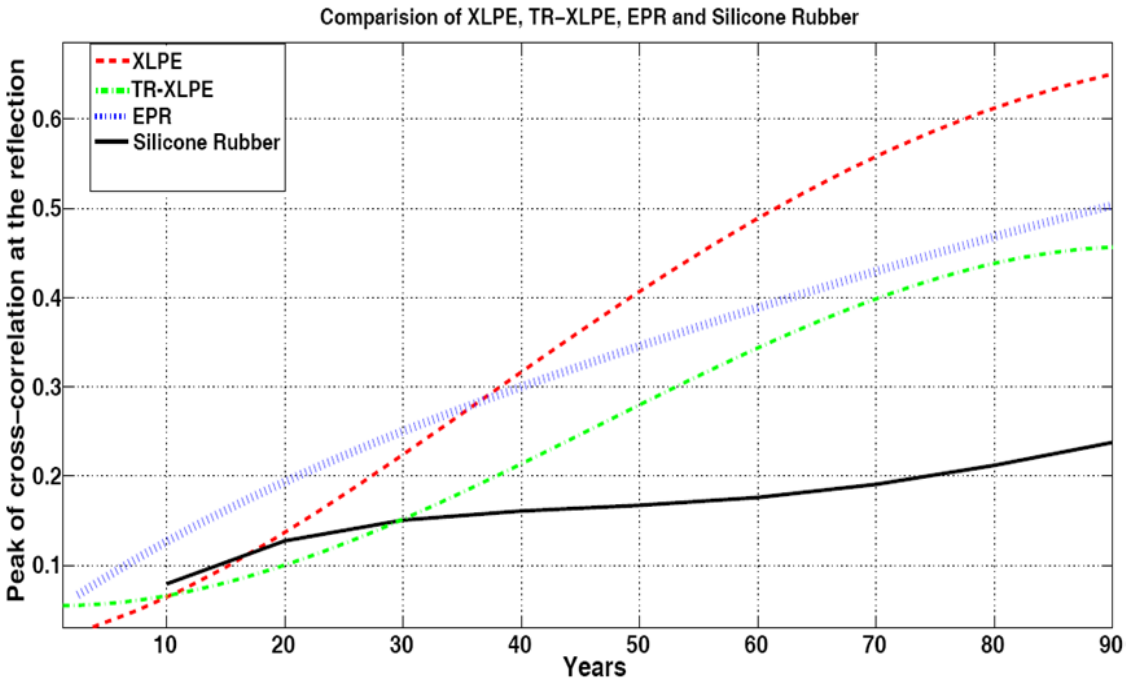

Figure 2.9: Comparisons of low voltage cables with cross-linked polyethylene (XLPE), ethylene propylene rubber (EPR), and silicone rubber (SIR) insulation types to tree-resistant medium voltage cable (TR-XLPE)

peak value growth. Before any external thermal stresses are applied, the waveforms are acquired multiple times to account for noise and acquisition error and processed for each cable sample to obtain the time-frequency cross-correlation baselines for future comparison. Only a localized segment (typically 1 m) is aged to simulate non-uniform aging along the length of a cable sample (10-20m for verifying tests). A certain number of hours (t_a), is computed depending on how long, (t_s), the cable is to be aged. When the cables are to be measured using the time-frequency cross correlation metric at regular intervals, the "hot spot," or aged segment, is cooled to ambient temperature to ensure that all metric increases are related to actual simulated aging and not simple geometry changes within the cable samples. The waveforms are acquired and processed after this cooling process is verified with an infrared thermometer, based on surface temperature of the jacket, to obtain an updated time-frequency cross-correlation plot. The program then calculates the peak value corresponding to the aged segment and records this new value for comparison with other

collected health assessments.

Analysis of Abrasion and Water Intrusion Faults

In order to verify the method of JTFDR, we look at a faulted low voltage cable with abrasion. The cable under test for this fault is a Rockbestos Firewall III XHHW cable with XLPE insulation. This cable has a 1.4cm section of outer jacket cut away and removed exposing the insulation material. The cut segment was measured using a caliper set and care was taken to ensure that the insulation was not completely stripped. Measurements were taken using the experimental set-up presented previously described and the abraded segment could be located by TFCC peaks given a threshold of 0.1 on the normalized scale. Next, we submerged the cable in a pan of water for 1 minute before measuring with 20 data acquisitions. This number was chosen to provide a better average of the somewhat unpredictable faults presented by the water intrusion. The fault is then measured and averaged again immediately after removing from water. The test procedure is shown in Figure 2.6.

Figure 2.10: Abraded 15 meter segment of Rockbestos Firewall III XHHW cable with 1.4cm cutaway of jacket and exposed insulation before and after soaking in water.

Figure 2.11 shows the results of JTFDR before and after submerging the exposed segment into water. The TFCC is significantly increased while submerged and immediately after being removed. The location of the submerged segement can be located accurately

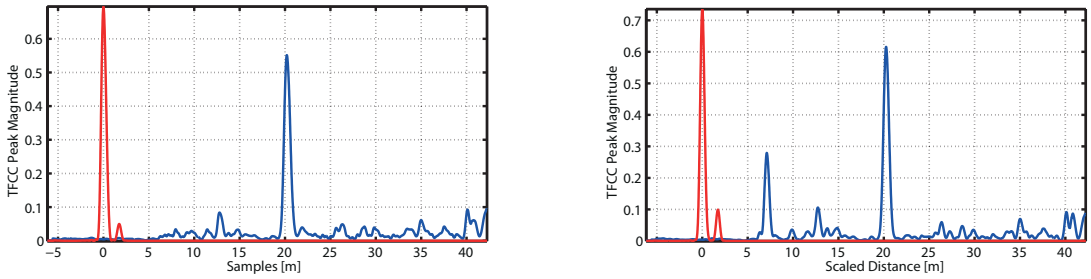

(a) (b)

Figure 2.11: JTFDR metrics for an XLPE insulated Rockbestos Firewall III cable (a) before submerging in water and (b) after submerging in water

and reliably. This helps showcase that the method of JTFDR is valid for multiple failure modes.

Accelerated Aging Test with Medium to High Voltage Cable

With previously collected and summarized aging tests for low voltage cables of given insulation types in Figure 2.9, a new test was undertaken to assess the viability of the method in medium voltage cable media. This tree resistant XLPE sample is also plotted in Figure 2.9 and a description of this cable follows. In the case of the medium voltage tree resistant XLPE cable, an activation energy E_a of 1.33 eV [15] was used with an acceleration temperature of 140°C. The typical maximum operating temperature of MV-90 cable is 90°C. With a an acceleration temperature of 140°C and a simulated service temperature (T_s) of 90°C over 90 years (t_s), the simulated aging time can be found to be 24 hours.

Aging was simulated using a heating chamber with two through ports for cable access separated by 0.6 meters. A meter long "hot spot" was desired for localized aging, however, in the case of thicker MV-90 underground cable, minimum bend radius along with cable stiffness and thickness allowed only 0.6 meters, or the separation between cable through ports, for hot spot consideration. Both XLPE insulated cable samples (Rockbestos Firewall III XHHW, low voltage and MV-90, medium voltage) were heated for one hour at a time at 140°C. The cables were then cooled to ambient temperature (25-27°C) as measured by

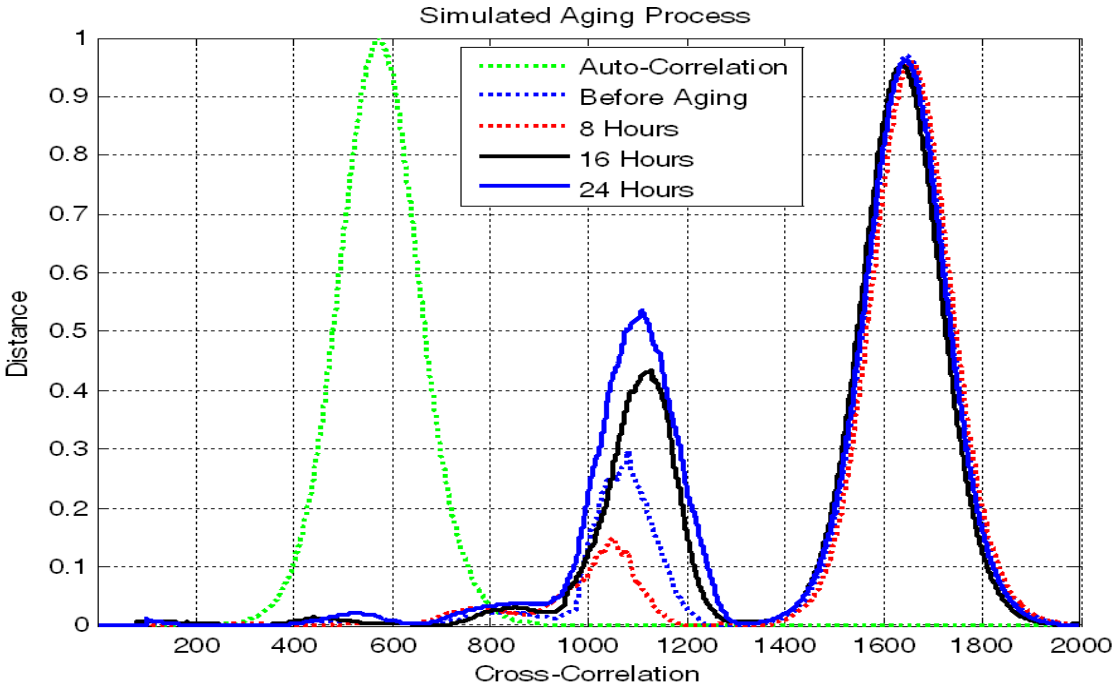

Figure 2.12: Cross correlation peak curves at progressive aging values exhibited in a sample of medium voltage MV-90 TR-XLPE insulated cable shown during temperature based accelerated aging.

an infrared surface thermometer before measurement. Cooling time, varying from 40 to 50 minutes, was allowed to prevent results from being obfuscated by other potential sources of reflectometry variation such as geometric changes of insulation and conductor materials.

Measurements were taken using an 8 GSa/s digital oscilloscope to record the raw data of each acquisition of sampled signals (incident and reflected) along with the initial reference signal. These signals were then evaluated using the JTFDR method. The results of both low voltage and medium voltage cables of similar lengths appear to so similar trend and the method seems applicable for multiple voltage levels and insulation types. Further analysis of the evaluation methods of the JTFDR method will be considered in Chapter 3 with these measurements of rapid accelerated aging forming a basis for future studies.

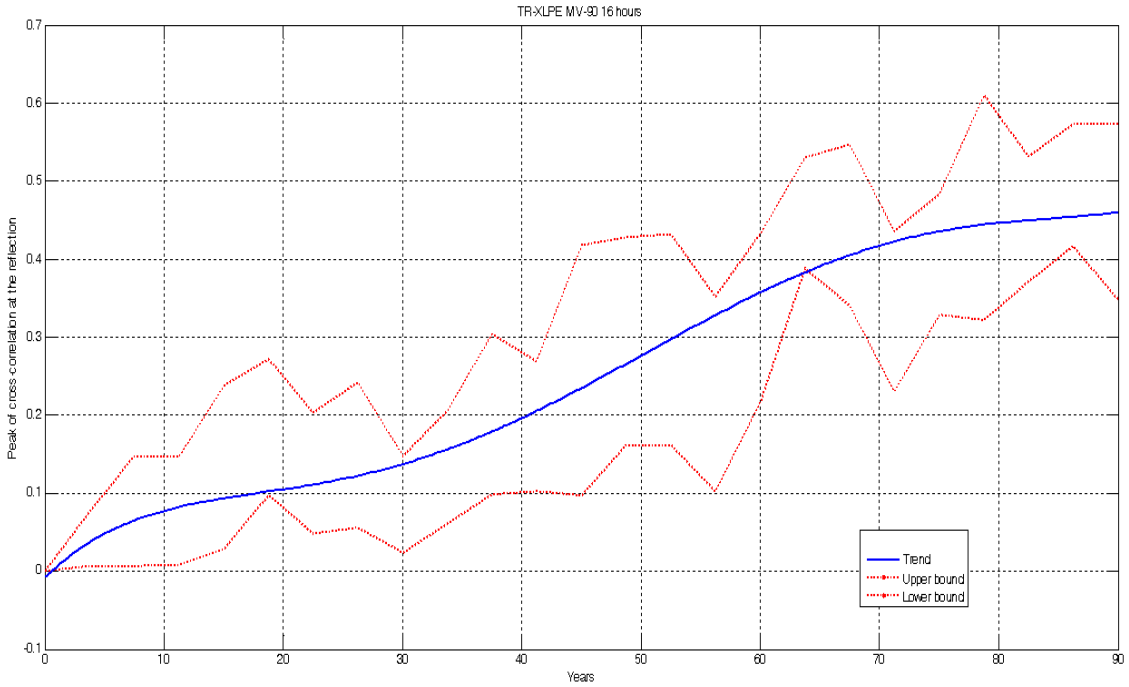

Figure 2.13: Summary of peak growth over time exhibited in a sample of medium voltage MV-90 TR-XLPE insulated cable shown during temperature based accelerated aging.

2.7 Practical Implementation of Time-Frequency Domain Reflectometry

Considering the time-frequency domain reflectometry methodology previously described and introduced, a number of practical considerations present themselves. How does the time-frequency domain reflectometry optimal reference perform along an endless cable or in absence of fault? How far can the reference signal travel in cable media? Based on time-frequency cross correlation resolution, how close can a fault be determined to the source, and what errors might be introduced if the fault resolution is too small to pick up an existing fault? What are some overall sources of error in time-frequency reflectometry?

Faulted Sections in "Endless Lines"

First, an experiment is undertaken to determine the response of the optimal reference for detection along a line that has no discernable end. In this case, the line under test was a

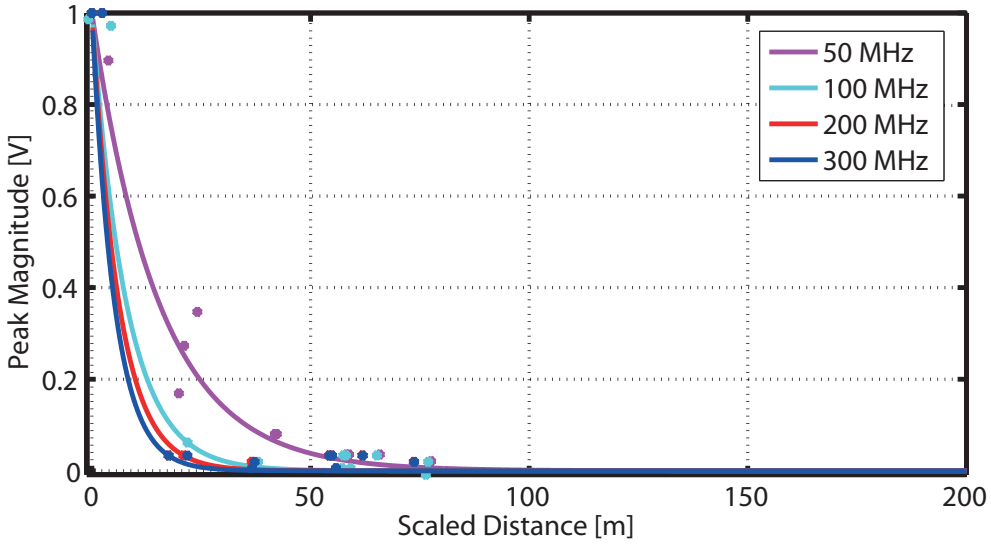

Figure 2.14: Peak ratios of incident and reflected peaks for perturbation estimate of line attenuation for 50-300MHz center frequency with 100MHz bandwidth and 60ns time duration.

cable spool of 50 meters. The cable used was a nuclear C&I coaxial cable (RG-58, 600V, XLPE-insulated, woven shield) manufactured by Habia cable. The optimal reference chosen had a 125MHz center frequency with 100MHz bandwidth for the linearly increasing chirp signal within a 60ns Gaussian envelope. This signal provides a range of approximately 30 meters of transmission in healthy cable as estimated by the perturbation method of attenuation assessment, an example of which is shown in Figure 2.14. This method essentially divides the reflected maximum peak magnitudes from raw data by the reference signal peak maximum in raw data. The maximum peaks in this case were identified by means of the TFCC algorithm and the index locations were used for obtaining the raw data peaks. The attenuation constant can then be estimated from the fitted exponential and a projected maximum readable distance is obtained from the resultant equation. The attenuation constant estimation can then be provided in either dB or $Neper/meter$.

A fault was then introduced along the line by first cutting away a narrow segment of both jacket and insulation and then shorting the inner conductor and outer outer shielding

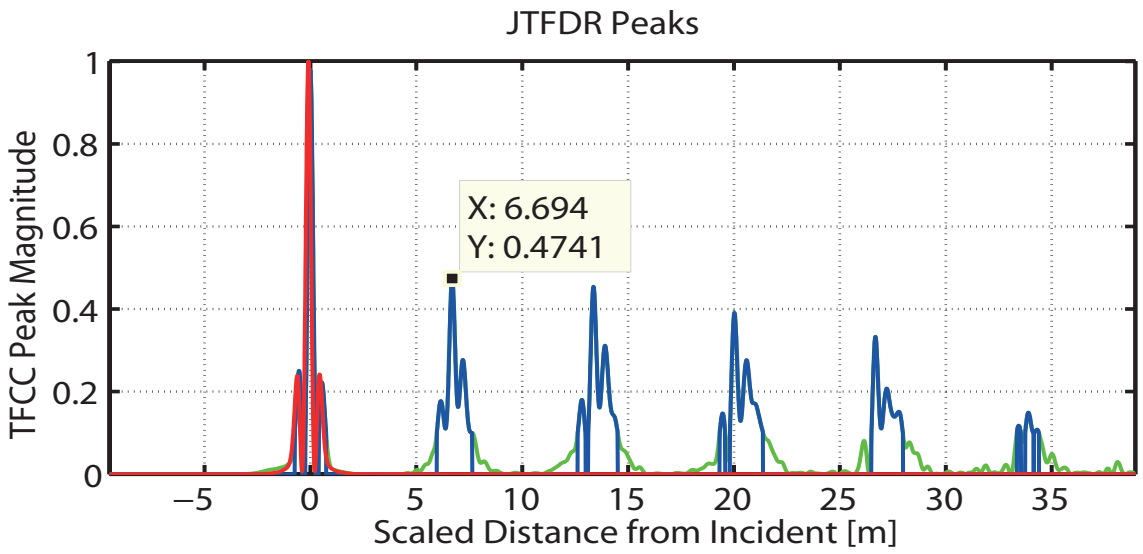

Figure 2.15: JTFDR signal is transmitted along the length of a cable spool to simulate a fault where the end of cable is not measurable, simulating an endless line.

at approximately 6.8 meters from the source of the monitoring system. Care was taken to minimize the width and depth of the cut segment of cable and a standardized short was used to introduce the fault and ensure that all frequencies were attenuated. The time-frequency cross-correlation of the incident and reflected signals was then taken to determine fault characteristics, and the results are shown in Figure 2.15. One can see from the plot that the first peak reflection is visible by the TFCC, however, this peak value is relatively weak without presence of a cable end. A total of four subsequent reflections of that same fault repeat without a clear indication of the end of the cable. This shows that a JTFDR signal could be tuned to monitor a specific segment of cable, or potentially a fault current limiter section, and provide periodic reports of a TFCC value. The signal transmitter and receiver could also be conceived as a stand-alone tester with application primarily toward fault location detection with or without a defined cable termination.

Nearest Fault Detection, Blind Spots, and Errors

Typical reflectometers are designed for more general use and not specifically to match impedance of exact cable types and models. Therefore, certain insertion losses or insertion reflections are typical. Primary methods of reducing the effect of "blind spots" include using an longer section of instrumentation test cable, double ended reflectometry for in-situ testing of cables segments, and testing a whole network of cables with multiple insertion points [62]. To assess the minimum detection range of our reflectometer system experimentally, we propagate a reference signal down an RG-58 instrumentation cable and simulated short circuit faults at varying points down the line closer to the signal injection point. We then compute the TFCC for each successive fault and try to locate the fault by scaled time-delay in our JTFDR measurement system. A baseline 7m segment was chosen with faults at 1, 2, and 3 meters. The values of 2 and 3 are not multiples of 7 and should not be seen in the confused in JTFDR measurements. Maximum peaks identified by the JTFDR algorithm are shown in green points whil those in red indicated local minima. Figure 2.16 shows the results of these tests compared to the baseline 7m segment. In each case, the minimum measurement is seen around 3 meters, however, very small secondary peaks are seen in each case at distances of 7.85 and 8.3 meters or approximating the length of the cable in addition to the faulted initial segment of 1 or 2 meters resepectively. A second fault is also seen around 9.55 meters in each test case corresponding to the initial length plus 3 meters. We would suggest a minimum length of desired detection for this signal in instrumentation cable of 3 meters or an additional instrumentation cable length to measure any potential fault closer than 3 meters from the test apparatus.

Performance of JTFDR in Networked Cable Systems

The next area of practical interest is the efficacy of JTFDR for networks of interconnected cables. Using experimental procedure similar to [62], a network of interconnected cables is constructed with three lengths of Habia manufactured, XLPE insulated, 50 Ω RG-58 wires.

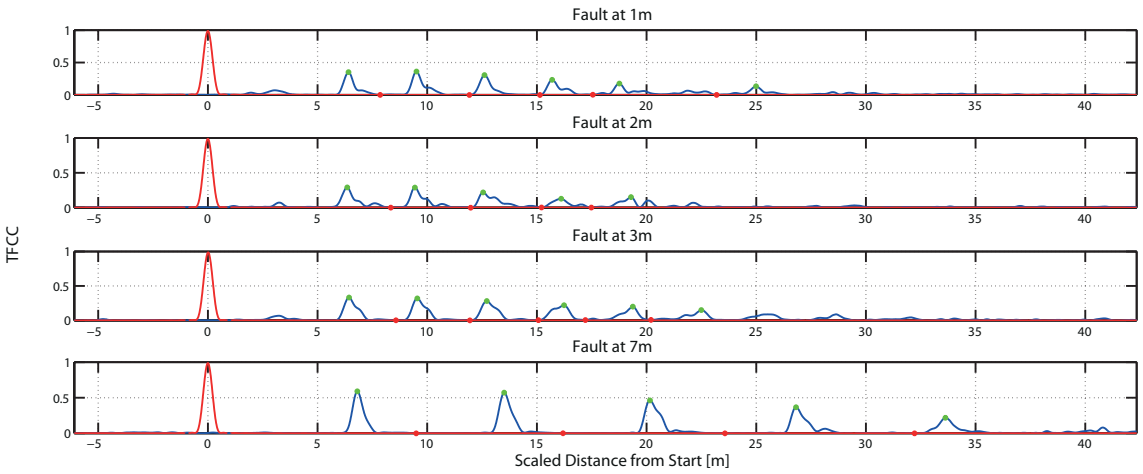

Figure 2.16: JTFDR signal is transmitted along the length of a 7 meter segment of cable to measure the closest detectable fault. The time frequency cross correlation value is shown for segments with faults at 1, 2, and 3 meters compared to the unfaulted segment.

The first cable section is 9 meters in length and a T-connector connects additional segments of 7 meters and 20 meters. We took care to test sections of cables that are not multiples of one another to allow easier interpretation of measured faults. The 7 meter segment was tested with an abrasion fault at 4 meters along its length. The goal of this test was to measure the end of all cables within the network and see the abrasion from the faulted cable segment. Additionally, in one test we provided a 5V direct current excitation source at the load end of the cable in a separate test to see the effect of loading or "online" tests on the cable. The same experimental setup of AWG and oscilloscope were utilized except with the oscilloscope probe being switched to DC coupling mode. Figure 2.17 shows the results of both of these tests (with and without DC Excitation). A schematic diagram of the simple connected network is shown below the figure to provide context and interpretation to the fault locations in the scaled TFCC metric. End locations can be seen at 9, 16, and 29 meters, and the abrasion fault can be seen at 13 meters in both offline and DC excitation cases, however, the end of the 20 meter line is harder to see due to additional reflections of the 9 and 7 meter segments and the fault on the 7 meter segment.

As a point of comparison, an additional faulted cable system is shown in Figure 2.18.

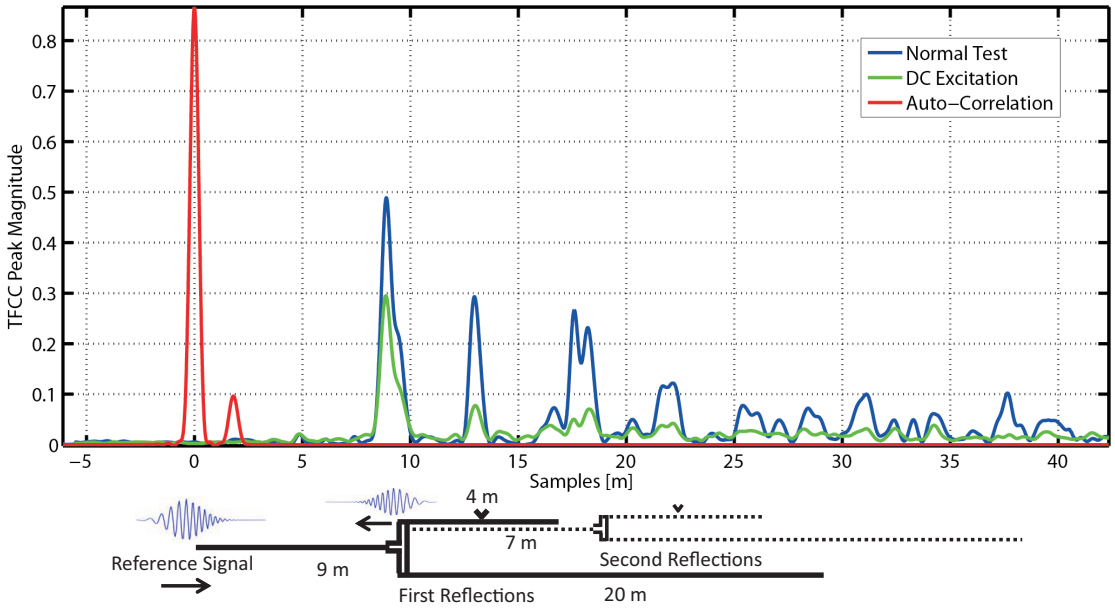

Figure 2.17: JTFDR signal is transmitted to a cable network, a T-connection of 9, 7, and 20 meter segments with an abrasion fault at 4 meters along the 7 meter segment of cable. A schematic of the wiring network is seen below the TFCC metric scaled to match the adjusted time-delay values scaled by the propagation velocity.

This figure showcases the same faulted system after the removal of the 7 meter faulted segment. Here the end of the 20 meter is more visible than previously received in Figure 2.17. We still see the repetition of the 9 meter fault at a scaled distance of 18 meters, however, we also se a greater magnitude of the TFCC metric at a scaled distance of 29 meters. Another issue of note is the indication of two separate peaks at locations of the first and second reflections of the end of the 9 meter cable. This is due to the slight impedance mismatches of the cable connectors providing addition reflections. Subsequent reflections from the end of the 20 meter segment seem further separated in time delay (scaled by velocity) and further attenuated. A comparison is shown again in these results between the system under normal test conditions and with the attached DC excitation. Again, the DC excitation lowers the overall reflected energy, however, notable features of the cable systems are still visible.

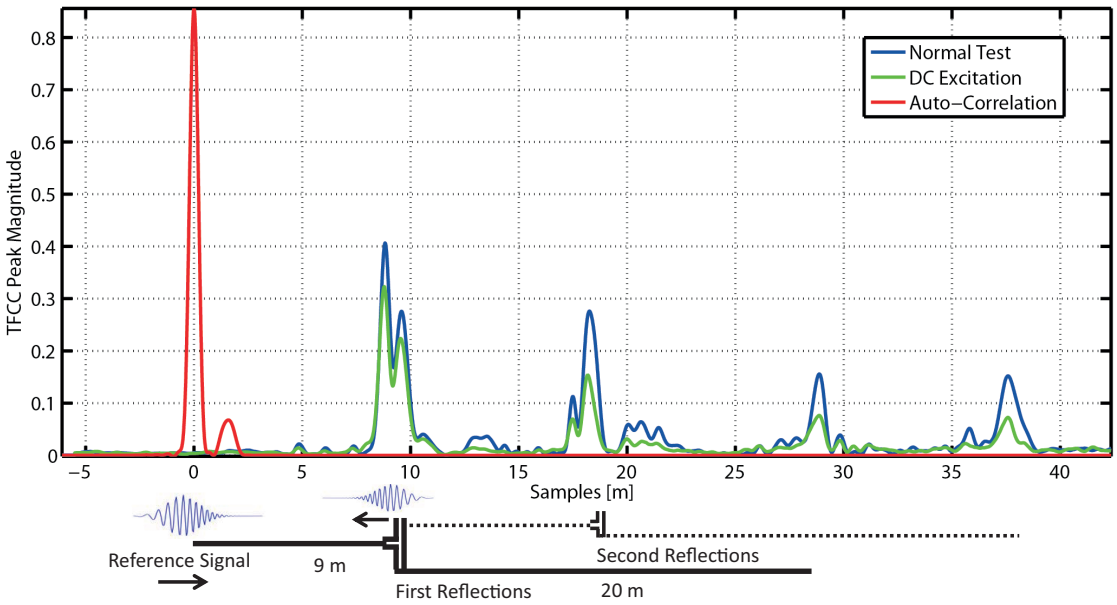

Figure 2.18: JTFDR signal is transmitted to a cable network of 9 and 20 meter connected segments with multiple simulated faults.

2.8 Conclusion

In this chapter we have presented the basic operation of Joint Time-Frequency Domain Reflectometry and presented the key considerations for selecting the optimal reference transmitted in cables and cable networks. The selection of the optimal reference has been automated with a set of cable length and type restrictions and a framework has been presented to automatically select the ideal parameters consistently to allow for better results. The assessment metrics of JTFDR have been verified for both low and high voltage cable types by rapid accelerated aging. Further practical considerations have been considered including the minimum detection distance and methods for overcoming blindspot limitations, estimation of the attenuation constant, the performance of JTFDR in cables where the end of the cable is not discernable, and the ability of JTFDR to monitor simple networks of connected cables both offline and online. Further sections will expand upon the accelerated aging performed here (Chapter 3) and use knowledge of JTFDR abilities and limitations to provide a basis for testing cables without removing them from operation (Chapter 4).

CHAPTER 3

IMPEDANCE ASSESSMENT, FAULT SIMULATION, AND EXTENDED ACCELERATED AGING IN CABLE SAMPLES

In this chapter, we will review certain limitations of the joint time-frequency cross correlation (TFCC) from previous work [53, 56] and propose clarifying impedance estimation and statistical methodology to mitigate constraints within previous implementations of the algorithm. Towards this end considerations will be taken to understand, from both an RF and digital signal processing perspective, the interactions of different reflections from fault points such as the open circuit at the end of a cable, a short circuit, or a localized change in impedance brought on by accelerated aging. Increased understanding of the distribution of reflected energy within subsequent reflections of the propagating signal in cable medium will then lead to algorithms to analyze the associated peaks and time delays determined by the TFCC algorithm. The trends established by previous aging routines will then be explored with these guiding principles. Methodology will be provided to better interpret and represent the impedance based changes in a cable under accelerated aging or other induced faults to provide a tenable physical interpretation of the TFCC results. These proposed improvements to the TFCC-based metric will then be implemented in a new accelerated aging study that will provide a more realistic basis for assessment of soft or invisible impedance faults.

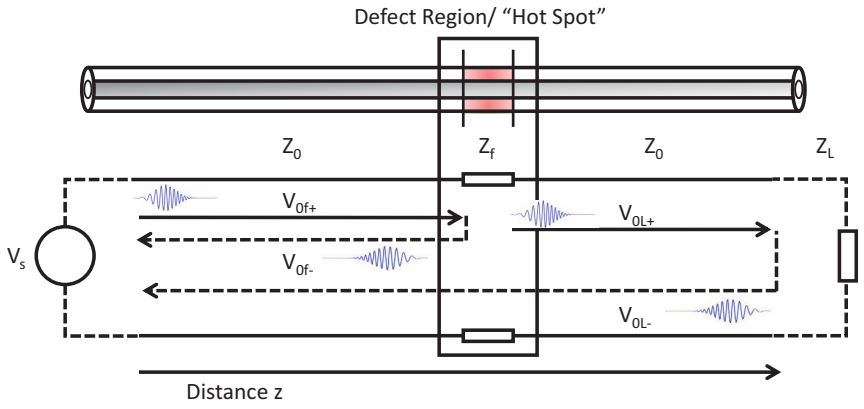

Figure 3.1: Schematic model of a cable with defect or hot-spot.

3.1 Hard and Soft Faults

In order to understand the impedance of a fault and related terminology a brief introduction will be given to the concept of what we will call “hard” and “soft” faults. Hard faults are typically interpreted as faults visible to the human eye or upon inspection of cable. Examples include detached connectors, corrosion, abrasion or severing of connected cables, and some types of water damage. These may lead to an open, short, or intermittent fault. Soft faults, however, may be invisible to manual inspection and include some forms of heat damage, fraying, damage within conduit or underground segments, or early failure due to thermal, radiation, or other environmental stressors. Depending on their severity, either hard or soft faults may go undetected by conventional manual inspections or even metered inspections such as TDR or FDR assessments for cable damage. It is important to take a closer look at varying levels of hard and soft faults as different failure modes for cable systems. Through the lens of fault detection and classification by reflectometry, we can examine more closely the present strengths and limitations of using the time-frequency cross-correlation metric for assessing cable failures.

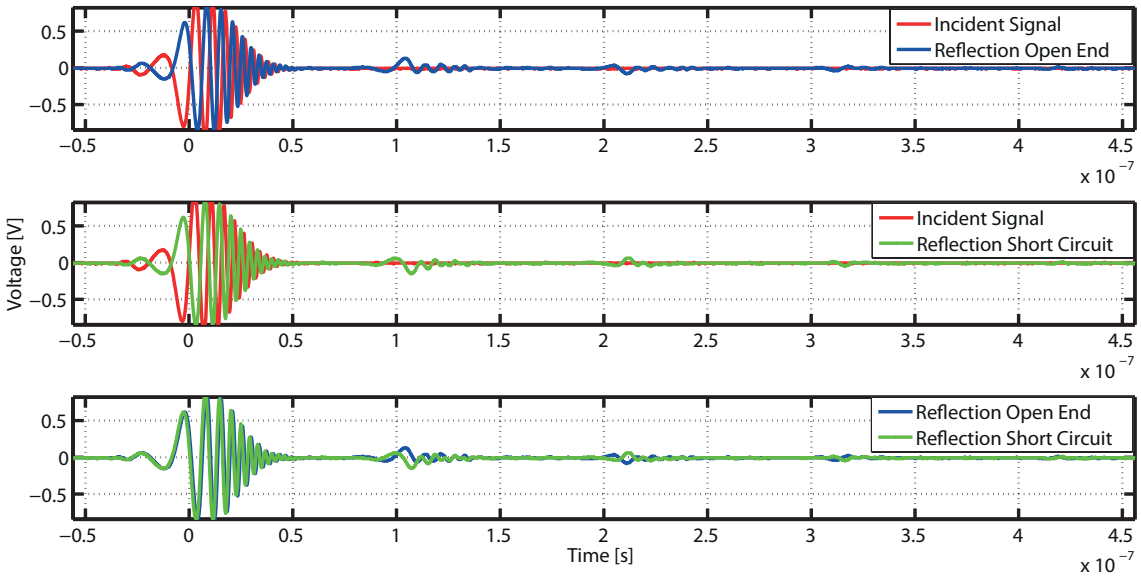

Figure 3.2: Incident and reflected signals in the event of open and short circuit faults using the optimal reference signal show a difference in phase

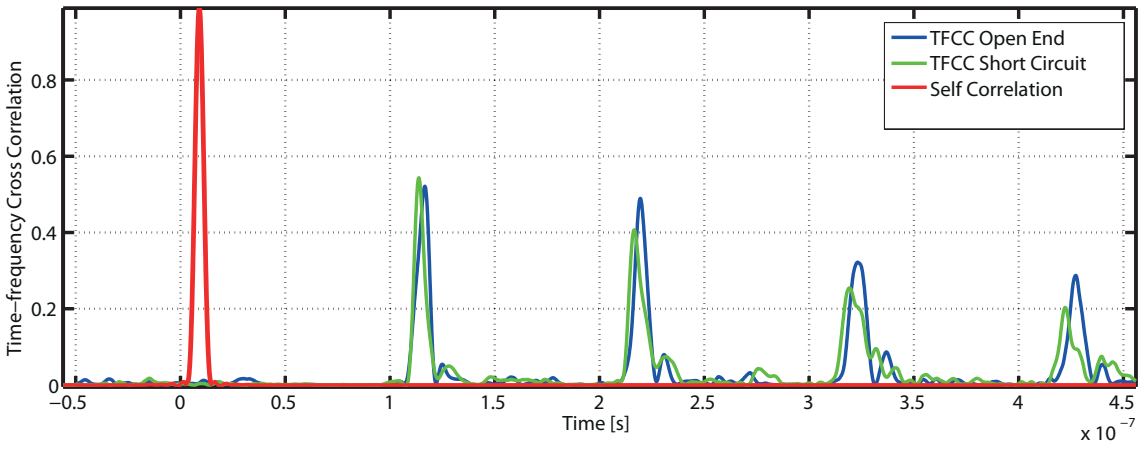

Figure 3.3: Time-frequency cross-correlation metric used for JTFDR falls short when comparing open and short faults due to a lack of phase information in the typical representation.

First, attention should be paid to the distinctions, or rather lack there of, between the two most extreme or most visible cases of cable faults: open and short circuit faults. A simplified diagram of the types of faults typically measured through reflectometry is shown in Figure 3.1. A comparison shown in 3.2 between open and short type faults for a nuclear C&I cable (RG-58, 600V, XLPE-insulated, woven shield) manufactured by Habia cable.

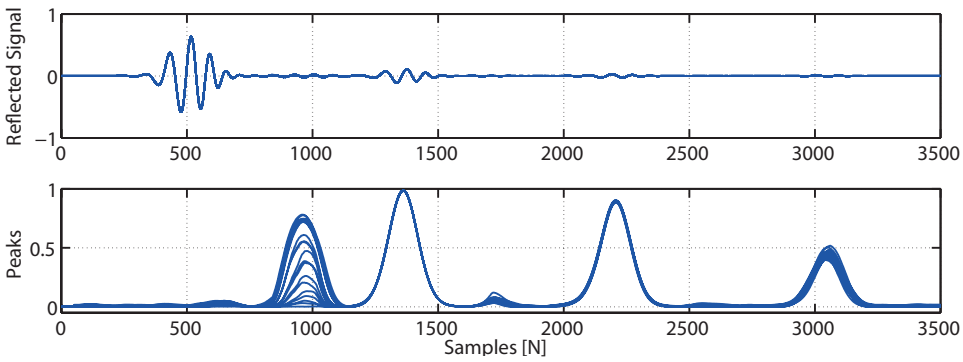

Figure 3.4: Measurement of the growth of the TFCC with a linear increase in a fault simulated at 5 meters. The fault signal for the 5 meter region is simply a scaling of the actual signal obtained from the aging of an XLPE insulated sample by a linearly increasing multiplier.

Figure 3.2 highlights an analysis of response of this cable to the optimal reference signal in the time-domain. Here differing phase can be found in the reflected signal encountering a standardized short circuit connector compared to the open end of the cable. However, when we analyze the fault by means of magnitude only time-frequency cross-correlation as shown in Figure 3.3, the differences in phase of the fault are not preserved and the metric fails to quantify the fault in a means typically expected by TDR in terms of inductive or capacitive faults. We can clearly see now the motivation for seeking an impedance estimating metric for localized changes in impedance by considering the desire to qualify faults and allowable fault severity before condition-based maintenance action. It should be noted that as evidenced from Section 2.6 differences in magnitudes of faults can seen from both low voltage and medium voltage cable types, however, specific estimation of inductive or capacitive faults is not available without looking at phase differences between the time-frequency representation of the reference signal and the reflected signal.

Simulation of Aging Growth by Historical Data

As a means of initial assessment of varying changes in impedance, a simulation based on historical accelerated aging implemented in Fig. 2.9 of Section 2.6 will compare the growth

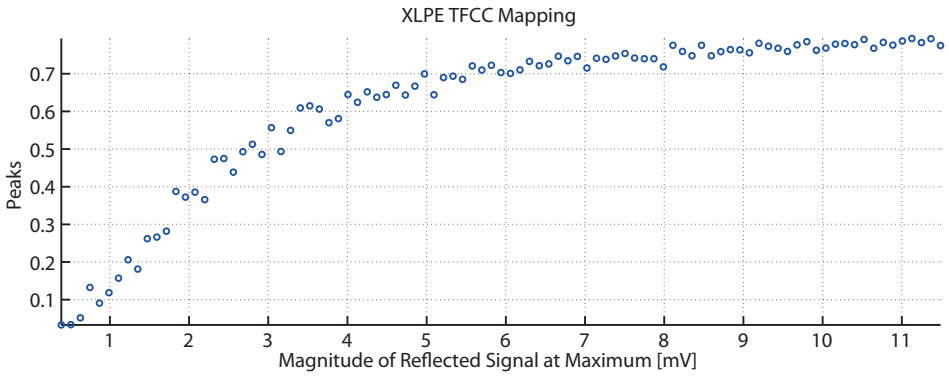

Figure 3.5: Measurement of the growth of the TFCC with a linear increase in a fault simulated at 5 meters. The fault signal for the 5 meter region is simple a scaling of the actual signal obtained from the aging of an XLPE insulated sample by a linearly increasing multiplier.

of the TFCC peak with the increase of peak magnitude in a segment of the reflected signal corresponding to the length of the hotspot. The goal here is to estimate the relationship of increases in the soft fault TFCC peak based on variations in magnitude of the reflected signal obtained experimentally before determining a mathematical relationship. Figure 3.4 shows graphically the experimental setup utilized for simulating increases in soft fault peaks due to accelerated aging. The historical reflected signal from the ending point of accelerated aging is used a reference and scaled within the given horizontal window corresponding to the length of the corresponding Gaussian envelope. These relationships can then be further studied to determine the contribution of one pass of the reflected signal through the cable medium and a subsequent return, or in other words multiple reflections of the same signals. Three figures represent respective simulated linear growth rates of the accelerated aging experiments for XLPE, EPR, and SIR insulated materials subjected to accelerated aging shown in Figures 3.5-3.7. Focus is placed on the XLPE accelerated aging because further experimentation is continued with this cable type at lower accelerated aging temperatures later in this work and the trends established provide a framework for interpretation of the variations in TFCC metric.

This shows that the essentially linear increase of the reflection magnitude is expressed

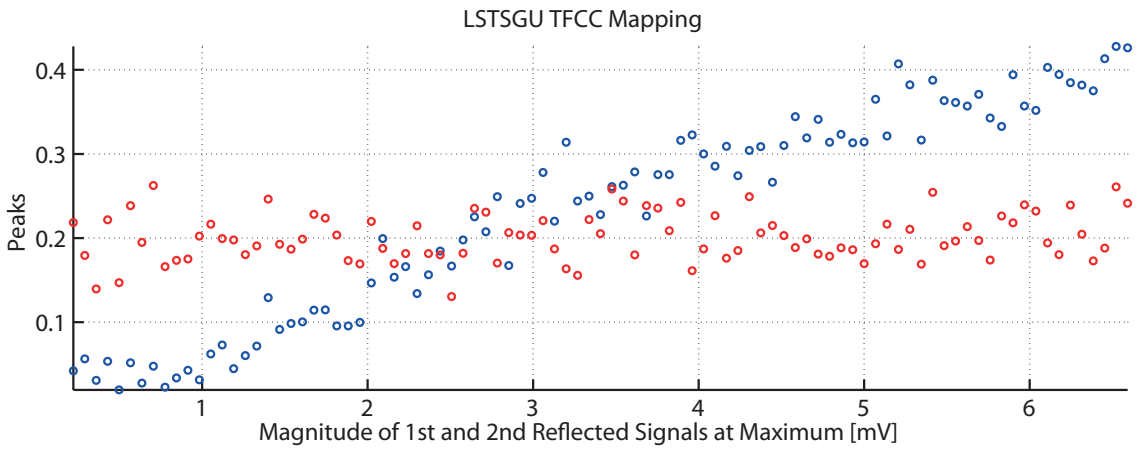

Figure 3.6: Measurement of the growth of the TFCC with a linear increase in a fault simulated at 5 meters. The fault signal for the 5 meter region is simple a scaling of the actual signal obtained from the aging of an LSTSGU insulated sample by a linearly increasing multiplier.

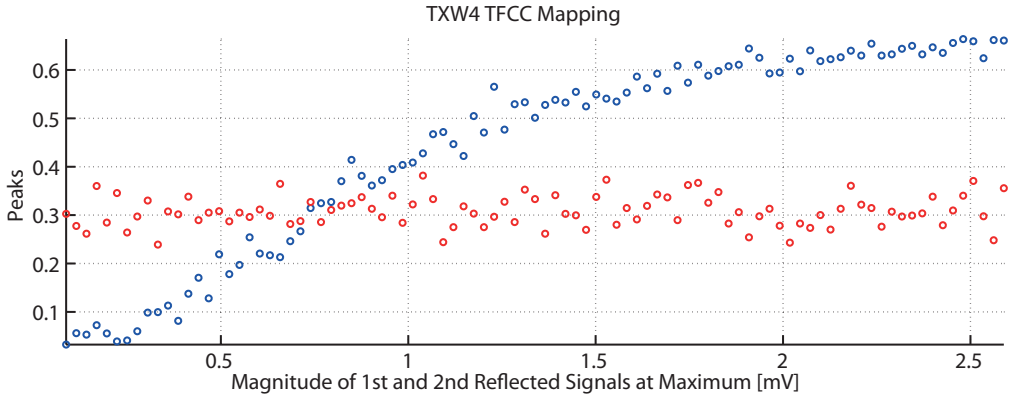

Figure 3.7: Measurement of the growth of the TFCC with a linear increase in a fault simulated at 5 meters. The fault signal for the 5 meter region is simple a scaling of the actual signal obtained from the aging of an TXW4 insulated sample by a linearly increasing multiplier.

by the JTFDR metric as an exponential growth due to mapping of the transformations imposed by the TFCC calculations. These calculations are performed in two parts with an initial time-frequency distribution formed by a windowed Fourier transform and then calculations of time-frequency cross distributions. Owing to the dependency on the cross distributions, mapping of reflected signal maximum peak due to fault will vary from reference signal to reference signal and thus also from material to material (due to the fact

that the reference signal is tailored to each individual cable type and to a lesser extent cable length). The cross-correlation employed here still provides an attenuation of noise and other desirable features, however, by looking to the phase information provided by the TFCC and other properties such as the energy of the incident and reflected signals also obtainable by the TFCC, we can refine the metric to better categorize some types of faults.

Aging Detection by Cross-Correlation Peak

Now that we have observed an experimental determination of the relationship between the magnitude of the reflected voltage and that of the TFCC peaks, we can look further at the equations and theory defining these phenomena. We will use the simplifying assumption that the kernel selected for the determination of the time-frequency distribution is that of the Wigner distribution described in (1.3) and(1.6). This allows for simpler calculation of the TFD in derivations, and the effect of the cross-terms induced by the simpler kernel is minimized by the nature of this type of reflectometry. The primary purpose of the chirp frequencies is in the ease of detecting an aggregate of single frequencies in a dispersive medium which attenuates frequencies differently. We are essentially looking for the least attenuated set of narrowband signals to form the cross-correlation peak and the cross-terms between the received frequencies will be averaged in processing . The JTFDR algorithm from (1.20)then computes the time-frequency cross correlation between an incident signal and the reflected signal through a propagating medium.

We will consider the simple transform pair:

$$s(t) \rightleftharpoons W(t,\omega) \tag{3.1}$$

Time and frequency shift properties as provided by Cohen [35], show that for a time domain signal, $s(t)$, from 2.4 with a Wigner Transform given as the following bivariate distribution, $W(t,\omega)$, a shift in time and frequency given by:

$$s(t) \rightarrow e^{j\omega_0 t} s(t - t_0) \tag{3.2}$$

A subsequent shift in time and frequency is seen in the Wigner Distribution:

$$W(t,\omega) \rightarrow W_1(t - t_0, \omega - \omega_0) \tag{3.3}$$

Using this simplified assumption we can take the Wigner transform of the simplified optimal reference and form a derivation of this distribution:

$$W_s(t,\omega) = \frac{1}{2\pi}\left(\frac{\alpha}{\pi}\right)^{1/2} \int e^{-\frac{\alpha(t-\frac{1}{2}\tau)^2}{2} - j\frac{\beta(t-\frac{1}{2}\tau)^2}{2} - j\omega_0(t-\frac{1}{2}\tau)} \cdot e^{-\frac{\alpha(t+\frac{1}{2}\tau)^2}{2} + j\frac{\beta(t+\frac{1}{2}\tau)^2}{2} + j\omega_0(t+\frac{1}{2}\tau)} \cdot e^{j\tau\omega} \cdot d\tau \tag{3.4}$$

$$W_s(t,\omega) = \frac{1}{2\pi}(\frac{\alpha}{\pi})^{1/2} \int e^{-\frac{\alpha(t^2-\tau t+\frac{1}{4}\tau^2)}{2} - j\frac{\beta(t^2-\tau t+\frac{1}{4}\tau^2)}{2} - j\omega_0(t-\frac{1}{2}\tau)} \cdot e^{-\frac{\alpha(t^2+\tau t+\frac{1}{4}\tau^2)}{2} + j\frac{\beta(t^2+\tau t+\frac{1}{4}\tau^2)}{2} + j\omega_0(t+\frac{1}{2}\tau)} \cdot e^{j\tau\omega} \cdot d\tau \tag{3.5}$$

The improper integral can be manipulated into the following form for an express solution:

$$\int_{-\infty}^{\infty} e^{-(a\tau^2+b\tau+c)} d\tau = \sqrt{\frac{\pi}{a}} e^{\frac{b^2-4ac}{4a}} \tag{3.6}$$

Reexpressing the improper integral we obtain:

$$W_s(t,\omega) = \frac{1}{2\pi}\left(\frac{\alpha}{\pi}\right)^{1/2} \int_{-\infty}^{\infty} e^{-(\frac{1}{4}\alpha\tau^2 + j(\omega-\beta t-\omega_0)\tau + \alpha t^2)} d\tau \tag{3.7}$$

Further simplifying, we obtain:

$$W_s(t,\omega) = \frac{1}{\pi} \cdot e^{\frac{(j(\omega-\beta t-\omega_0))^2 - \alpha^2 t^2}{\alpha}} \tag{3.8}$$

$$W_s(t,\omega) = \frac{1}{\pi} \cdot e^{\alpha t^2 - \frac{(\omega-\beta t-\omega_0)^2}{\alpha}} \tag{3.9}$$

$$C_{sr}(t) = \frac{1}{E_s E_r(t)} \int_{t'=t-T_s}^{t'=t+T_s} \int W_r(t',\omega) W_s(t'-t,\omega) d\omega dt' \tag{3.10}$$

where $W_r(t,\omega)$ is the Wigner distribution of the reflected signal; $W_s(t,\omega)$ is the Wigner distribution of incident signal; and E_s and $E_r(t)$ are normalization factors related to signal energy. The Wigner distribution of the optimal reference given in (2.1) and that of a time displaced reflected signal are given below as W_s and W_r respectively:

$$W_s(t,\omega) = \frac{1}{\pi} e^{-\alpha(t-t_0)^2 - (\omega - \beta(t-t_0) - \omega_0)^2/\alpha} \tag{3.11}$$

$$W_r(t,\omega) = \frac{1}{\pi} e^{-\alpha(t-z/v)^2 - (\omega - \beta(t-z/v) - \omega_0)^2/\alpha} e^{-2Az\omega} \tag{3.12}$$

Here in (3.12), the attenuation is estimated as an exponential coefficient with decay terms $-2Az\omega$ where $2z$ is the distance traveled by the reflected wave and A is an approximation of the attenuation constant of the cable. We now substitute (3.11) and (3.12) into (3.10) to obtain:

$$C_{sr}(t) = \frac{2}{E_s E_r(t)} \int_{t'=t-T_s}^{t'=t+T_s} \int_{-\infty}^{\infty} e^{-\alpha(t'-z/v)^2 - (\omega - \beta(t'-z/v) - \omega_0)^2/\alpha} \cdot e^{-2Ax\omega} e^{-\alpha(t'-t)^2 - (\omega - \beta(t'-t) - \omega_0)^2/\alpha} d\omega dt' \tag{3.13}$$

The reflected energy E_r is defined as:

$$\begin{aligned} E_r &= \int_{t'=t-T_s}^{t'=t+T_s} \int_{-\infty}^{\infty} W_r(t',\omega) d\omega dt' \\ &= e^{-(\alpha^2+\beta^2)/\alpha A^2 z^2 - 2Az\omega_0} \\ &= e^{-2Az(\omega_0 - \delta\omega/2)} \end{aligned}$$

The reference energy E_s is normalized to a value of $E_s = 1$. We substitute back into (3.13) to obtain:

$$C_{sr}(t,\omega) = e^{-(\alpha^2+\beta^2/2\alpha)(Az)} \cdot e^{-(\alpha^2+\beta^2/2\alpha)(t-z/v)^2} \tag{3.14}$$

$$C_{sr}(t,\omega) = e^{-(\alpha^2+\beta^2/2\alpha)(Az+(t-z/v)^2)} \tag{3.15}$$

This last equation governs the relationships shown experimentally in Section 3.1 as a Gaussian function of smaller magnitude than the autocorrelation of the reference signal. In presence of multiple faults, superposition applies and multiple Gaussian functions can be seen at delayed time instances, however, some confusion may arise if faults are too close together or if there are multiple reflections that overlap in locations of multiples of the same distance.

3.2 Variation of Reference Envelope

Having shown some limitations of the current optimal reference signal, a set of variations of this signal is now considered. We will look to vary the envelope function of the optimal reference described in Section 2.3. We consider the possibility of taking the derivative of the Gaussian function and show some new detection properties opened by this choice. First, we will show the envelopes and then the chirp signals enclosed within them Figures 3.2 and 3.2.

Solving the generalized envelope function, $\psi(t,\omega)$, for a Gaussian derivative, we use the following envelope:

$$\psi(t,\omega) = (t_0 - \alpha t) \cdot e^{-\alpha(t-t_0)^2/2} \tag{3.16}$$

This solves to the following expression:

$$s(t) = (\alpha/\pi)^{1/4} \cdot (t_0 - \alpha t) \cdot e^{-\alpha(t-t_0)^2/2 + j\beta(t-t_0)^2/2 + j\omega_0(t-t_0)} \tag{3.17}$$

Additional derivatives of the Gaussian window follow Hermite polynomials and are solved below for the second and third derivative of the Gaussian function. The enveloping

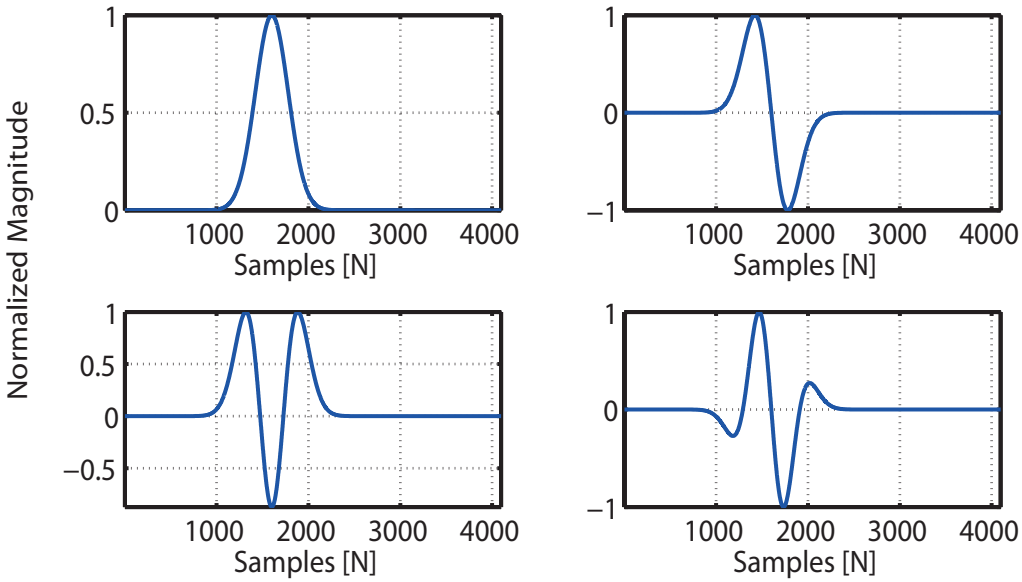

Figure 3.8: Alternative enveloping functions for the chirp signal based on the derivative of the gaussian function. (a) gaussian envelope, (b) first derivative of gaussian, (c) second derivative of gaussian, and (d) third derivative of gaussian

function is given along with the full signal with chirp signal first for the second derivative function,

$$\psi(t,\omega) = (\alpha^2(t_0-t)^2 - \alpha/2)\cdot e^{-\alpha(t-t_0)^2/2} \tag{3.18}$$

$$s(t) = (\alpha/\pi)^{1/4}\cdot(\alpha^2(t_0-t)^2 - \alpha/2)\cdot e^{-\alpha(t-t_0)^2/2+j\beta(t-t_0)^2/2+j\omega_0(t-t_0)} \tag{3.19}$$

followed by the third derivative functions,

$$\psi(t,\omega) = (-\alpha^3(t_0-t)^3 + 3\alpha^2(t_0-t))\cdot e^{-\alpha(t-t_0)^2/2} \tag{3.20}$$

$$s(t) = (\alpha/\pi)^{1/4}\cdot(-\alpha^3(t_0-t)^3 + 3\alpha^2(t_0-t))\cdot e^{-\alpha(t-t_0)^2/2+j\beta(t-t_0)^2/2+j\omega_0(t-t_0)} \tag{3.21}$$

The Wigner distribution of the first derivative of Gaussian function enveloping the chirp signal is derived from (1.6) and (3.11) and given below:

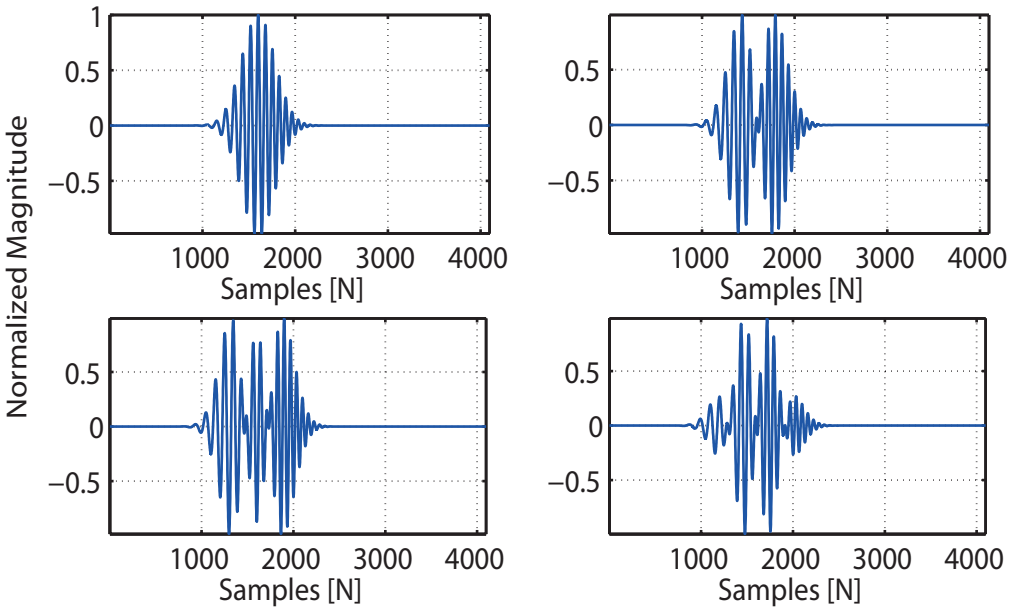

Figure 3.9: Alternative reference signals for JTFDR with an enveloped chirp signal based on the derivative of the gaussian function. (a) gaussian envelope, (b) first derivative of gaussian, (c) second derivative of gaussian, and (d) third derivative of gaussian

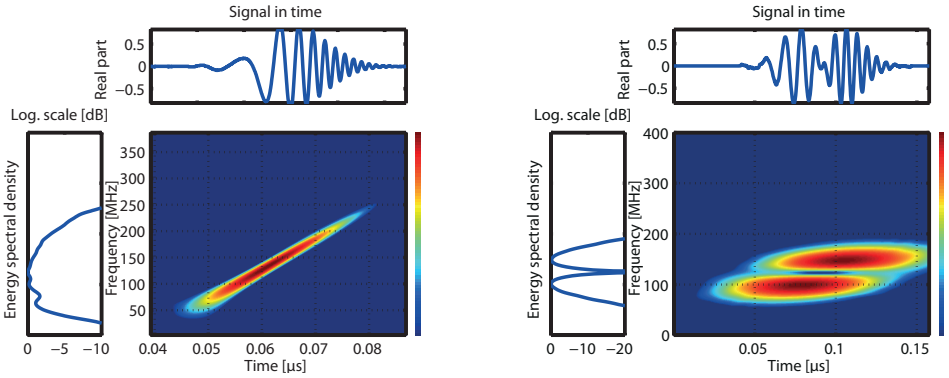

Figure 3.10: Time-frequency distribution of (a) optimal reference and (b) reference with derivative of gaussian function as envelope.

$$W_s(t,\omega) = \frac{1}{\pi}\left[\frac{\alpha^2-\beta^2}{\alpha}(t_0-t)\frac{1}{\alpha}(\omega_0-\omega)\right] e^{-\alpha(t-t_0)^2-(\omega-\beta(t-t_0)-\omega_0)^2/\alpha} \tag{3.22}$$

The time frequency representations of these variations of the Gaussian envelope can be seen in Figures 3.10 and 3.11.

Our ultimate goal for this set of variations to the reference signal is to provide better

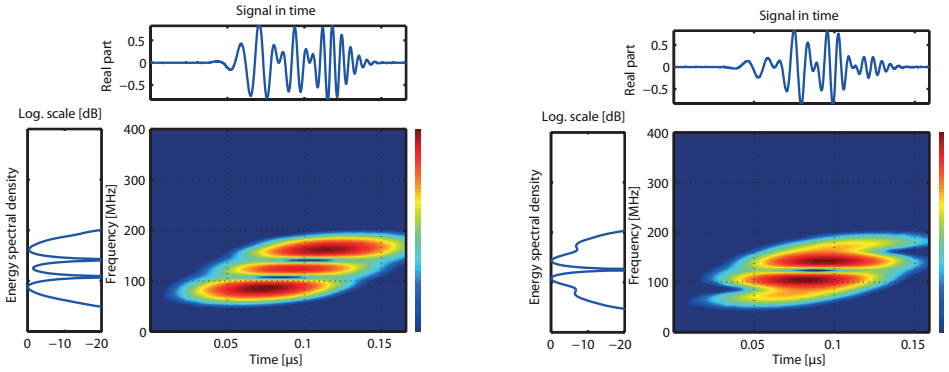

Figure 3.11: Time-frequency distribution of (a) optimal reference with second derivative of gaussian function as envelope and (b) reference with third derivative of gaussian function as envelope

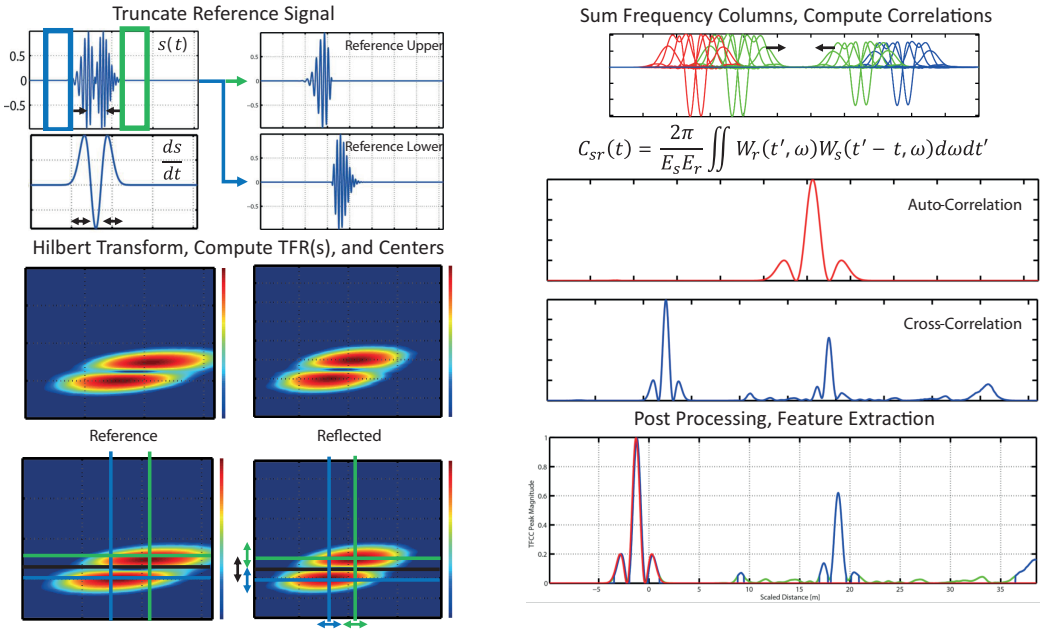

Figure 3.12: Summary and visualization of the new time-frequency cross-correlation algorithm obtained for the variation of the Gaussian envelope.

utility in fault detection in the time-frequency domain. We thus partially remove the center frequency while at the same time introducing a phase discontinuity at the previous time center of the Gaussian chirp signal. We allow for more defined detection of the phase difference between incident and reflected signals for impedance estimation and fault location detection in general. The new reference provides us with an additional pair of peaks for

each hard fault to allow for better rejection of false positives.

We summarize the new time-frequency cross-correlation algorithm for this split packet optimal reference signal in Figure 3.12. As previously seen in Figures 2.4 and 2.5, we start by truncating our measured reference signal. We identify local characteristics by computing a derivative of the envelope only and measure the distance between min and max of this second derivative of Gaussian function to identify the truncation length. We then separate the upper and lower reference packets of chirp signal enveloped by a separate "lobe" of the Gaussian derivative envelope. These two signals along with the full signal are now compared to the reference signal. This comparison is accomplished by computing the Hilbert transform and subsequent time-frequency representations of the signal using the spectrogram kernel. Next, we calculate time and frequency centers and the sum of frequency columns in the time domain. From these computed frequency columns we can compute and normalize the auto- and cross-correlations of reference and reflected signal. We then threshold the data according to the specific background defects of the baseline cable sample and scale correlation lag or time variable by the velocity of propagation of the cable medium. We present the results of the three different scalings of the reference signal and related cross- and auto-correlations in Figures 3.13-3.14

3.3 Improvements of Experimental Set-up

As part of collaboration with the International Atomic Energy Agency (IAEA), improvements to the testing setup at the University of South Carolina were implemented to further simulate a cable test environment closer to that experienced in a nuclear power plant cable tray. This updated configuration includes cable tray sections, stressing bends in the test cable, feeding segments in conduit, and more realistic heating models for advanced aging. The updated configuration is summarized in Figure 3.3. Cables will be tested with advanced aging protocol under this industrial settings testbed as well as with a control group tested without added stresses.

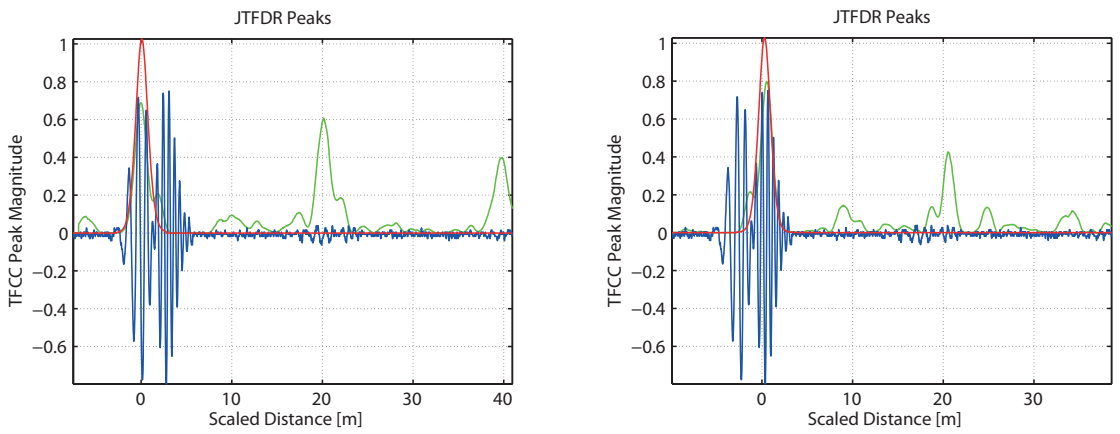

(a) (b)

Figure 3.13: Time-frequency cross correlation peaks generated by measure between individual windowed reference peaks and the reflected signal for 20 meter undamaged RG-58 cable segment (a) with the left-most reference peak (b) with the right-most reference peak with overlayed reflected signal.

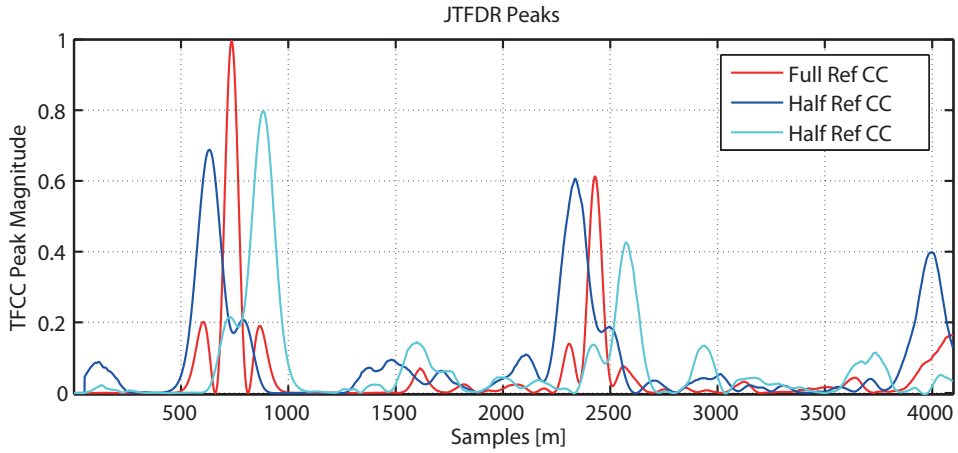

Figure 3.14: A closer view of the time-frequency cross correlation peaks generated by the measure between individual windowed left-most and right-most reference peak and the reflected signal.

Initial accelerated aging tests focused on testing a wide range of instrumentation cables quickly enough to produce results and facilitate comparison of JTFDR to other more established methods. However, certain fallacies exist in this short time test. As explained in (2.8), a mathematical relationship exists between an accelerated aging time and a service life time based upon heating temperature and the activation energy. From further research, it has been determined that previous estimations of cable activation energy for cross-linked

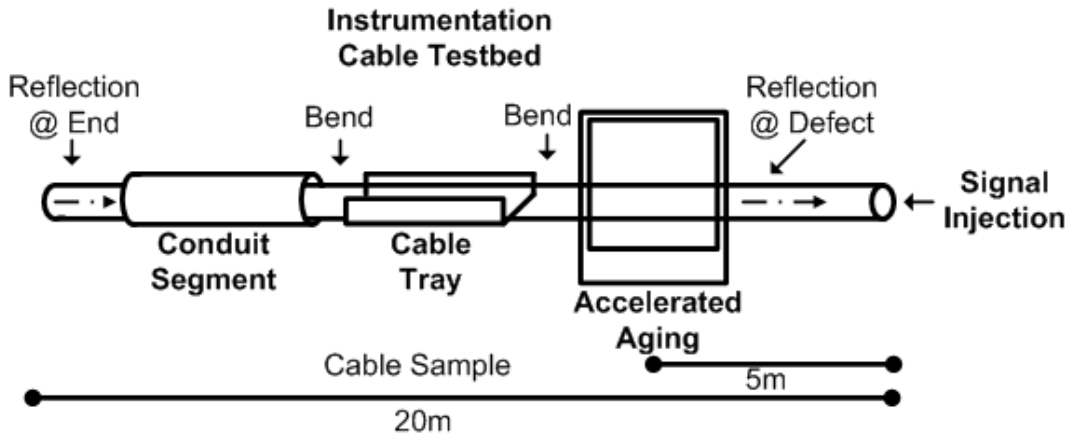

Figure 3.15: Experimental setup for JTFDR in a nuclear plant environment including conduit and cable tray segments.

polyethylene (XLPE) at 1.33eV may be too high. Similarly, the aging temperature may be too high to provide an accurate accelerated aging model. As such, a new set of aging parameters specifically for accelerated aging for XLPE-insulated instrumentation level cable, such as a sample received from Swedish manufacturer Habia Cable. As further cable samples are received from IAEA member manufacturers in the United States and internationally, a homogenized or normalized baseline can be developed for nuclear instrumentation and future standards could be developed around JTFDR-based metrics where previously TDR or FDR metrics dominated.

An accelerated aging test was performed for measuring damage to RG-58 cable over the course of 916 hours corresponding to approximately 30 years of actual service aging. This aging was performed in two separate stages to allow for a more complete view of the aging process over the course of a certification period of a nuclear power plant. The first stage was a slower process at a lower temperature of 115C. This stage makes up the first 304 hours of the test study. The second stage was accomplished at 130C for an additional 612 hours to allow a more observable real time span within a lab environment (under 2000 hours). The modified Arrhenius equation with a summary of actual parameters for the accelerated aging test follows is provided in 2.8 where the following hold true:

T_a is the accelerated aging temperature (varying from 115 to 130C over the span of

aging);

T_s is the service temperature (an average room temperature);

t_a is the aging time at acceleration temperature (a total of 916 hours in a heating chamber);

t_s is the aging time at service temperature (a total of 30 years simulating a certification time for many nuclear power plants);

E_a is the activation energy of the material (assumed to be comparable to other RG-58 cables around 13kcal/mol or 0.564 eV);

B is the Boltzmann's constant (given in 2.9), This relationship provides an estimate of the rate of chemical reactions typically for a single reaction type, and while limited in scope, it is a common assessment in quality testing of cables [48]. The maximum aging temperature of 130C is chosen as it is the maximum listed operating temperature of the cable for intermittent operation while expected delinkages of the cross-linked polyethylene bonds begin around 115 to 120C [68].

This accelerated aging was measured by the metrics described in Section 2.2. Figures 4.4 and 4.5 describe the overall function of the hardware for JTFDR in these experimenst showing the actual setup and a system function diagram. Two "hot spots" were simulated for localized heating or aging at 5 and 15 meters respectively along the length of the cable.

3.4 Imaging of Baseline and Aged Samples

The aged cables at low aging temperature (115C) were analyzed by X-ray computed tomography (CT) to determine whether notable insulation and cable damaged had occurred over the duration of the previously described aging test. Noticeable differences can be seen between the baseline samples left unexposed to accelerated aging and those subjected to accelerated aging. These results are shown with side-by-side comparisons in Figures 3.16-3.18. The insulation material has degraded along the length of the cable with measurements of cable diameter after heating and cooling also decreasing slightly over the

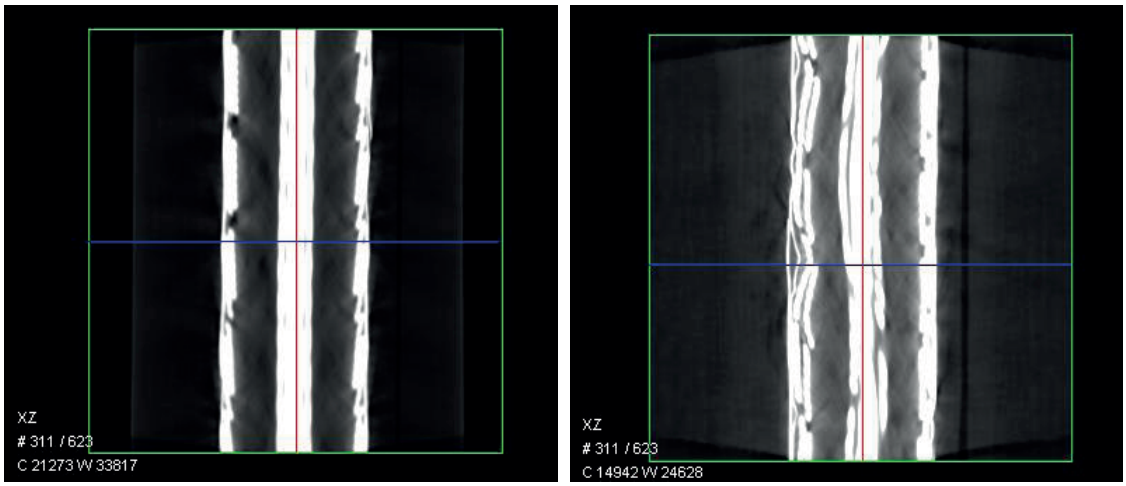

Figure 3.16: X-ray CT images of the RG-58 cable comparing baseline sample and a segment aged at an accelerated rate to simulate 9 years of service.

course of aging.

The aged cables from the test at low aging temperature (115C) were analyzed in 10cm segments by X-ray CT to determine whether notable insulation and cable damage had occurred over the duration of the previously described accelerated aging procedure at the defect inception site. Noticeable differences can be seen between the baseline samples left unexposed to accelerated aging and those subjected to accelerated aging. These results are shown with side-by-side comparisons in Figures 3.16-3.18. Figure 3.16 shows the XZ transverse sectional area of the cable where the conductor and woven shielding of the instrumentation cable are highlighted as the white portions of the image while the XLPE insulation is shown as the darker portion. Compiled in Figures 3.17 and 3.18 are three-dimensional representations of the cable under test with cross and transverse sections. The insulation material has degraded along the length of the cable with the stranded conductor twisting within its shielding. Measurements of cable diameter also decreased slightly after heating and cooling over the course of aging.

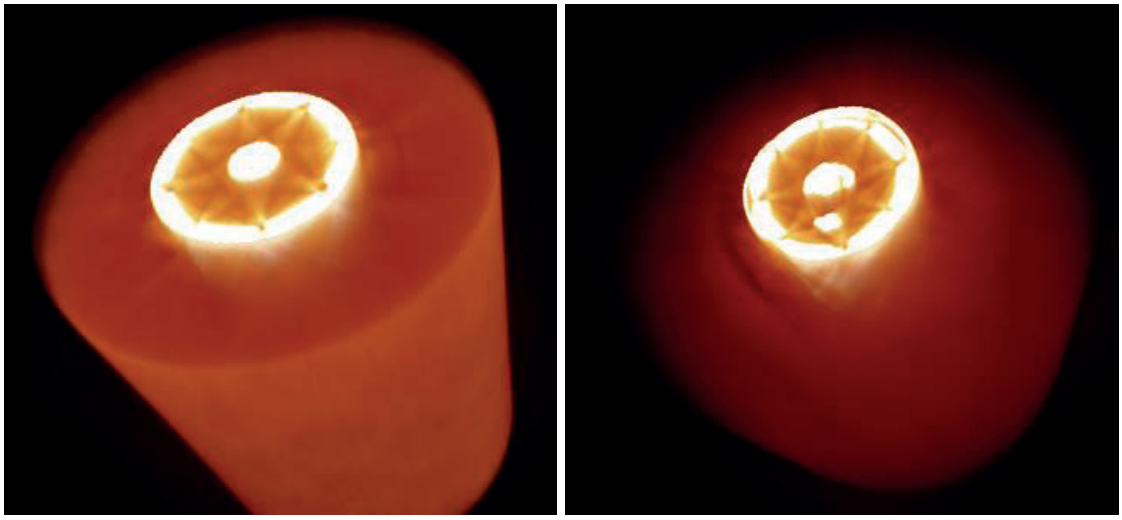

Figure 3.17: Cross-sectional 3-dimensional x-ray CT images of the RG-58 cable comparing baseline sample and a segment aged at an accelerated rate to simulate 9 years of service.

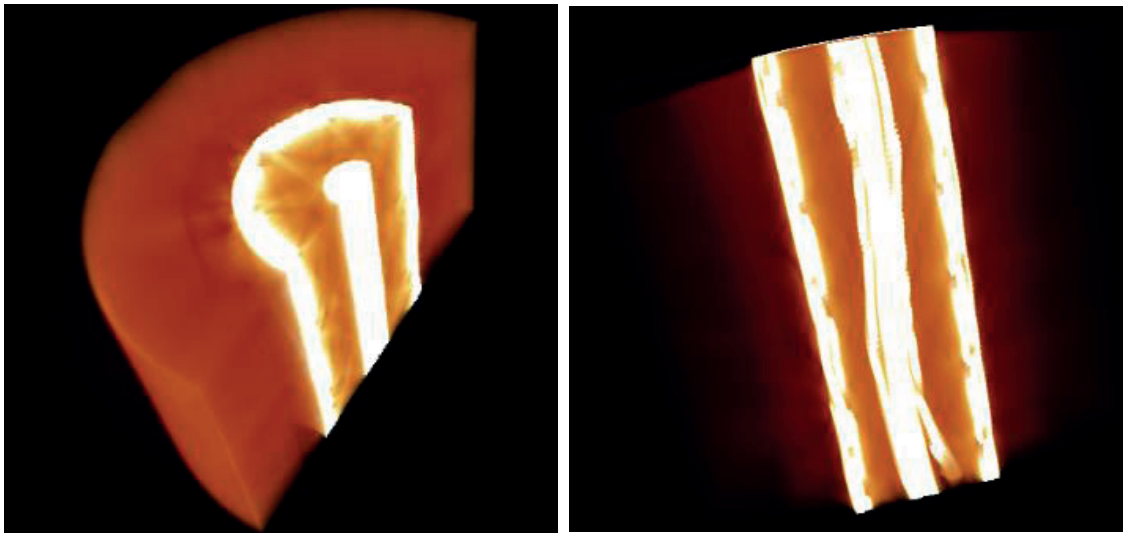

Figure 3.18: Transversal 3-dimensional x-ray CT images of the RG-58 cable comparing baseline sample and a segment aged at an accelerated rate to simulate 9 years of service.

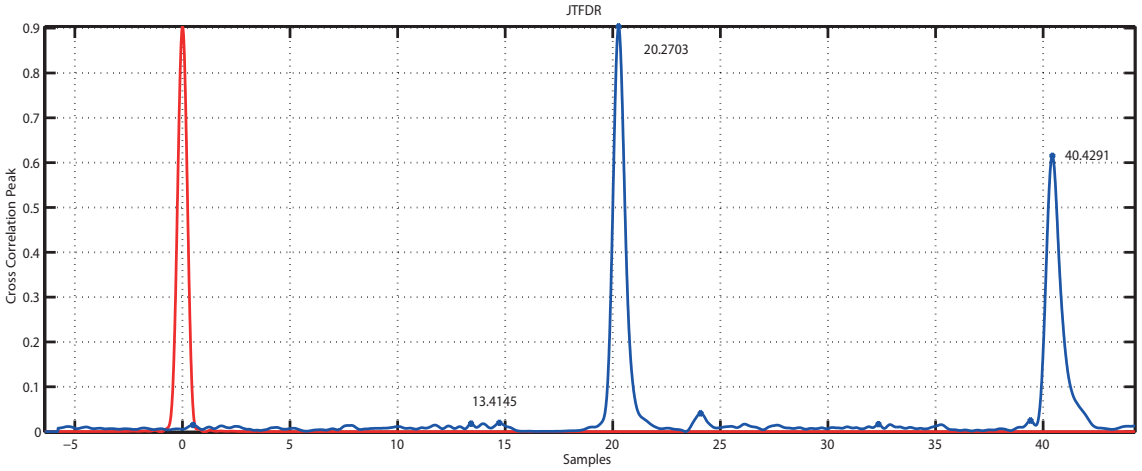

Figure 3.19: JTFDR Metric value for average of 20 acquisitions of baseline or unaged cable.

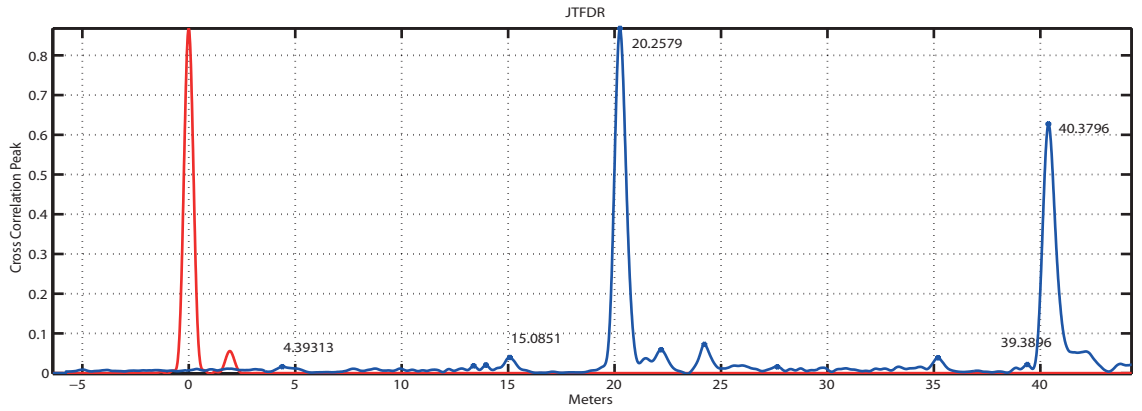

Figure 3.20: JTFDR Metric value for average of 20 acquisitions after 412 hours of accelerated aging simulating 9 years of service.

3.5 Measuring and Monitoring Multiple Faults

Analysis by JTFDR

Having shown individual graphs of the metric in Figures 3.19 and 3.20 for specific examples of accelerated aging a full compilation of the measured data for the course of 916 hours is presented in Figure 3.21. This presents the average of the 20 measurements taken at each aging interval. The trend was then calculated from the full set of aging data. A cubic interpolation is superimposed on the graph to show the general trend of simulated aging over time, and the metric typically increases over the duration of accelerated aging.

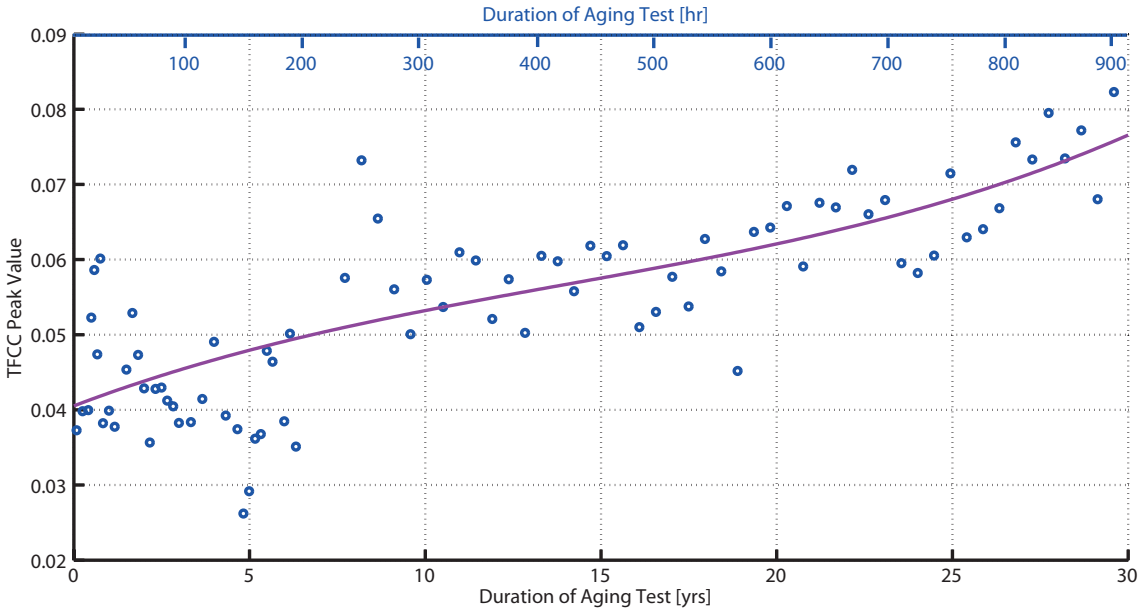

Figure 3.21: JTFDR Metric value for average of 20 acquisitions of an accelerated aging test simulating 30 years of cable life (916 hours of testing).

Having shown individual graphs of the metric in Figures 3.19 and 3.20 for specific examples of accelerated aging a full compilation of the measured data for the course of 916 hours is presented in 3.21. This presents the average of the 20 measurements taken at each aging interval. The trend was then calculated from the full set of aging data. A cubic interpolation is superimposed on the graph to show the general trend of simulated aging over time, and the metric typically increases over the duration of accelerated aging.

3.6 Conclusion

A new methodology is introduced for time-frequency domain reflectometry that helps further fault location and classification accuracy by introducing a phase discontinuity in the enveloping function. Accelerated aging is accomplished at lower temperatures that provide a better simulation of insulation damage than before. Results are confirmed by means of x-ray CT imaging. Insulation damage is apparent after aging and can be assessed and classified by fault impedance using time-frequency domain reflectometry.

CHAPTER 4

DESIGNING TIME-FREQUENCY DOMAIN REFLECTOMETRY SIGNAL FOR SURFACE WAVE PROPAGATION

In searching for a more universal method of prognostic remaining useful life indicators in high voltage cables, we sought a method that could couple to the cable in question (1) without requiring removal of the cable under test from a given system, (2) without damaging transmission cables, and (3) a method that is sensitive enough to enable assessment of impedance of the cable. Another key factor in order to provide a more versatile approach to HV testing is the injection method of the diagnostic signal. We will focus on the theory of surface wave injection of reflectometry signals (propagation along insulation surface waves induced by an antenna launcher) as a means of noninvasively injecting a diagnostic signal. Additionally, we present a method for optimizing a reflectometry signal in time and frequency domains and applications of these two principles for initial tests in transmission up to 15kV. These efforts will cumulatively add to the assessment of health of insulation materials in the real-world electric power systems.

4.1 IMPLEMENTATION OF TIME-FREQUENCY DOMAIN REFERENCE IN DISPERSIVE ENVIRONMENTS

In order to counter the dispersion properties of the antennae based surface wave signal injection methods, a secondary sinusoidal modulation is explored relative to the existing reference signal that can further tune the optimal reference to a given set of narrowband slices within a larger bandwidth.

4.2 Reference Signal for Surface Wave Propagation

Now we will consider the same simplified signal in (2.4) and add a sinusoidal modulation component to the signal. The signal becomes:

$$s(t) = \left(\frac{\alpha}{\pi}\right)^{1/4} e^{-\frac{\alpha t}{2} + j\frac{\beta t^2}{2} + jm \cdot sin\omega_m t + j\omega_0 t} \tag{4.1}$$

With the following derivation for the Wigner transform

$$W_s(t,\omega) = \frac{1}{2\pi}\left(\frac{\alpha}{\pi}\right)^{1/2} \int e^{-\frac{\alpha(t-\frac{1}{2}\tau)^2}{2} - j\frac{\beta(t-\frac{1}{2}\tau)^2}{2} - jm \cdot sin\omega_m(t-\frac{1}{2}\tau) - j\omega_0(t-\frac{1}{2}\tau)} \cdot e^{-\frac{\alpha(t+\frac{1}{2}\tau)^2}{2} + j\frac{\beta(t+\frac{1}{2}\tau)^2}{2} + jm \cdot sin\omega_m(t+\frac{1}{2}\tau) + j\omega_0(t+\frac{1}{2}\tau)} \cdot e^{j\tau\omega} \cdot d\tau \tag{4.2}$$

$$W_s(t,\omega) = \frac{1}{2\pi}\left(\frac{\alpha}{\pi}\right)^{1/2} \int_{-\infty}^{\infty} e^{-(\frac{1}{4}\alpha\tau^2 + jm \cdot (sin\omega_m(t-\frac{1}{2}\tau) - sin\omega_m(t+\frac{1}{2}\tau)) + j(\omega - \beta t - \omega_0)\tau + \alpha t^2)} d\tau \tag{4.3}$$

$$W_s(t,\omega) = \frac{1}{2\pi}\left(\frac{\alpha}{\pi}\right)^{1/2} \int_{-\infty}^{\infty} e^{-(\frac{1}{4}\alpha\tau^2 + j2 \cdot m \cdot sin(\omega_m t) \cdot cos(\frac{\tau}{2}) + j(\omega - \beta t - \omega_0)\tau + \alpha t^2)} d\tau \tag{4.4}$$

$$W_s(t,\omega) = \frac{1}{2\pi}\left(\frac{\alpha}{\pi}\right)^{1/2} e^{-\alpha t^2} \int_{-\infty}^{\infty} e^{-(\frac{1}{4}\alpha\tau^2 + j2 \cdot m \cdot sin(\omega_m t) \cdot cos(\frac{\tau}{2}) + j(\omega - \beta t - \omega_0)\tau)} d\tau \tag{4.5}$$

$$e^{j2m \cdot sin(\omega_m t) \cdot cos(\frac{\tau}{2})} = \sum_{n=-\infty}^{\infty} J_n(2m \cdot cos(\omega_m t)) e^{\frac{jn\omega_m \tau}{2}} \tag{4.6}$$

$$W_s(t,\omega) = \frac{1}{\pi} e^{-\alpha t^2} \sum_{n=-\infty}^{\infty} J_n(2m \cdot cos(\omega_m t)) e^{\frac{(\omega - \omega_0 - \beta t - \frac{n\omega_m}{2})^2}{\alpha}} \tag{4.7}$$

JTFDR computes the time-frequency cross correlation between an incident signal and the reflected signal through a propagating medium with the following equation:

$$C_{sr}(t) = \frac{1}{E_s E_r(t)} \int_{t'=t-T_s}^{t'=t+T_s} \int W_r(t',\omega) W_s(t'-t,\omega) d\omega dt' \tag{4.8}$$

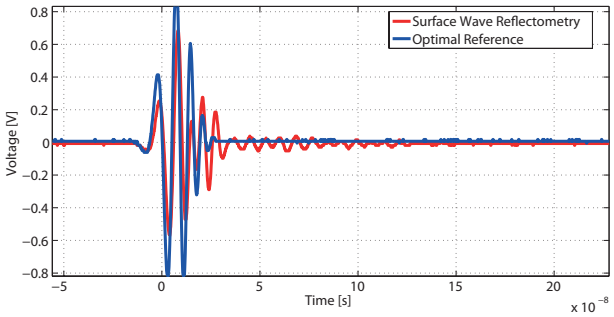

Figure 4.1: Optimal reference signal compared to reflected signal obtained by surface wave reflectometry

where $W_r(t,\omega)$ is the Wigner distribution of the reflected signal; $W_s(t,\omega)$ is the Wigner distribution of incident signal; and E_s and $E_r(t)$ are normalization factors.

$$C_{sr}(t) = \frac{1}{E_s E_r(t)} \int_{t'=t-T_s}^{t'=t+T_s} \int e^{-\alpha(t')^2} \sum_{n=-\infty}^{\infty} J_n(2m \cdot cos(\omega_m t')) e^{\frac{(\omega-\omega_0-\beta t' - \frac{n\omega_m}{2})^2}{\alpha}} \cdot e^{-\alpha(t'-t)^2} \sum_{n=-\infty}^{\infty} J_n(2m \cdot cos(\omega_m (t'-t))) e^{\frac{(\omega-\omega_0-\beta(t'-t)-\frac{n\omega_m}{2})^2}{\alpha}} \quad (4.9)$$

As a means of providing reflectometry and health assessment by a method that is both non-destructive and non-invasive, a conformal wave-guide based surface wave injection of a time- and frequency- localized diagnostic reference signal is proposed. Surface waves travel along the boundary between two different media, with the typical example, in reflectometry applications, of the boundary between conductor and insulation material. Sommerfeld explained surface wave propagation along an infinitely long cylindrical conductor of circular cross section embedded in an infinite homogenous dielectric material [71]. Elmore built on this foundational theory to propose power line communication by use of surface wave propagation [74]. The particular solution of that boundary value problem was a symmetric transverse magnetic (TM) wave traveling along the line wherein the electric field has only a longitudinal component, as shown in Figure 4.6.

The figure further illustrates basic surface wave propagation along the conductor/dielectric interface of an insulated unshielded power cable. The means of injecting this TM surface

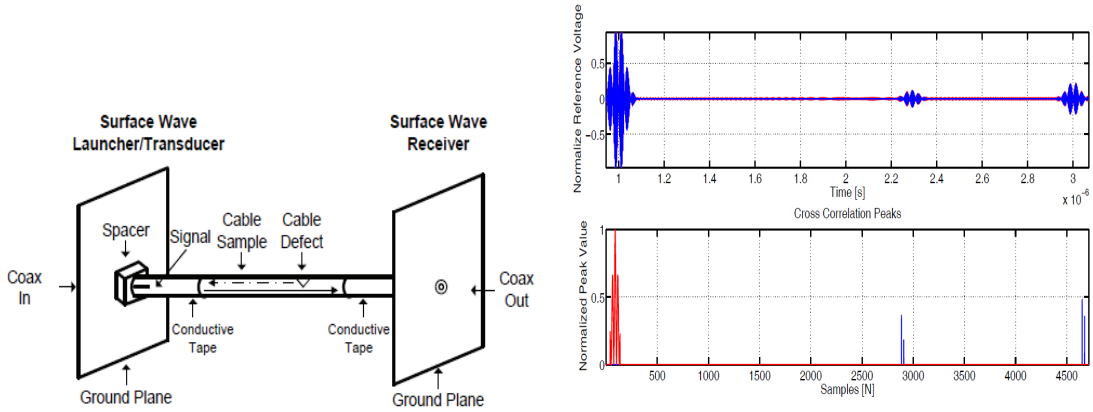

(a) (b)

Figure 4.2: (a) Experimental setup for Surface Wave Optimized and (b)Simulated defect on 10m segment of cable using the surface wave optimized reference shown in time domain (top)and by comparison using JTFDR (bottom).

wave along such an interface include: planar and cylindrical conductors with a thin layer of dielectric coating [75, 76], a large multi-wavelength horn shaped metal surface wave launcher exciting a desired wave mode propagation, or more recently small, conformal surface wave launchers [77, 78] The later methodology is used as described in Figure 4.1 and has demonstrated efficacy in open circuit fault detection of various power cables using Time Domain Reflectometry (TDR).

This work is then extended to the Time-Frequency Domain by use of a time-frequency localized optimal reference.

4.3 Implementation of Cable Health Assessment by Surface Wave Injection

Shown in Figure 4.2(a) is the system function diagram that describes the configuration and function of the experimental devices of the JTFDR wiring test bed for non-invasive surface wave injection methods. The signal is then reflected at the fault location, and travels back to the signal launcher/receiver. A prototype surface wave launcher/transducer pair (pictured in Figure 4.2(a)) was placed at each end of a 7 ft (2.1336m) cable sample and coupled to the cable using a concentrically wrapped length of conductive tape. This conductive tape was

connected to the signal connector of the coaxial input by a thin filament and separated from the input coaxial return by a polystyrene spacer. The coaxial return was in turn connected to the ground plane. Initial tests were performed to evaluate the utility of the surface wave signal in OEM unshielded cable samples (600V low voltage, LSTSGU-9, SIR insulated) and a shielded sample (15kV medium voltage, TR-XLPE insulated cable).

The first step of practical implementation of surface wave reflectometry for non-invasive diagnostic coupling is detection of an open end. Further work must be accomplished to fully characterize the frequency response and dispersion characteristics of the broadband monopole surface wave launcher before implementation of the methodology described previously, therefore, these tests utilize a JTFDR reference signal of a chirp signal in time-localized Gaussian envelope. The Gaussian chirp signal used in these tests has a center frequency at 350 MHz over a 100 MHz bandwidth for a 0.9 μs time duration.

Using the surface wave injection configuration of Figure 4.2(a), we tested the unshielded, low voltage and shielded, medium voltage cable samples using the JTFDR algorithm and the results are shown in 4.3(a) and 4.3(b) for 2 meter segments of each cable type. In each figure, the autocorrelation peak of the reference signal is represented by the peak with the most energy, which displays the start of the cable or reference point of the incident signal. A time-frequency cross-correlation of the reference and reflected signals is then shown by further corresponding peaks with the difference between the two peaks (reference and first reflection), scaled by the propagation velocity and signal lengths, providing an estimate of the length of the cable.

By use of the described metric for the LSTSGU-9 SIR cable an estimated cable length to open circuit fault was described as 1.9822 m, a 7.1 percent difference from the actual length of 2.1336 m. Similarly for the MV-90 TR-XPLE cable, a length to open circuit fault of 2.2489 m was estimated by optimized surface wave, a 5.4037 percent difference from the same length. These results show promise for a potential fault location algorithm and further tests in proposed work will explore the adjustments to JTFDR metrics while testing

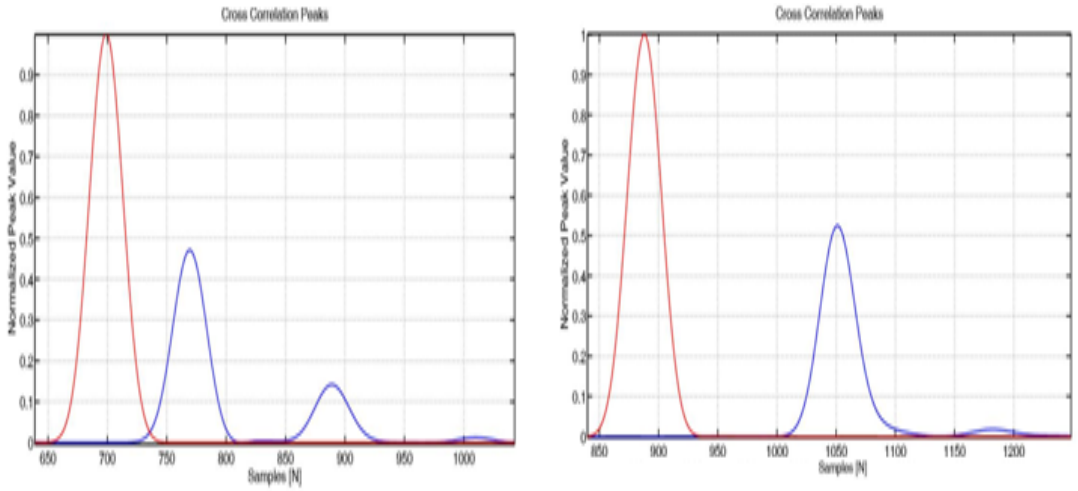

(a) (b)

Figure 4.3: Time-frequency cross correlation metric for open end measurement on 2 meter segment of (a) cable in low voltage unshielded case and (b) cable in medium voltage shielded case with stripped injection point.

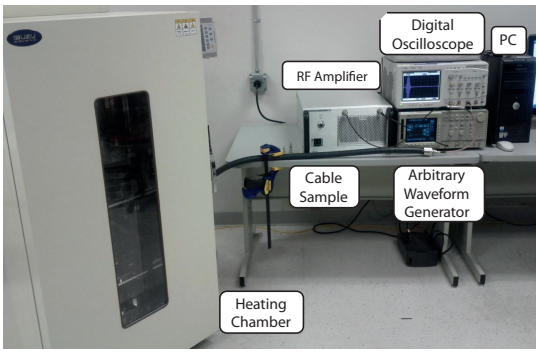

Figure 4.4: Generation and acquisition system for JTFDR.

longer lengths of cable.

4.4 Surface Wave Implementation

In practical implementation of surface wave tests through antenna, problems are presented in the form of dispersive media distorting the response of the frequency sweeping reference signal in either frequency or time-frequency domains. This is seen in the reflected signal of Fig. 2. However, we present an optimal reference signal and time-frequency cross correlation diagnostic and prognostic algorithm to allow for implementation of joint

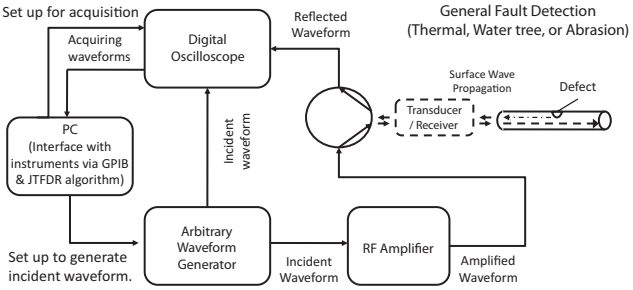

Figure 4.5: JTFDR system function diagram including surface wave launcher.

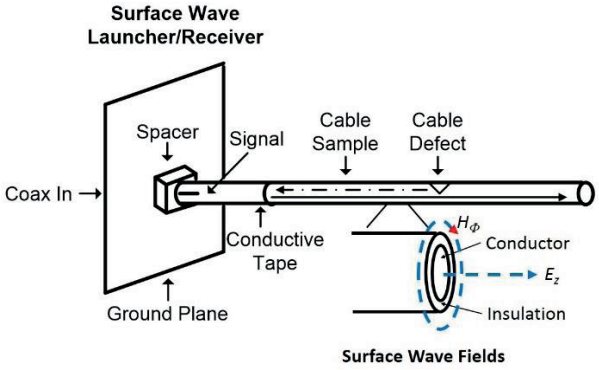

Figure 4.6: Experimental setup for surface wave optimized JTFDR and TM Surface wave fields in insulated power line.

time-frequency domain reflectometry (JTFDR). Research is focused on the application of JTFDR to 22.5 ft (6.86 m) segment of Southwire neutral cable (up to 600V, AWG 2/0) for initial verifications. Conditions of accelerated aging and thermal stress were simulated towards the ultimate development of present life appraisals along with fault location. The measurement algorithm allows for detection and distance estimation of multiple reflectometry peaks as induced by surface wave propagation of the optimal reference signal (those caused by initial insertion loss of connected impedance mismatch and subsequent reflections).

A “hotspot” of the cross-linked polyethylene (XLPE) cable was aged a total of 12 hours at 140C to simulate approximately 45 years of cable aging according to Arrhenius aging parameters. This aged segment was located from 8 to 10 ft (2.4 to 3 m) along the length of the cable. An undamaged segment of TR-XLPE insulated 15kV MV-90 designated

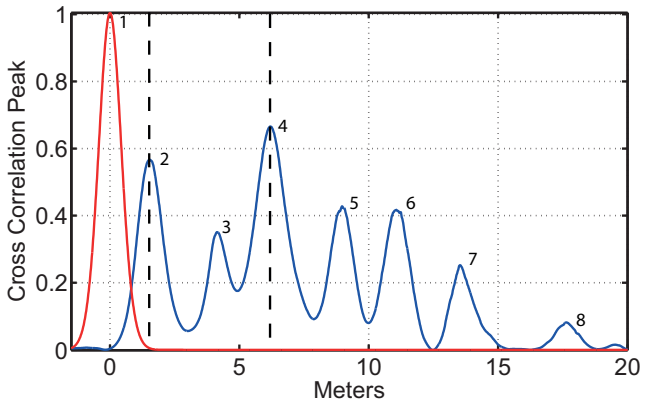

Figure 4.7: JTFDR algorithm updated to measure multiple reflection peaks and total reflected energy

Prysmian cable is also tested using the same metrics.

Shown in Figure 4.5 is the system function diagram that describes the configuration and function of the experimental devices of the wiring test bed for non-invasive surface wave injection methods. Each reflectometry reference signal is produced by an arbitrary waveform generator and sent to the surface wave launcher from the AWG via a 5 ft, 50Ω coaxial instrumentation cable. The Gaussian-chirp incident signal is designed based upon the input center frequency, bandwidth, and time duration with optional as described previously. This incident signal propagates (either via electrical connection or via surface wave) into the target cable via the RF amplifier in cases of longer cable lengths. The signal is then reflected at the fault location, and travels back to the signal launcher/receiver. The reflected signal is redirected to the digital oscilloscope. The computer program acquires both the incident and reflected signals from the oscilloscope and executes the time-frequency cross-correlation algorithm to detect, locate, and assess any defects on the cable.

4.5 Surface Wave Monitoring of Accelerated Thermal Aging Testing

To further adapt the JTFDR algorithm to circumstances presented by real-world implementation of surface wave propagation, multiple time-frequency cross correlation peaks are measured and peak maxima are determined corresponding to reflections of the injected

Table 4.1: Explanation of sample peaks data

Peak	Region	Dist. (m)	Explanation
1	Insertion	0.00	Start of Cable
2	Insertion	1.52	Insertion Loss
3	1st Reflection	4.13	End of Hot Spot
4	1st Reflection	6.50	End of Cable
5	2nd Reflection	8.97	Defect Reflection 1
6	2nd Reflection	11.10	Defect Reflection 2
7	2nd Reflection	13.50	Second Reflect, End
8	3rd Reflection	n/a	Additional Reflected

signal at areas of localized impedance change. An example is presented in Figure of the aforementioned Southwire low voltage neutral cable under 12 hours of accelerated aging conditions. An example interpretation of the time-frequency cross correlation reflectometry metric for fault location is provided here and summarized in Figure 4.7 and Table 1 where each local maximum is explained. Further figures provide a marker to indicate the local maxima and these locations are saved for the fault location algorithm.

The first peak highlighted in Figure 4.7 corresponds to the autocorrelation or reference point or start of the cable. The peak immediately following this typically corresponds to some initial reflection due to insertion loss of the optimal signal transducing antenna. Measurements between the start of cable and this peak are in the blind spot of reflectometry. In healthy cable, each subsequent peak corresponds to a reflection of the incident signal while a peak between expected reflection intervals produced by the open end may indicate damaged segments. The updated algorithm measures all local minimum and maximum peak values and records also the total energy of the reflected signal.

4.6 Discussion and Summary

With the previously outlined thermal stress procedures, data was taken using the optimal reference signal with center frequency 120MHz with frequency bandwidth and time duration at 100 MHz and 30 nanoseconds respectively. After cooling the cable from ther-

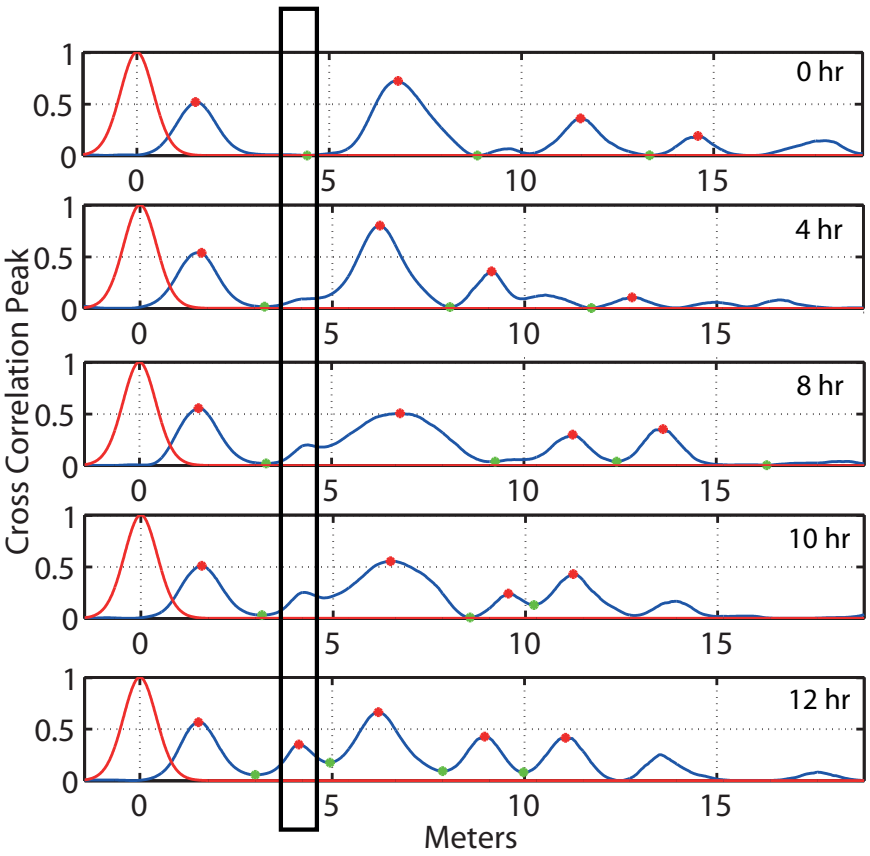

Figure 4.8: The JTFDR cross-correlation peaks (blue) are shown here with the autocorrelation (red) and highlighted segment illustrating the peak growth with increased thermal stress over the course of 12 hours of accelerated aging.

mal stress, measurements of raw data and computed time-frequency cross correlation were taken and saved. From the multipeak JTFDR health assessment algorithm, distances of peaks were determined corresponding to initial reflection from signal launcher, first and subsequent reflections from the end of the cable, and potential heating defect between the initial start of cable reflection and the end of cable reflection.

While Figure 4.7 showed the specific peaks for one set of measurements Figure 4.8 shows the subsequent growth of defective region or hot spot peak over the course of thermal stress corresponds to a point at approximately 3m. From experimental results, the fault

growth is found at an average distance of 3.812 m. One possible source of error is in a difference of the dielectric constant of the cable from manufacture standard affecting the propagation velocity used for reflectometry calculations. This showcases the ability of the JTFDR method to work with surface wave injection and measure both fault location and severity in real-time, non-invasively under noise conditions as seen in Figure 4.5.

4.7 Conclusion

The results show that thermal stresses and aging can be monitored non-invasively with a prototype implementation of guided surface wave propagation that does not require physical connection to the system. These methods are first applied to lower voltage unshielded neutral cable and then extended to cable supporting voltage up to 15 kV. Problems that have been encountered with this approach such as a higher insertion loss from the new signal propagation method have been countered with changes to the JTFDR algorithm to allow for multiple peak detection and estimation of total reflected energy. These strengthen the overall efficacy of the methodology and provide a new path to a condition based age monitoring and fault locating diagnostic system.

CHAPTER 5

HEALTH MONITORING OF ROTORCRAFT DRIVETRAIN BY MUTUAL INFORMATION

5.1 INTRODUCTION

Experimental Setup

The CBM center at The University of South Carolina has an AH-64 Helicopter tail rotor drivetrain test stand for on-site data collection and analysis [1]. The test stand includes an AC input motor (Fig. 5.1(a)) rated at 400 horsepower to provide input drive to the configuration, a multi-shaft drive train supported by hanger bearings, flex couplings at shaft joining points, two gearboxes, and an absorption motor of matching rating to simulate the torque loads that would be applied by the tail rotor blades. The test stand, with picture provided in Figure 5.1(b), was used to collect data to be used in conjunction with historic helicopter vibration data to develop the baseline of operation for the systems under test. The signals are collected during the operational run of the apparatus included vibration data measured by accelerometers, temperature measured via thermocouples, and speed and torque measurements. The measurement devices were placed at the forward and aft hanger bearings and both gearboxes. This paper focuses on the application of time-frequency techniques to the forward and aft hanger bearing vibration signals denoted as S_1 and S_2 in Figures 5.1(a) and (b). The physical separation of between accelerometers (which will further be referred to more generally as sensors) on the bearings is 3.43 m.

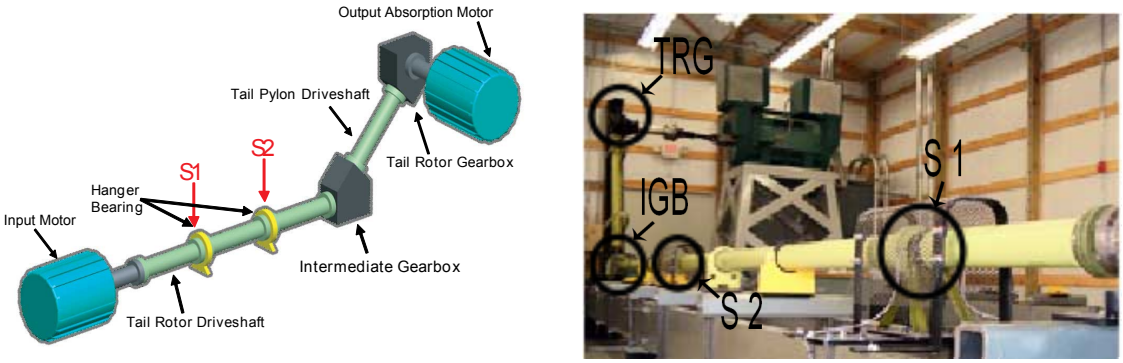

(a) (b)

Figure 5.1: Schematic representation of AH-64 helicopter tail rotor drivetrain test stand (a) and actual test stand (b) with labeled components for comparison.

Data Acquisition

The data acquisition software collects data from the hanger bearings once every two minutes during the course of the thirty minute baseline runs, with the exception of two additional collection periods at the start of the run, a total of 17 measurements. An experimental run consists of an intermediate speed ramp from 0 to 600 RPM followed by a ramp from 600 to 4863 RPM. The measurements for baseline characterization were then taken during operation of the test stand at a constant rotational speed of 4863 RPM from the prime mover with a simulation of output torque at 111 ft-lbs from the secondary. A summary of test conditions is given in Table 5.1 given a few conventions. Rotational speed is the speed of the input shafts and hanger bearings. Output torque is given by the torque at the output of the tail rotor gearbox simulating rotor operation while the torque applied to the input shafts and hanger bearings is equal to 32.35 ft-lbs.

Table 5.1: Loading profile for a 30 minute baseline test run

Rotational Speed (RPM)	Output Torque (ft-lb)	Input Torque (ft-lb)	Duration (min)
0-600	0	0	7.5
4863	111	32.35	30
600-0	0	0	7.5

Data collection yielded 65,536 point at a sampling rate of 48 kS/s per scheduled sampling period, which results in a data collection time of roughly 1.31 sec per acquisition. For each run, data was acquired 17 times on these 1.31 sec intervals: twice at the beginning and then once every two minutes until the end of the run. With individual data files containing 65,536 samples each, acquisition results in over one million data points per set, which is too intensive for many processors to handle during time-frequency analysis. In order to resolve this computational issue and decrease computation time, each data set under test was divided into 17 experimental frames to correspond to each time the sensor was activated to collect data. Each of the 17 experiments was then divided into 16 windows comprised of 4096 points each. Within these subdivided windows, spectrogram measurements were made on both S_1 and S_2 while the mutual information measure was applied to 4096 point segments of S_1 and S_2.

Additional windows can determined by an overlap percentage which layers additional 4096 point windows within the main 16 in a given experimental frame at intervals of 4096 multiplied by the overlap percentage in order to create additional effective mutual information measurements from the given data. An overlap of 33 percent was determined to provide adequate clustering and enhance the probability density for implementation of predictive confidence levels.

This overlap selection helps eliminate data outliers and improve the visualization of the clustering when applying the time-frequency mutual information described in Section 5.2 to multiple data points. Therefore the total number of mutual information measure points for the given data is equal to the number of experimental frames (17) multiplied by the number of window signal subsets (16) and the inverse of the fractional overlap percentage (3), for a total of 816 mutual points or 272 mutual points when neglecting overlap components. The data format of the time series is also provided in [26].

The configuration of the test stand uses balanced drive-shafts aligned in a straight assembly as a baseline for normal operations. After performing test runs in the baseline

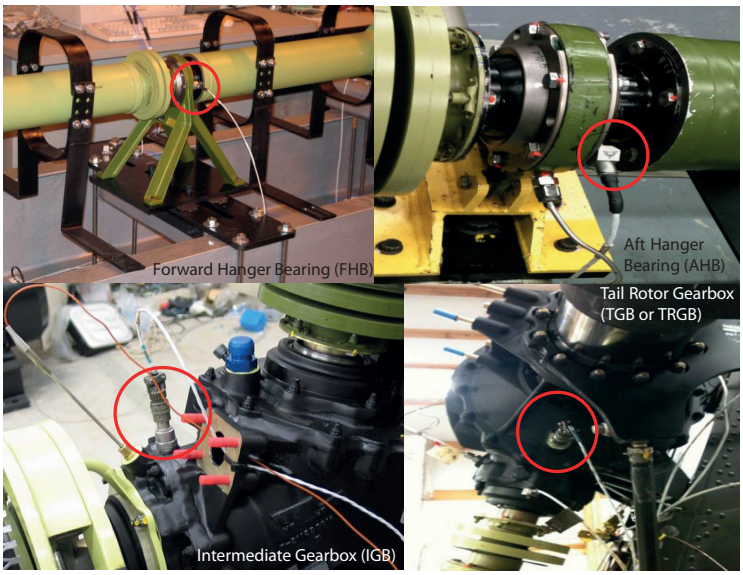

Figure 5.2: Primary accelerometer sensor locations on the tail rotor drivetrain test stand on a per component basis for hanger bearings (FHB and AHB) and intermediate and tail rotor gearboxes (IGB and TGB).

condition, intentionally faulted configurations are tested to expand the baselines to include combinations of misaligned and unbalanced shafts. The goal of the time-frequency analysis is to establish metrics for the baseline conditions using the original data set and produce a set of metrics to diagnose each of unbalanced and misaligned conditions. The data presented for analysis included five sets of thirty minute runs of the apparatus each taken with different alignment and balancing conditions. Table 5.2 displays these conditions and their designations.

The primary physical fault conditions characterized experimentally are bearing unbalance and shaft misalignment. While these conditions will be described more thoroughly in Section 5.4, an overview of these settings helps in gaining a familiarity with the experimental set up. The nomenclature of the baseline sets is dictated by numbered segments of the drive-train. Each segment of concern in experimentation is designated by a number (1 through 5) and coupled by flex couplings at the bearings locations to hanger bearings. Unbalance is related to drive shafts which exhibit geometrical or mass centerlines that do not coincide with axes of shaft rotation (UB/A and UB/MA cases). These will be referred to as

the unbalanced-aligned (UB/A) and unbalanced-misaligned (UB/MA) cases respectively. Misalignment (MA/B, UB/A and MA/UB cases) in the test configuration is characterized by a change in bearing and shaft placement that moves the number 3, 4, and 5 shafts from straight alignment to produce an angle of 1.3 degrees. Either a 3-5 unbalance (unbalance of three consecutive drive shafts) or a 4-5 unbalance (unbalance of only two drive shafts) differentiates two experimental settings. The aforementioned settings will be referred to as the misaligned-balanced (MA/B) and unbalanced-misaligned (UB/MA) 3-5 and 4-5 cases. These settings produce additional wear on drive-train components while also presenting additional transients in harmonics that can be measured for health classification purposes. For the purposes of this paper we will simply refer to these cases as baseline (A/B), misaligned (MA/B), unbalanced (UB/A), and misaligned-unbalanced (MA/UB) as shown in the nomenclature of Table 5.2. Instances of ambiguity between the misaligned-unbalanced cases will be specified as 3-5 misaligned or 4-5 misaligned.

Table 5.2: Tail Rotor Driveshaft Experimental Settings

Shaft Status	Balanced	Unbalanced
Aligned	A/B	UB/A
Misaligned	MA/B	MA/UB 3-5, 4-5

Unbalance vibrations are generated when geometrical centerline or mass centerline of a shaft do not coincide with the rotational axis of the shaft, for example in cases of bearing

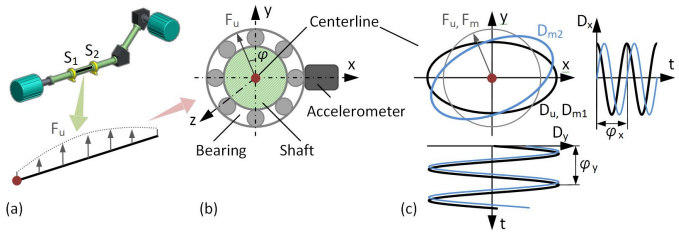

Figure 5.3: Unbalance force distribution over the shaft supported at the S_1 and S_2 accelerometers locations (a) cross-section of a bearing and the shaft at the S_1 accelerometer location (b) shaft centerline orbits at the S_1 and S_2 accelerometer locations, and (c) displacement or vibration components in the x and y axis directions (D_u, D_{m1} orbits when $\varphi_y - \varphi_x = 90^\circ$, D_{m1} when $\varphi_y - \varphi_x = 120^\circ$)

looseness or due to manufacturing imperfections. This inconsistency between rotational axis and geometrical or mass centerline creates a radial bow force F_u at a fixed relative phase angle, φ, which varies in magnitude along the length of the shaft as shown in Figure 5.3-(b). The unbalance condition creates harmonically varying vibrations, D, on a hanger bearing housing, which are registered by dedicated accelerometers. These varying vibrations consist of x and y axis radial vibrations, z axis axial vibrations, and torsional vibrations of a shaft in a bearing (Figure 5.3-(b)) as well as additional vibration signal contributions coming from coupled bearings, gearboxes, power units, airframe, and other components. Each hanger bearing on a helicopter system has only one dedicated accelerometer in current settings, which can pick only lateral x axis component of the vibrations (Figure 5.3-(c)) of the form:

$$D_x = A_x \cdot \cos(\omega t + \psi_x) \tag{5.1}$$

$$D_y = A_y \cdot \sin(\omega t + \psi_y) \tag{5.2}$$

where $D_{x,y}$ and $A_{x,y}$ are displacements and amplitude of displacements in x and y axis directions, ω - angular velocity, and $\psi_{x,y}$ - phase angles.

Vibrations caused by unbalance will be in-phase on both bearings accelerometers S_1 and S_2 when $(\varphi_y - \varphi_x = 0)$, and will vary only in magnitude depending on the magnitude of unbalance, F_u. The drive shaft supported by the hanger bearings at sensor locations S_1 and S_2 is not a uniform shaft but rather a sectionalized shaft as previously described. Therefore, misalignment cannot typically be avoided. It should be noted that as shown in Table 5.1 the experimental data is gathered under conditions of constant or near constant torque load and speed.

Misalignment in our case is considered as an angular misalignment when the shaft centerlines of the two shafts meet at angle with each other. This, on the contrary to unbalance, causes axial preloads on the shaft in the z axis direction, and can be decomposed to x signal component based on angle of misalignment $F_x = F_z sin(\alpha_m)$. This force will have the greatest impact on the bearing closest to the shafts' coupling point, and will have a phase

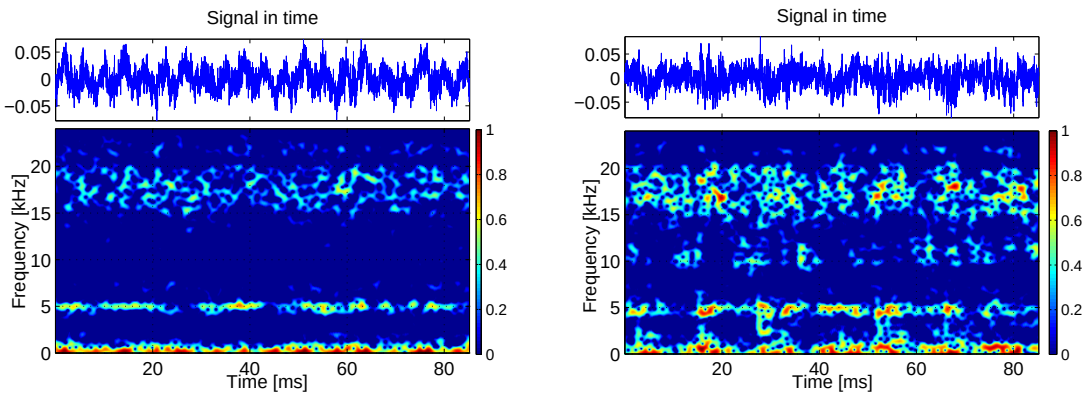

(a) (b)

Figure 5.4: Spectrogram of S_1 for (a) baseline (B/A), and (b) misaligned-unbalanced (MA/UB 3-5).

difference in reference to force registered at a further located sensor $(\varphi_y - \varphi_x \neq 0)$ (Figure 5.3-(c)) because of finite stiffness and dampening in the system.

In industrial vibration monitoring one would use shaft diagnosis techniques such as shaft centerline orbit monitoring, which requires two x and y sensors at a single location, and a skilled human operator, which make such technique inapplicable in our case and justifies the need for an advanced diagnostic measure. Mutual information measure takes advantage of two accelerometer signals located at different locations, simultaneously quantifying all frequency and phase components of the mechanical vibrations signals.

Low Grease Case Study in Tail Rotor Gearbox

The first case study to be discussed using the AH-64 TRDT teststand is a grease drought experiment for the tail rotor gearbox (TGB). The TGB is a grease-lubricated right-angle transmission with a speed reduction ration of 2.591:1 dictating the component output frequencies. This speed corresponds to a gear mesh frequency of 1334 Hz with subsequent harmonics at approximately 2668, 4000, and 5336 Hz being key frequencies in vibration analysis and fault diagnostics. In actual rotorcraft, the output seal of this gearbox is often problematic due to a combination of factors: (1) inoperability of maintenance without first

(a) (b)

Figure 5.5: Images of the inside of the intermediate gearbox taken by a borescope (a) in a healthy gearbox and (b) after a grease starvation experiment provides significant damage to the gear teeth.

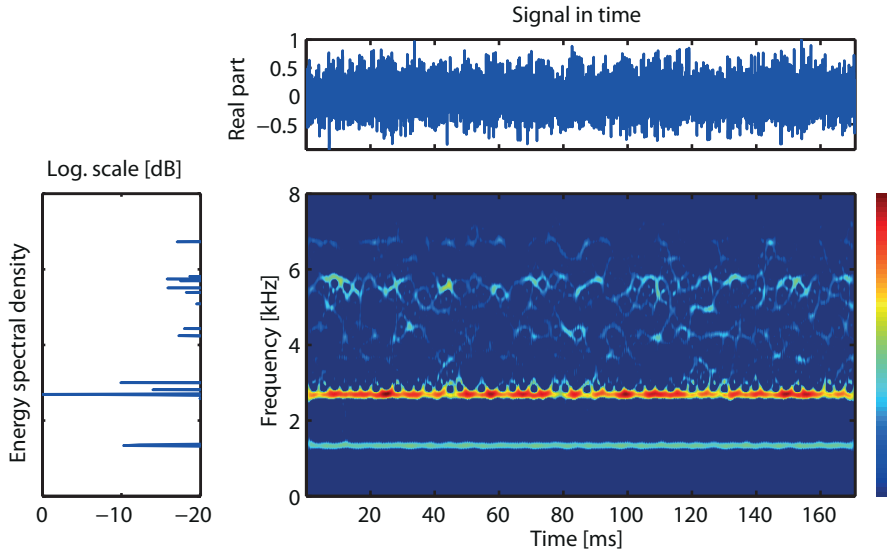

Figure 5.6: Time-frequency representation with Zhao-Atlas-Marks kernel showing the time-varying spectrum of a vibration signature near the end of life (4 days before failure) in a Tail Rotor Gearbox case study.

removing the component from the tail of the AH-64, (2) subsequent lack of field servicing capability, and (3) a difficulty in assessing the amount of grease in the static mast proceeding the output seal in general to assess the need for repair. This fault accounted for half of all gearbox removals in 2006 and provided a situation where a faulted gearbox was both difficult to detect and often preemptively removed and torn down with or without complete assurance of initial causality. At the TRDT test stand, a worst case scenario was replicated

for this TGB fault by inducing a leak in the output seal and allowing grease to drain from the static mast. This test gearbox was then operated for 500 hours without additional grease servicing. Much of the grease volume from initial servicing had been ejected by 150 hours and the grease amount was considered under-serviced by 260 hours of running operation. By 300 hours of testing, tooth wear was evident in the single spiral bevel gear set as shown compared in Figure 5.5 with a healthy set of gear teeth. Vibration data was gathered for the last week of operating test runs preceding a failure at 487 hours in which a gear tooth broke and normal operation of the gearbox was halted. Figure 5.6 shows the time-frequency representation by Zhao-Atlas-Marks kernel for the first day of this week of test runs. Further results of this vibration analysis case study will be presented in 5.3 with additional metrics derived to assess time-frequencies transients.

5.2 Theory of Mutual Information for Condition Based Maintenance

Cross Time-Frequency Distribution

The metric $H_\alpha(C_s)$ defined in (1.26) measures the number of signal elements of $s(t)$ over the time and frequency planes. The Rényi information measure is a meaningful measure of time-frequency distribution, but it is only defined for a single realization of signal, e.g. self-information. If we have a pair of signals closely related, how can we define or quantify the interactions in terms of information? We will investigate a generalization of the time-frequency information measure by introducing the mutual time-frequency information.

In order to analyze the information of two closely spaced components, the classical mutual information of two random processes is extended to two time-frequency distribution functions. Let us consider the classical definition of the mutual information that might be extended to the measure of mutual information of the time-frequency distributions. The joint entropy $H(X,Y)$ of a pair of continuous random variables (X,Y) with a joint proba-

bility density function $p(x,y)$ is defined as:

$$H(X,Y) = -\int\int p(x,y)\log_2 p(x,y)dxdy \tag{5.3}$$

By chain rule,

$$H(X,Y) = H(X) + H(Y|X) \tag{5.4}$$

where $H(Y|X)$ is the conditional entropy. Under the same conditions, the mutual information $I(X;Y)$ is the relative entropy between the joint distribution $p(x,y)$ and the product distribution of the individual marginal distribution $p(x)$ and $p(y)$ as follows:

$$I(X;Y) = \int\int p(x,y)\log_2 \frac{p(x,y)}{p(x)\cdot p(y)} \tag{5.5}$$

The relation of the mutual information $I(X;Y)$ and joint entropy $H(X,Y)$ is defined as follows:

$$\begin{aligned} I(X;Y) &= H(X) - H(X|Y) \\ &= H(Y) - H(Y|X) \\ &= H(X) + H(Y) - H(X,Y) \end{aligned} \tag{5.6}$$

Thus, it is necessary for us to define cross time-frequency distribution $J_{s_1s_2}(t,\omega;\phi)$ of the signal pairs S_1 and S_2 [46].

$$\begin{aligned} J_{s_1s_2}(t,\omega;\phi) &= \frac{1}{4\pi^2}\int\int\int s_1(u+\frac{\tau}{2})s_2^*(u-\frac{\tau}{2})\phi(\theta,\tau) \\ &* \quad e^{-j\theta t - j\tau\omega + j\theta u}d\theta d\tau du \end{aligned} \tag{5.7}$$

The kernel $\phi(\theta,\tau)$ is equivalent to the kernel given in Cohen's class in (1.24) and the cross time-frequency distribution satisfies time and frequency marginal property under the same constraints given in Cohen's class. Consider a joint information of time-frequency distribution $H_\alpha(J_{s_1s_2})$ in terms of cross time-frequency distribution $J_{s_1s_2}(t,\omega;\phi)$ as follows:

$$\begin{aligned} H(S_1,S_2) &= H_\alpha(J_{s_1s_2}) = \\ &= -\frac{1}{1-\alpha}\log_2 \frac{\int\int J_{s_1s_2}^\alpha(t,\omega)dtd\omega}{\int\int J_{s_1s_2}(t,\omega)dtd\omega} \end{aligned} \tag{5.8}$$

Time-Frequency Mutual Information Measure

However, one must be careful in defining the information measure of the cross time-frequency distribution which is a complex number. In addition, normalization of the distribution is important for a proper bound of the information measure. Therefore, instead of direct application of the generalized Rényi information, consider the normalized cross time-frequency distribution $\overline{J}_{s_1 s_2}(t,\omega)$ as follows:

$$\begin{aligned}
\overline{J}_{s_1 s_2}(t,\omega) &= \frac{J_{s_1 s_2}(t,\omega)}{\sqrt{C_{s_1}(t,\omega)\cdot C_{s_2}(t,\omega)}} \\
&= \frac{R_{s_1 s_2}(t,\omega)}{\sqrt{C_{s_1}(t,\omega)\cdot C_{s_2}(t,\omega)}} \\
&+ j\frac{Q_{s_1 s_2}(t,\omega)}{\sqrt{C_{s_1}(t,\omega)\cdot C_{s_2}(t,\omega)}} \\
&= \overline{R}_{s_1 s_2}(t,\omega) + j\overline{Q}_{s_1 s_2}(t,\omega) \qquad (5.9)
\end{aligned}$$

We can define the time-frequency mutual information measure of in-phase $I^R_\alpha(S_1;S_2) = -H_\alpha(\overline{R}_{s_1 s_2})$ and quadrature $I^Q_\alpha(S_1;S_2) = -H_\alpha(\overline{Q}_{s_1 s_2})$ as follows:

$$\begin{aligned}
I^R_\alpha(S_1;S_2) &= \frac{1}{1-\alpha}\log_2 \int\int R^\alpha_{s_1 s_2}(t,\omega)dtd\omega \\
&- \frac{1}{2}\cdot\{H_\alpha(C_{s_1}) + H_\alpha(C_{s_2})\} \qquad (5.10) \\
I^Q_\alpha(S_1;S_2) &= \frac{1}{1-\alpha}\log_2 \int\int Q^\alpha_{s_1 s_2}(t,\omega)dtd\omega \\
&- \frac{1}{2}\cdot\{H_\alpha(C_{s_1}) + H_\alpha(C_{s_2})\} \qquad (5.11)
\end{aligned}$$

Then, the mutual information measure $I_\alpha(S_1;S_2)$ of S_1 *and* S_2 is defined in terms of in-phase time-frequency mutual information $I^R_\alpha(S_1;S_2)$ and quadrature time-frequency mutual

information $I_\alpha^Q(S_1;S_2)$ as follows:

$$\begin{aligned} I_\alpha(S_1;S_2) &= I_\alpha^R(S_1;S_2)+I_\alpha^Q(S_1;S_2) \\ &= -H_\alpha(\overline{R}_{s_1s_2})-H_\alpha(\overline{Q}_{s_1s_2}) \\ &= H_\alpha(C_{s_1})-H_\alpha(C_{s_1}|C_{s_2}) \\ &= H_\alpha(C_{s_2})-\underbrace{(H_\alpha(C_{s_1},C_{s_2})-H_\alpha(C_{s_1}))}_{H_\alpha(C_{s_2}|C_{s_1})} \\ &= H_\alpha(C_{s_2})-H_\alpha(C_{s_2}|C_{s_1}) \end{aligned} \tag{5.12}$$

Therefore, the mutual time-frequency information $I_\alpha(C_{s_1};C_{s_2})$ is the sum of individual time-frequency information $H_\alpha(C_{s_1})$, $H_\alpha(C_{s_2})$ and joint information $H_\alpha(C_{s_1},C_{s_2})$. For example, if $s_1(t)=s_2(t)$, then $C_{s_1}=C_{s_2}$ and $Q_{s_1s_2}=0$ such that

$$I_\alpha(C_{s_1};C_{s_2})=I_\alpha(C_{s_2};C_{s_2})=H_\alpha(C_{s_1}) \quad \text{or} \quad H_\alpha(C_{s_2}) \tag{5.13}$$

Based on the mutual time-frequency information measure, we investigate the efficacy of the proposed technique with real-world data sets. The experimental setup and data descriptions are provided in Section 5.1.

5.3 Analysis of Hanger Bearing Vibration Signals in Tail Rotor Gearbox Case Study

Frequencies of Interest and Corresponding Rotating Components

A more advanced analysis was performed on raw vibration data using the Zhao-Atlas-Marks kernel for joint time-frequency distribution. Much like the commonly used spectrogram, this distribution shows time domain and frequency domain content of a signal simultaneously using the same fundamental principles as a short-time Fourier transform. A repeated computation of the transform was performed over several short time intervals creating a distribution of time and frequency content, thus providing a higher sensitivity to

Table 5.3: Rotating Frequencies of TRDT Components Provided by AED

Component Source	Harmonic Number	Frequency Type	Frequency (Hz)	Frequency (RPM)
Hanger Bearings	1	CFF	31.95	1917
Hanger Bearings	2	CFF	63.90	3834
Driveshaft	1	SO	81.06	4863
Hanger Bearings	3	CFF	95.85	5751
Hanger Bearings	4	CFF	127.80	7668
Driveshaft	2	SO	162.11	9727
Hanger Bearings	1	BSF	182.89	10974
Driveshaft	3	SO	243.17	14590
Hanger Bearings	1	BPFO	287.55	17253
Driveshaft	4	SO	324.23	19454
Hanger Bearings	2	BSF	365.79	21947
Hanger Bearings	1	BPFI	441.96	26518
Hanger Bearings	3	BSF	548.68	32921
Hanger Bearings	2	BPFO	575.10	34506
Hanger Bearings	4	BSF	731.57	43894
Hanger Bearings	3	BPFO	862.65	51759
Hanger Bearings	2	BPFI	883.92	53035
Hanger Bearings	4	BPFO	1150.19	69012
Hanger Bearings	3	BPFI	1325.89	79553
Hanger Bearings	4	BPFI	1767.85	106071

and resolution in the change of signal components over time. These results confirm the oscillating behavior of signal characteristics observed in the gear mesh frequency plots. The first surveys taken on the days before the failure show a reduced signal noise in the 3 to 6 kHz range when compared to samples taken later in the day. On the day of gearbox failure, higher-order gear mesh harmonics become prominent, and the noise band is reduced.

In the predictive maintenance practices of CBM, metrics similar to the simpler total harmonic distortion (THD) or root mean squared (RMS) classical methods are used as diagnostics. These provide comparisons of a signal harmonic component (such as the fundamental) to other harmonics in weighted algorithms. These metrics provide good indications of vibration characteristics under the condition that the frequency components under test are stationary, or remain unchanged with the progression of time.

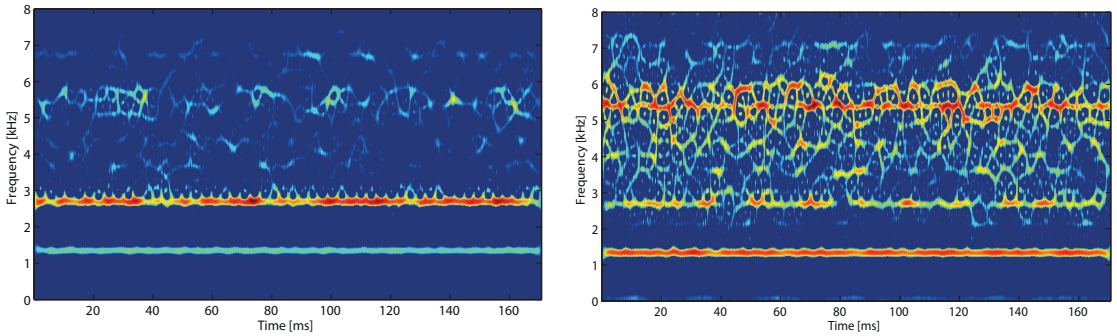

(a) (b)

Figure 5.7: Time-frequency representation with Zhao-Atlas-Marks kernel showing the time-varying spectrum of a vibration signature near the end of life (2 days before failure) in a Tail Rotor Gearbox case study. Data acquisition surveys are taken at (a) start of run and (b) under torque load from absorption motor

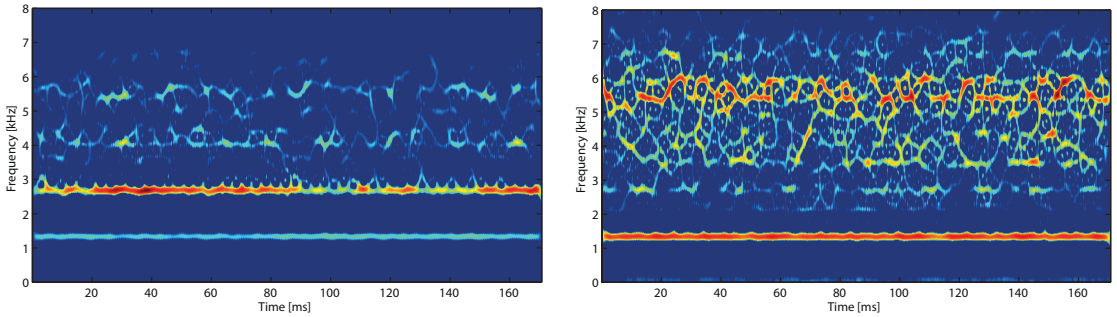

(a) (b)

Figure 5.8: Time-frequency representation with Zhao-Atlas-Marks kernel showing the time-varying spectrum of a vibration signature near the end of life (1 day before failure) in a Tail Rotor Gearbox case study. Data acquisition surveys are taken at (a) start of run and (b) under torque load from absorption motor

Unfortunately, this classical approach inherently assumes the disturbance is of a periodic nature. In fact, not all real life disturbance events result in periodic waveforms and transient frequency variations are common in the event of faulted components. Often events such as damage cause disturbances that can best be characterized as transient in nature. In such cases it is necessary to study the time-varying frequency components of a disturbance. This can be accomplished with time-frequency analysis.

The motivation to use time-frequency analysis is to have the ability to represent and analyze non-stationary signals whose spectral characteristics change in time. One approach

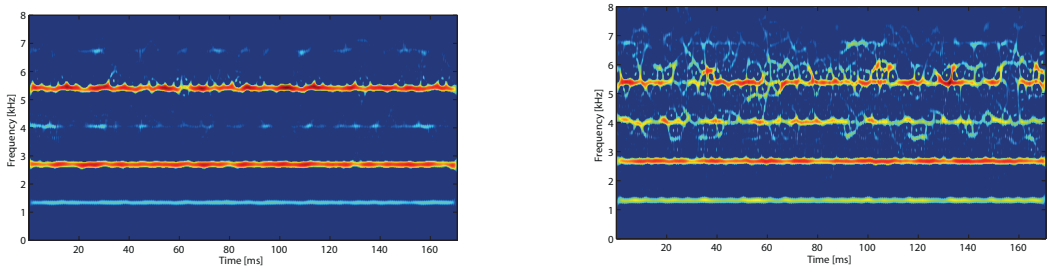

(a) (b)

Figure 5.9: Time-frequency representation with Zhao-Atlas-Marks kernel showing the time-varying spectrum of a vibration signature near the end of life (day of failure) in a Tail Rotor Gearbox case study. Data acquisition surveys are taken at (a) start of run and (b) under torque load from absorption motor

to time-frequency analysis is to take the time-frequency distribution of a signal.

The problem with WV distribution is that it introduces artifacts in a multicomponent signal between existing components (on auto terms) at non-linear spacings (cross-frequencies). This artifact can be reduced with CW, RID, and ZAM distributions, shown in Figure 5.10(a)-(f). The ZAM kernel was selected for this project for its its general capability to represent a fair tradeoff in time and frequency resolution. The window for this function is selected based on the number of frequency bins (N = 1024) with the Hamming window being selected in both time and frequency smoothing. The time and frequency window lengths are given as N/10 (or 103) and N/4 (or 255) respectively with rounding to the nearest odd number. Looking at the time-frequency distributions of the two signals, we can see that the first signal (advanced state) has four frequency bands while the second signal (damaged state) has two frequency components with increased energy in the second harmonics and decreased energy in the first harmonics. However, the second signal seems to have more transient variation among the frequency bands. We will search for a way to define this transient variation. The metric $H_\alpha(C_s)$ defined in (1.26) measures the number of signal elements of $s(t)$ over the time and frequency planes.

Figure 7 is a metric derived from the Rényi information of the time-frequency distribution. In Figure 7(a), the Rényi information or entropy of the of Wigner-Ville kernel is

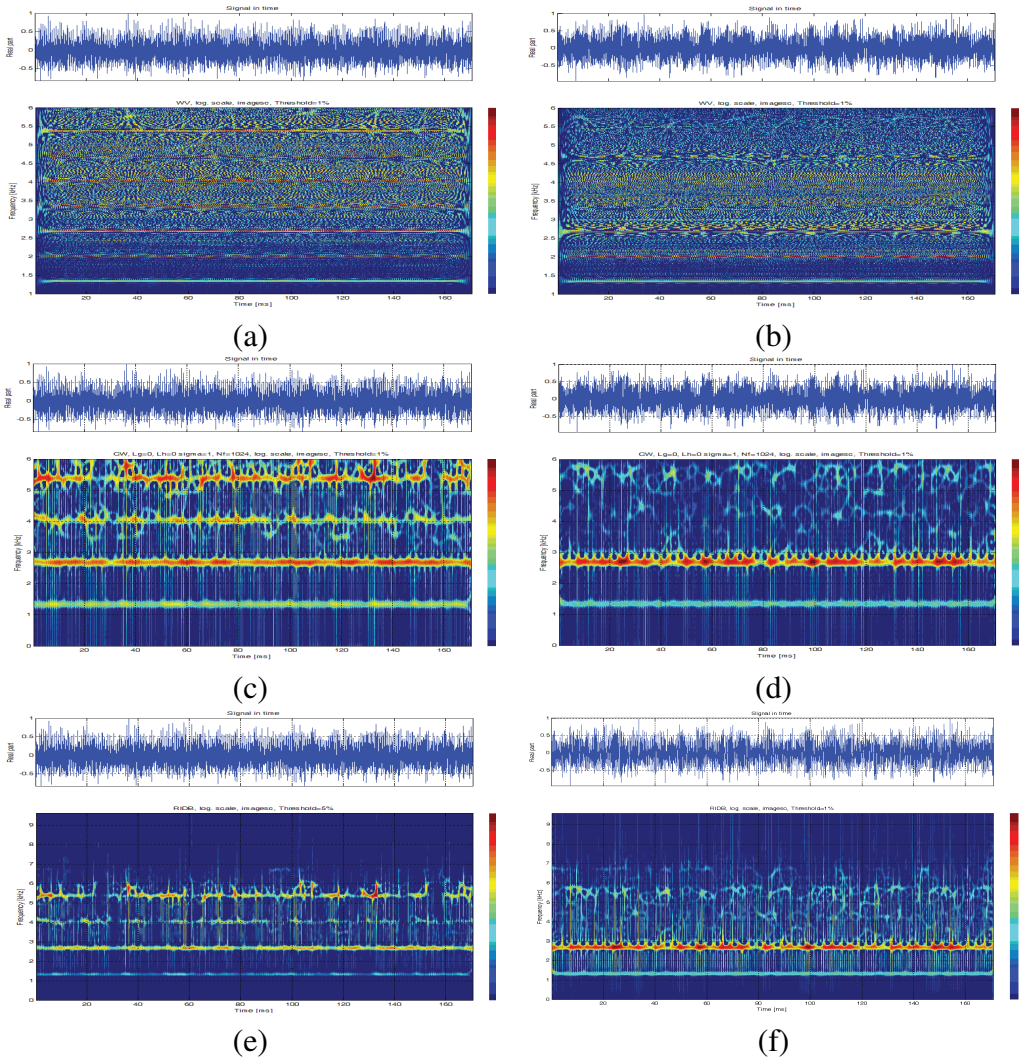

Figure 5.10: Time-frequency distributions of vibration signals from (a) data set 1, and (b) data set 2 with WV distribution, illustrating the potentially negative impact of cross terms in vibration analysis.

compared to that of the reduced interference distributions. From the metric, we can see a higher value for the amount of information as represented by the reduced interference distribution. This can be interpreted similarly to visual inspection of the time-frequency distributions for the respective kernels. By visual inspection of the reduced interference distributions, we see more of the information represented in the transient variations of the signals and less of the cross-terms. The values of these test points (1-10) are randomized within the week long duration of testing approaching failure in our case study, so we will

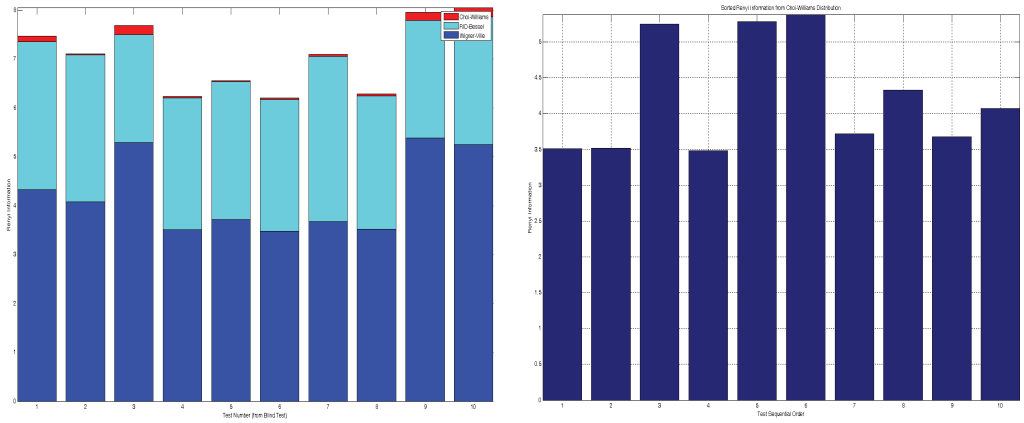

(a) (b)

Figure 5.11: (a) Rényi metric comparison, and (b) sequential sorting of metric for the CW.

now view the sorted version of the same data and consider the metric for a sequential interpretation approaching failure. This will help us view the Rényi information as a metric for condition assessment.

The sequential time-series to failure is shown in Figure 7(b). The bars corresponding to 1, 2, and 4 showcase approximately the same complexity by our metric and all correspond to the start of an experiment run. However, bar number 7 corresponding similarly to the start of an experimental run, shows a significantly higher complexity value while actually decreasing in the number of frequency bands (as seen from Figures 4-6). This corresponds to high amount of frequency transient information caused by the impending failure. Extensive damage was likely caused during the previous runs at the values indicated by high Rényi metric and failure occurred soon after the measurement used for bar 10. Constant increase is seen from bar 3 to 5 to 6 leading up to failure, and it will be interesting in the future to consider sections that have been completely matched in terms of the test sequence (both loading and rotational speed). With the given results, we would suggest using the Rényi metric derived previously to confirm that a part is failing. If the second harmonic of the gear mesh frequency measured here were increasing, we could measure the Rényi based metric and confirm that while the number of frequency bands from 1x of mesh to 4x of mesh frequency is decreasing, the Rényi information is increasing. This would indicate

a high number of transient variations and allow for rejection of some false positives based on the previous metrics of first and second harmonics of gear mesh frequency.

5.4 Analysis of Hanger Bearing Vibration Signals in Baseline Measurements

Comparison of Rényi Derived Self Information to Time-Frequency Methods

The first step of analysis and discussion uses the self Rényi information measure defined in (1.26) of Section 1.4 to describe the individual time series. The self Rényi information measures of S_1 and S_2 for baseline and misaligned cases are provided in Figure 5.12. Signal 1, S_1, and Signal 2, S_2, in both the baseline (A/B) and misaligned (MA/B) cases are processed by applying the 8-point moving average filtering followed by Rényi information calculation to obtain the self information measure. Thus, for every time instance of every experiment window of the data, a Rényi calculation of each auto-correlated signal was gathered. As shown in Figure 5.12, a total of 272 self information measures were gathered for each signal of each case. Additional overlapping is used for x-y coordinate mapping used in visualizing part health. In order to identify the tendency of the measure, an 8-point moving average filter was applied to each signal with the filter covering half of the time instances provided in each experiment window. The results of this self information measure are compared side by side in Figure 5.12 for each signal. The referenced time instance (15th of file frame at 5th experiment window) is marked on each graph to show a consist reference point based on the description of Section 5.1.

Notable difference from the side by side comparison in Figure 5.12 is a sizable increase in the self information measure of the misaligned case over the baseline case. This could be a characteristic signature of a misaligned case. The self information measure shows a general increase at the given samples when comparing the balanced-aligned case with the

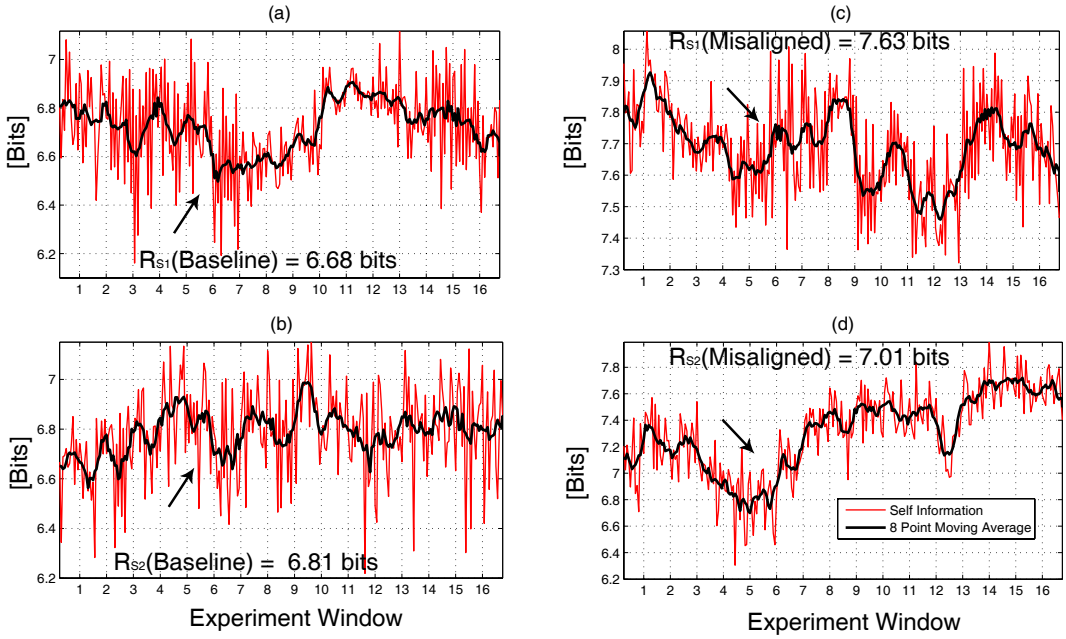

Figure 5.12: Self Rényi information measure of S_1 and S_2 for baseline in (a)∼(b), and self Rényi information measure of S_1 and S_2 for misalignment in (c)∼(d)

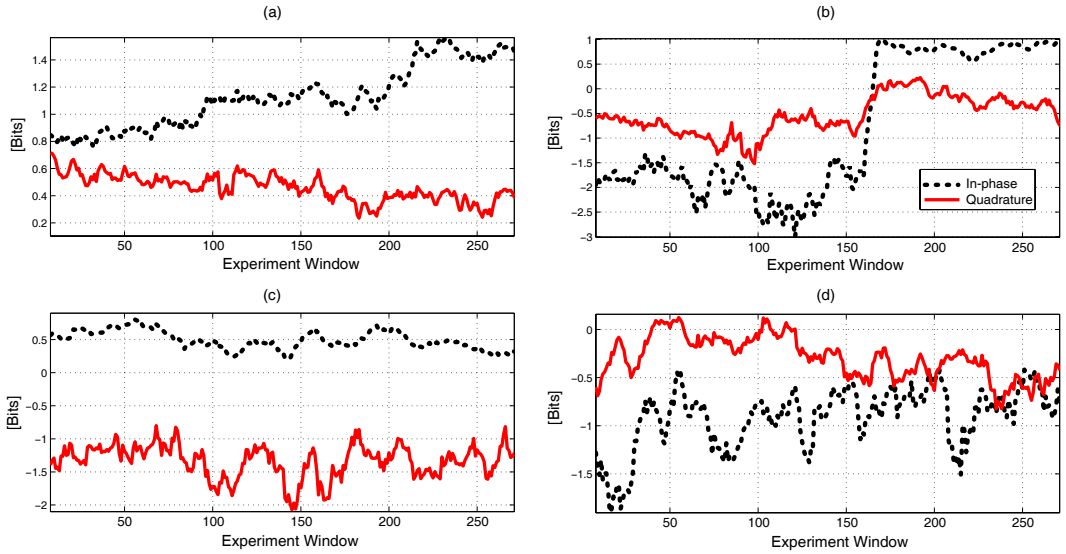

Figure 5.13: Mutual Rényi information measure of S_1 and S_2 for (a) Baseline-Aligned, (b) Aligned-Unbalanced, (c) Misaligned-Balanced, and (d) Misaligned-Unbalanced

misaligned case and an increase on the average of measured frames. The average self information value of the baseline S_1 signal is reported at 6.72 bits while the average value of the same signal in the misaligned-balanced case was 7.68 bits. Comparing the second signal set, S_2, we obtain a value of 6.78 bits compared to 7.31 bits for the same cases. However,

from this derived metric, the interpretation is yet unclear. This self-information measure can be verified using the spectrogram example discussion in Figure 5.4. From this data, there is little other indication of change from the baseline case to another "faulty" status of the shaft. Moreover, the self Rényi information of S_1 in the balanced case in Figure 5.12(a), as well as both signals in the misaligned case, oscillate more compared to the self Rényi information of S_2 of the baseline case (A/B). This could be attributed to more high frequency components shown in the time-frequency spectrogram of Figure 5.4 (b).

While this self information proves useful and shows a notable basis by which to compare data sets, it lacks potential for comparison of closely related signals and in this instance shows an increase when compared on average while not for localized comparison. This only partly supports the desired qualities of a condition indicator while further information can be gathered from the mutual information measure. This mutual information measure is a complex value and can be further subdivided into two constituent values: an in-phase mutual time-frequency information ($I_\alpha(R_{s_1 s_2})$) and a quadrature mutual time-frequency information ($I_\alpha(Q_{s_1 s_2})$) defined in (5.10) and (5.11).

In-Phase and Quadrature Components of the Time-Frequency Mutual Information Measure

Mutual information measures of baseline and misaligned cases are provided in Figure 5.13. An interesting trend can be seen in the baseline case in Figure 5.13(a). Overall, the in-phase mutual time-frequency information ($I_\alpha(R_{s_1 s_2})$) stays mostly at a constant separation from the quadrature mutual time-frequency information ($I_\alpha(Q_{s_1 s_2})$). Both the $I_\alpha(R_{s_1 s_2})$ and $I_\alpha(Q_{s_1 s_2})$ of the baseline case in Figure 5.13(a) remain relatively constant throughout all windows of the experiment. However, toward the end of the sequence outlined in Figure 5.13(a), the in-phase and quadrature mutual information measure values begin to experience a larger separation. These characteristics are all important to note while considering what truly characterizes the baseline physics of the system.

A glance at the mutual information from the misaligned case in Figure 5.13 (b) draws attention to two distinctive signatures. First, like the baseline case, the co-spectral mutual time-frequency information ($I_\alpha(R_{s_1 s_2})$) remains relatively constant throughout all experiment windows with a large trough around experiment window 10 corresponding to a minimum value of the quad-spectral mutual time-frequency information ($I_\alpha(Q_{s_1 s_2})$). Second, the quadrature component has a larger average value over the length of the experiments than was seen in the quad-spectral component in the baseline case. Also, the quad-spectral component in the misaligned case fluctuates greatly, showing greater amounts of local minima and maxima. Though the quad-spectral information in the misaligned case revealed a significant rise in the number of bits in the mutual information measure, the co-spectral portion showed little increase over the experiment windows measure. By comparing the results in Figure 5.13 with other results by classical spectral analysis or traditional spectrogram, one can find the usefulness of the proposed technique for a quantitative health condition assessment of the experimental setup. Further analysis is underway to understand the relationship between the time-frequency mutual information method and other confounding factors such as speed and torque, isolating the sources of transient changes in the vibration signatures.

Time-Frequency Mutual Information Measure Visualization

The mutual information measure currently in development and shown in Figure 5.14 provides a graphical interpretation of part condition by analyzing the amount of mutual data shared between two vibration signals received from separate accelerometers. The mutual information measure is comprised of a quadrature component and an in phase component which, by observation seem to indicate differences in the actual physics of the system. Figure 5.14 shows the scatter plot distribution of the in phase component of the measure on the x-axis and the quadrature component of the measure on the y-axis. In the condition of system unbalance, as seen in Figure 5.14 (a), (c), and (d), which compare misaligned and

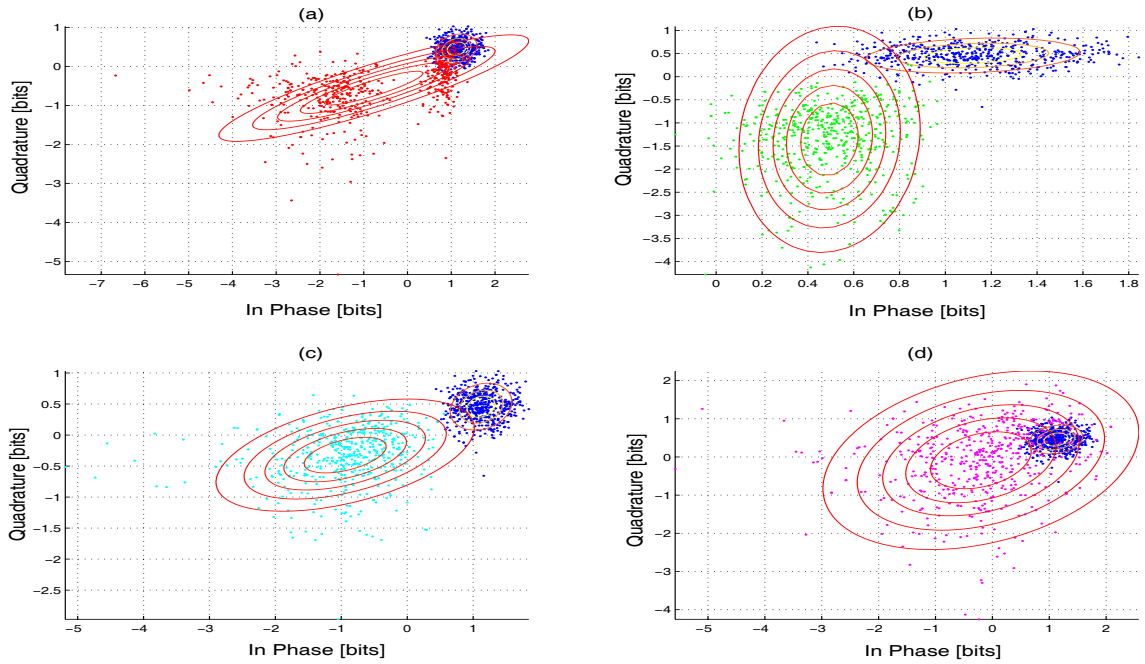

Figure 5.14: Baseline comparisons of the mutual information measure (a) Aligned-Unbalanced, (b) Misaligned-Balanced, (c) Misaligned-Unbalanced 3-5, and (d) Misaligned-Unbalanced 4-5 with the Aligned-Balanced Case

unbalanced experimental settings to the standard baseline, the in-phase component shows a potential trend toward a decrease in information bits.

Similarly, misalignment can be observed to decrease the number of information bits of the measure contained in the quadrature component, provided in Figure 5.14 (b) and (d). As a distribution these values can be seen to shift along the x-y plane indicating a shift in part or system status. Additional studies should be analyzed and compared to determine if these trends are truly linear as they appear to be from observation. It would appear that Figure 5.14 (c) and (d) which were tested under both misalignment and unbalance conditions, as well as combination settings, have differing degrees of misalignment and unbalance yielding different distributions which follow the established trends along the quadrature and in phase components.

Mutual Information Based Condition Indicator for Drivetain Health Monitoring

Included in Table 5.4 is reference for the statistics related to both spectra of the mutual information measure proposed. Future studies of this indicator method could focus on varying states of misalignment and unbalance to determine a quantifiable relation between the x-y distribution shift and part health. Differences in this mutual information measure can be further developed into an increased precision statistical indicator of part or system health status.

Table 5.4: Statistical Summary of Mutual Information Measure

Statistical Parameter		Baseline	Aligned-UB	Misalign - Balanced	Misaligned-Unbalanced 3-5	Misaligned-Unbalanced 4-5
Mean μ	*In Phase*	1.1202	-0.7424	0.4902	-0.9535	-0.1753
	Quad	0.4535	-0.551	-1.3691	-0.3268	-0.0726
STD σ	*In Phase*	0.0837	1.8258	0.2147	1.0136	1.4344
	Quad	0.2324	0.7107	1.3228	0.4852	1.2363
Correlation ρ		0.2326	0.8732	0.0891	0.4005	0.3188

This metric can be used in the fusion of other types of sensors in order to obtain extended information for more accurate assessment of the health status of components. Data can be gathered from vibration, acoustic, and temperature sensors and correlated to present a single, more robust, health indicator [49], [50]. Furthermore, analysis of these values can yield great insights into the physics behind systems such as the system under study which provided the mechanical vibration data, providing either a simple summary of component health for an operator or a complex interpretation from a knowledgeable engineer in order to fully achieve condition-based maintenance.

5.5 CONCLUSIONS

In this project, two sets of vibration signals have been analyzed with four different kernels - WV, CW, RID, and ZAM distributions. For these vibration signal analyses in time-frequency domain, WV shows some cross terms which are reduced with CW, RIDB, and ZAM distributions. We have shown which frequency components are responsible for the vibration introduced by the mechanical components in the test bed system as well. In addition to this, comparison of time-frequency distributions it is possible to identify which component is in an advanced stage and which component is potentially damaged. Moreover, from Rényi information it can be concluded which time-frequency distribution provides more information for the vibration signal analysis. Based on all the analyses provided in this project, necessary steps can be taken for health improvement of components in order to avoid premature failure.

Drawing from Rényi complexity measures and mutual information theory, baseline, unbalanced, and misaligned experimental settings are quantitatively distinguished by the proposed mutual information technique. Statistical analysis of the time-frequency information measure from Table 5.4shows a variance in the proposed in-phase and quadrature information measures of 0.0070 (STD of 0.0837) and 0.0054 (STD of 0.2324) respectively for baseline testbed conditions in opposition to an increased in-phase information measure variance of 3.33 (STD of 1.8258) in repeated unbalanced test cases and increased quadrature information measure of 1.7497 (STD of 1.3228) in repeated misaligned cases. With unbalance quantifiable by variance in the in-phase mutual information and misalignment quantifiable by variance in the quadrature mutual information, machine health classification can be accomplished using statistical bounding regions. The baseline is characterized with a constant separation on a per-time instance basis of the mutual information measure. The misaligned case may be characterized by its quadrature component, showing the misalignment in an increased number of bits from the information measure.

BIBLIOGRAPHY

[1] A. Bayoumi, et. al., "Integration of Maintenance Management Systems and Health Monitoring Systems through Historical Data Investigation," *Technical Specialists' Meeting on Condition Based Maintenance*, Huntsville, AL, 2008.

[2] A. Bayoumi, et al., "Implementation of CBM through the Application of Data Source Integration," *Technical Specialists' Meeting on Condition Based Maintenance*, Huntsville, AL, 2008.

[3] A. Bayoumi, et. al.,"Examination and Cost-Benefit Analysis of the CBM Process," *Technical Specialists' Meeting on Condition Based Maintenance*, Huntsville, AL, 2008.

[4] A. Bayoumi, et. al., "Aircraft Components Mapping and Testing for CBM," *Technical Specialists' Meeting on Condition Based Maintenance*, Huntsville, AL, 2008.

[5] J.W. Hines, J.J. Garvey, J. Preston, A. Usynin, "Empirical Methods for Process and Equipment Prognostics," *Reliability and Maintainability Symposium*, 2007.

[6] W. Weibull, "A statistical distribution of wide applicability," *Journal of Applied Mechanics Transactions*, ASME, vol. 18, no. 3, pp. 293-297, 1951.

[7] J. Coble, *Merging Data Sources to Predict Remaining Useful Life âĂŞ An Automated Method to Identify Prognostic Parameters*, Doctoral Dissertation, The University of Tennessee, Knoxville, Tennessee, 2010

[8] C.J. Lu, W. Meeker, "Using Degradation Measures to Estimate a Time-to-Failure Distribution," *Technometrics* vol. 35, no. 2, pp. 161-174, 1993

[9] G. Yang, *Life Cycle Reliability Engineering,* John Wiley and Sons, Hokoken, NJ, 2007.

[10] Abdel-Moez E. Bayoumi, William Ranson, Lester Eisner, Lemuelle Grant, "Cost and Effectiveness Analysis of the AH-64 and UH-60 On-Board Vibrations Monitoring System," *Aerospace Conference-IEEE*, Big Sky, Montana, March 2005.

[11] Tanzina Zaman, Abdel E. Bayoumi, "Analysis of Health and Usage Monitoring System (HUMS) Users' Perspective towards Mission Benefits Using Regression Analysis." *Proceedings of AHS 70th Annual Forum*, May 20-22, 2014.

[12] Erin L. Ballentine, Adam D. Miracle, Abdel E. Bayoumi, Michele K. Platt, Lester Eisner. "Return on Investment: Analysis of Benefits of the Implementation of Elastomeric Wedges as Vibration Control on the Apache (AH-64D) Aircraft." *AHS Airworthiness, CBM, and HUMS Specialists' Meeting*, Feb 2013.

[13] Mohammed A. Hassan, David Coats, Kareem Gouda, Yong-June Shin, Abdel Bayoumi. "Analysis of Nonlinear Vibration-Interaction Using Higher Order Spectra to Diagnose Aerospace System Faults," *IEEE Aerospace Conference*, April 2012.

[14] Mohammad A. Hassan, David Coats, Yong-June Shin, Abdel-Moez Bayoumi, Alexander Barry. "Bicoherence Analysis for Condition Assessment of Multi-Faulted Helicopter Drivetrain Systems." *Proceedings of the AHS International 68th Annual Forum and Technology Display*, May 2012.

[15] Mohammed A. Hassan, David Coats, Yong-June Shin, Abdel E. Bayoumi, "Quadratic-Nonlinearity Power-Index Spectrum and Its Application in Condition Based Maintenance (CBM) of Helicopter Drive Trains." *IEEE International Instrumentation and Measurement Technology Conference*, May 13-16, 2012.

[16] Mohammed A. Hassan, Abdel E. Bayoumi, Yong-June Shin. "Quadratic-Nonlinearity Index Based on Bicoherence and Its Application in Condition Monitoring of Drive-Train Components," *IEEE Transactions on Instrumentation and Measurement*, vol. 63, no. 3, pp. 719 - 728, Mar. 2014.

[17] Ignacio Santamaría-Caballero, Carlos J. Pantaleón-Prieto, Jesús Ibáñez-Díaz, Enrique Gómez-Cosío, "Improved procedures for estimating amplitudes and phases of harmonics with application to vibration analysis," *IEEE Transactions on Instrumentation and Measurement*, vol. 47, no. 1, Feb. 1998, pp. 209 - 214.

[18] Giovanni Betta, Consolatina Liguori, Alfredo Paolillo, Antonio Pietrosanto, "A DSP-based FFT-analyzer for the fault diagnosis of rotating machine based on vibration analysis," *IEEE Transactions on Instrumentation and Measurement*, vol. 51, no. 6, Dec. 2002, pp. 1316 - 1322.

[19] Jaidilson Jó da Silva, Antonio Marcus Nogueira Lima, Franz Helmut Neff, José Sérgio da Rocha Neto "Non-invasive fast detection of internal fouling layers in tubes and ducts by acoustic vibration analysis," *IEEE Transactions on Instrumentation and Measurement*, vol. 58, no. 1, Jan. 2009, pp. 108 - 114.

[20] Paul Grabill, Jason Seale, Dariusz Wroblewski, Tom Brotherton. "iTEDS: the intelligent Turbine Engine Diagnostic System" *48th International Instrumentation Symposium*, pp. 6.

[21] Marc Vedrines, Vincent Gassmann, Dominique Knittel, "Moving web-tension determination by out-of-plane vibration measurements using a laser," *IEEE Transactions on Instrumentation and Measurement*, vol. 58, no. 1, Jan. 2009, pp. 207 - 213.

[22] Ruqiang Yan, Robert X. Gao, "Complexity as a measure for machine health evaluation," *IEEE Transactions on Instrumentation and Measurement*, vol. 53, no. 4, Aug. 2004, pp. 1327 - 1334.

[23] J. Banks, T. Bair, K. Reichard, D. Blackstock, D. McCall, J. Berry, "A Demonstration of a Helicopter Health Management Information Portal for U.S. Army Aviation," *Proceedings of the IEEE Aerospace Conference*, Big Sky, MT 2005. pp. 3748-3755.

[24] S. Santhi, V. Jayashankar, "Time-frequency analysis method for the detection of winding deformation in transformer," *Proceedings of the IEEE Transmission and Distribution Conference and Exposition*, Chicago, IL, 2008. pp. 1-5.

[25] Satish Rajagopalan, José A. Restrepo, José M. Aller, Thomas G. Habetler, Ronald G. Harley, "Nonstationary motor fault detection using recent quadratic time frequency representations," *IEEE Transactions on Industry Applications*, vol. 44, no. 3, May/Jun. 2008, pp. 735 - 744.

[26] Kwang Ik Cho, David Coats, John Abrahms, Nicholas Goodman, Yong-June Shin, Abdel Bayoumi, "Applications of Time-Frequency Analysis for Aging Aircraft Component Diagnostics and Prognostics," *Proceedings of SPIE-Advanced Signal Processing Algorithms, Architectures, and Implementations XVIII*, San Diego, CA, July 2008.

[27] Andrew R. Scott, "Characterizing system health using modal analysis," *IEEE Transactions on Instrumentation and Measurement*, vol. 58, no. 2, Feb. 2009, pp. 297 - 302.

[28] Ruqiang Yan, Robert X. Gao, "Hilbert-Huang transform-based vibration signal analysis for machine health monitoring," *IEEE Transactions on Instrumentation and Measurement*, vol. 55, no. 6, Dec. 2006, pp. 2320 - 2329.

[29] T. Cover and J. Thomas, Elements of Information Theory New York: Wiley, 1991.

[30] D. Coats, K. Cho, Y.J. Shin, N. Goodman, V. Blechertas, A.E. Bayoumi, "Advanced Time-Frequency Mutual Information Measures for Condition-Based Mainte-

nance of Helicopter Drivetrains,"*IEEE Transactions on Instrumentation and Measurement*, vol.60, no.8, pp.2984-2994, Aug. 2011.

[31] Hamming, R. W. and Tukey, J. W. "Measuring Noise Color." Unpublished memorandum, 1949.

[32] Blackman, R. B. and Tukey, J. W. "Particular Pairs of Windows." *In The Measurement of Power Spectra, From the Point of View of Communications Engineering*. New York: Dover, pp. 98-99, 1959.

[33] W. J. Williams, M. L. Brown, and A. O. Hero, "Uncertainty, information, and time-frequency distributions," in *Proceedings of SPIE-Advanced Signal Processing Algorithms, Architectures, and Implementations X*, vol. 1566, 1991, pp. 144-156.

[34] T.-H. Sang and W. J. Williams, "Rényi information and signal-dependent optimal kernel design," in *Proc. IEEE Int. Conf. Acoustics, Speech, and Signal Processing ICASSP '*95, vol. 2, 1995, pp. 997-1000.

[35] L. Cohen, "*Time-Frequency Signal Analysis*," Prentice Hall, New York, 1995.

[36] Leon Cohen, "Time-frequency distributions - a review," *Proceedings of the IEEE*, Vol.77, July, 1989, pp. 941-981.

[37] Y. Zhao, L. E. Atlas, and R. J. Marks, "The use of cone-shaped kernels for generalized time-frequency representation of nonstationary signals," *IEEE Trans. Acoust., Speech, Signal Processing,* vol. 38, pp. 1084-1091, 1990.

[38] "Standard for Nuclear Power Plants - Instrumentation and control important to safety - Electrical equipment condition monitoring methods - Part 3: Elongation at break," IEEE P62582-3/FDIS, September 2012 , vol., no., pp.1,27, Sept. 15 2012

[39] Anandakumaran, K., "Aging and condition monitoring studies of composite insulation cables used in nuclear power plants," Dielectrics and Electrical Insulation, IEEE Transactions on , vol.14, no.1, pp.227,237, Feb. 2007

[40] L. R. Mason, A. B. Reynolds, "Standardization of oxidation induction time testing used in life assessment of polymeric electric cables," *Journal of Applied Polymer Science* vol. 66, no. 9, pp. 1691âĂŞ1702, 28 November 1997

[41] Fei Liu; Xingyi Huang; Jing Wang; Pingkai Jiang, "Insulation ageing diagnosis of XLPE power cables under service conditions," *Condition Monitoring and Diagnosis (CMD), 2012 International Conference on* , vol., no., pp.647,650, 23-27 Sept. 2012

[42] Byun, D. G.; Shin, H. T.; Kim, W.J.; Shin, J.Y.; Hong, J.W., "Insulation deterioration diagnosis on ultra high voltage power cables," *Properties and Applications of Dielectric Materials, 2003. Proceedings of the 7th International Conference on* , vol.1, no., pp.179,182 vol.1, 1-5 June 2003

[43] J. Mendel, "Fuzzy logic systems for engineering: a tutorial," *Proceedings of the IEEE*, Vol. 83(3), pp. 345-377, March, 1995.

[44] "Fuzzy control programming" Technical report, *International Electrotechnical Commision*, 1997.

[45] R.G. Baraniuk, P. Flandrin, A. Janssen, and O. Michel, "Measuring time-frequency information content using the Renyi Entropies," *IEEE Transactions on Information Theory*, vol. 47, no. 4, May 2001, pp 1391-1409.

[46] Yong-June Shin, E. J. Powers, and W. M. Grady, "On definition of cross time-frequency distribution function," *Proceedings of SPIE-Advanced Signal Processing Algorithms, Architectures, and Implementations X*, San Diego, CA, July 2000. pp. 9-16.

[47] Bin Zhang, et al, "Application of blind deconvolution denoising in failure prognosis," *IEEE Transactions on Instrumentation and Measurement*, vol. 58, no. 2, Feb. 2009, pp. 303 - 310.

[48] *IEEE Standard*-1064-1991, "Guide for Multifactor Stress Functional Testing of Electrical Insulation Systems," 1991.

[49] Michael E. Stieber, Emil Petriu, George Vukovich, "Instrumentation architecture and sensor fusion for systems control," *IEEE Transactions on Instrumentation and Measurement*, vol. 47, no. 1, Feb. 1998, pp. 108 - 115.

[50] Stephen C. Stubberud, Kathleen A. Kramer, "Data association for multiple sensor types using fuzzy logic," *IEEE Transactions on Instrumentation and Measurement*, vol. 55, no. 6, Dec. 2006, pp. 2292 - 2303.

[51] P. Loughlin, G. Bernard, "Cohen-Posch (Positive) Time-frequency Distributions and Their Application to Machine Vibration Analysis," *Mech. Syst. Signal Proc.*, 11(4), 561-576, 1997.

[52] S. Shah, A. El-Jaroudi, P. Loughlin, L. Chaparro, "Signal Synthesis and Positive Time-frequency Distributions," J. Franklin Inst., 337, 317-328, 2000.

[53] Y. J. Shin, E. J. Powers, T. S. Choe, C. Y. Hong, E. S. Song, J. G. Yook, J. B. Park, "Application of Time-Frequency Domain Reflectometry for Detection and Localization of a Fault on a Coaxial Cable," *IEEE Transactions on Instrumentation and Measurement*, Vol. 54, No. 6, Dec. 2005.

[54] J. Wang, P. Crapse, Y. J. Shin, and R. Dougal, "Diagnostics and Prognostics of Electric Cables in Ship Power Systems via Joint Time-Frequency Domain Reflectometry," *Proceedings of the IEEE Instrumentation and Measurement Technology Conference*, May 2008, pp. 917-921.

[55] J. Wang, P. Crapse, Y. J. Shin, and R. Dougal, "Diagnostics and Prognostics of Electric Cables in Nuclear Power Plants via Joint Time-Frequency Domain Reflectometry," *IEEE International Symposium on Electrical Insulation*, Jun. 2008, pp. 24-27.

[56] J. Wang, P.E.C. Stone, D. Coats, Y.J. Shin, R.A. Dougal, "Health Monitoring of Power Cable via Joint Time-Frequency Domain Reflectometry," *Instrumentation and Measurement, IEEE Transactions on*, vol.60, no.3, pp.1047-1053, March 2011.

[57] Brian Drost, Michael Mastrianni, Bruce Thompson, "Aircraft Wire Fault Detection and Isolation using Spread Spectrum Time Domain Reflectometry" American Helicopter Society Forum 70, May 2014.

[58] L. Cohen, "Time-frequency distributions - a review," *Proc. IEEE*, Vol.77, pp. 941-981, July, 1989.

[59] Naik, S.; Furse, C.M.; Farhang-Boroujeny, B., "Multicarrier reflectometry," *Sensors Journal, IEEE*, vol.6, no.3, pp.812,818, June 2006.

[60] Smith, P.; Furse, C.; Gunther, J., "Analysis of spread spectrum time domain reflectometry for wire fault location," *Sensors Journal, IEEE*, vol.5, no.6, pp.1469,1478, Dec. 2005.

[61] Griffiths, L.A.; Parakh, R.; Furse, C.; Baker, B., "The invisible fray: a critical analysis of the use of reflectometry for fray location," Sensors Journal, IEEE , vol.6, no.3, pp.697,706, June 2006.

[62] Cynthia Furse, You Chung Chung, Chet, Lo, Praveen Pendayala; "A Critical Comparison of Reflectometry Methods for Location of Wiring Faults," *Smart Structures and Systems*, vol. 2, no.1, 2006, pp. 25-46.

[63] K. Anandakumaran, W. Seidl and P. V. Castaldo, "Condition Assesment of Cable Insulation Systems in Operating Nuclear Power Plants," *IEEE Transactions on Dielectrics and Electrical Insulation*, Vol. 6 No. 3, Jun. 1999.

[64] A. Al-Arainy, Nazar H. Malik, Mohammed Iqbal Qureshi, and Mohammed Nabih Al-Saati, "The Performance of Strippable and Bonded Screened Medium-Voltage XLPE-Insulated Cables Under Long-Term Accelerated Aging," *IEEE Transactions on Power Delivery*, VOL. 22, NO. 2, Apr. 2007.

[65] S. B. Dalal, R. S. Gorur, "Aging of Distribution Cables in Service and Its Simulation in the Laboratory," *IEEE Transactions on Dielectrics and Electrical Insulation*, Vol. 12 No. 1, Feb. 2005.

[66] B. K. Hwang, "A New Water Tree Retardant XLPE," *IEEE Trans. On Power Delivery*, Vol. 5, No. 3, May/June 1990, pp. 1617-1627.

[67] X. Qi and S. Boggs, "Thermal and Mechanical Properties of EPR and XLPE Cable Compounds," *IEEE Electrical Insulation Magazine*, Vol. 22, No. 3, May/June 2006, pp. 19-24.

[68] R. Bartnikas, K. D. Srivastava, "Power and Communication Cables Theory and Applications," *IEEE Press Series on Power Engineering*, Wiley January 2003, pp. 134-137

[69] J. P. Crine, "A Molecular Model for the Electrical Aging of XLPE," *Int. Conf. on Electrical Insulation and Dielectric Phenomena* 2007, October 2007, pp. 608-610.

[70] J. P. Crine, "Electrical Aging and Breakdown of XLPE Cables," *IEEE Trans. On Dielectric and Electrical Insulation*, October 2002, pp. 23-26.

[71] A. Sommerfeld, "Transmission of electrodynamic waves along a cylindrical conductor," *Annalen der Physik und Chemie*, vol. 67, pp. 233âĂŞ290, 1899.

[72] J. Zenneck, "On the propagation of plane electromagnetic waves along a planar conductor surface and its relationship to wireless telegraphy," *Annalen der Physik*, series 4, vol. 23, pp. 848âĂŞ866, 1907.

[73] G. Goubau, "Surface waves and their application to transmission lines," *J. Applied Physics*, vol. 21, pp. 1119âĂŞ1128, 1950.

[74] G. E. Elmore, "System and apparatus for transmitting a surface wave over a single conductor," US patent 7567154B2, July 2009.

[75] M. N. Alam, R. H. Bhuiyan, R. Dougal, M. Ali, "Novel Surface Wave Exciters for Power Line Fault Detection and Communications," *IEEE Antennas and Propagation Society International Symposium*, Spokane, WA, July 2011.

[76] Md. N. Alam, R.H. Bhuiyan, R. Dougal, and M. Ali, "Design and Application of Surface Wave Sensors for Non-Intrusive Power Line Fault Detection," *IEEE Sensors Journal*, 2011 (submitted).

[77] R. Bhuiyan, *Proximity Coupled Non-Intrusive Wireless Sensors for Monitoring and Diagnostics*, Ph.D. Dissertation, University of South Carolina, 2010.

[78] M. Ali, R.H. Bhuiyan, and R. Dougal, *Conformal Surface Wave Injector Device for Application in Non-intrusive Cable Fault Detection and Broadband Power Line (BPL) Communication*, 2011. (patent pending).

[79] Millane, R.P., Eads, J.L; "Polynomial approximations to Bessel functions." *Antennas and Propagation, IEEE Transactions on*, vol. 51, no. 6, pp. 1398-1400, June, 2003.

[80] Rothwell, E.J.;"Exponential Approximations of the Bessel Functions I0,1(x), J0,1(x), Y0(x), and H01,2(x), with Applications to Electromagnetic Scattering, Radiation, and Diffraction [EM Programmer's Notebook]." *Antennas and Propagation Magazine*, IEEE no. 3 pp.138-147, June 2009.

APPENDIX A

SMART WIRING GUI OVERVIEW

The smart wiring graphical user interface is the MATLAB program developed at the University of South Carolina for TDR, FDR, and JTFDR. The left most portion of the GUI shown in Figure A.1 is used to select input parameters for the optimal reference. Most important here is the set of chirp signal parameters and the selection of envelope type and chirp type. Chirp parameters include center frequency, bandwidth, and time duration and upon selecting and saving these parameters, the uncertainty principle or time-bandwidth product is calculated for the reference signal. The GUI will provide a red highlighted value if the chirp signal parameters produce a time-bandwidth product below 0.5, a scalar value. Next, the envelope type portion of the GUI allows selections for the chirp signal which include gaussian, derivative of gaussian, and no enveloping function (essentially a linear chirp for use in FDR measurements). Chirp options include linear chirp, exponential chirp, modulated chirp, and no chirp rate or just the envelope. This last option allows for TDR by use of a gaussian or other window function in the time domain only. Once signal options have been selected, the user can generate the signal and see an example of what the signal looks like on the reference signal axis.

Once the reference signal properties have been fully defined, oscilloscope parameters can be adjusted on the left portion of the screen including range, position of reference, delay, number of points in acquisition, sampling rate, voltage scale of the oscilloscope measurements, and the oscilloscope load selection. Pressing the data acquisition button on the right collects the data from the oscilloscope probe channels or incident and reflected signals while a custom routine of data acquisition can be selected with the “Run Routine”

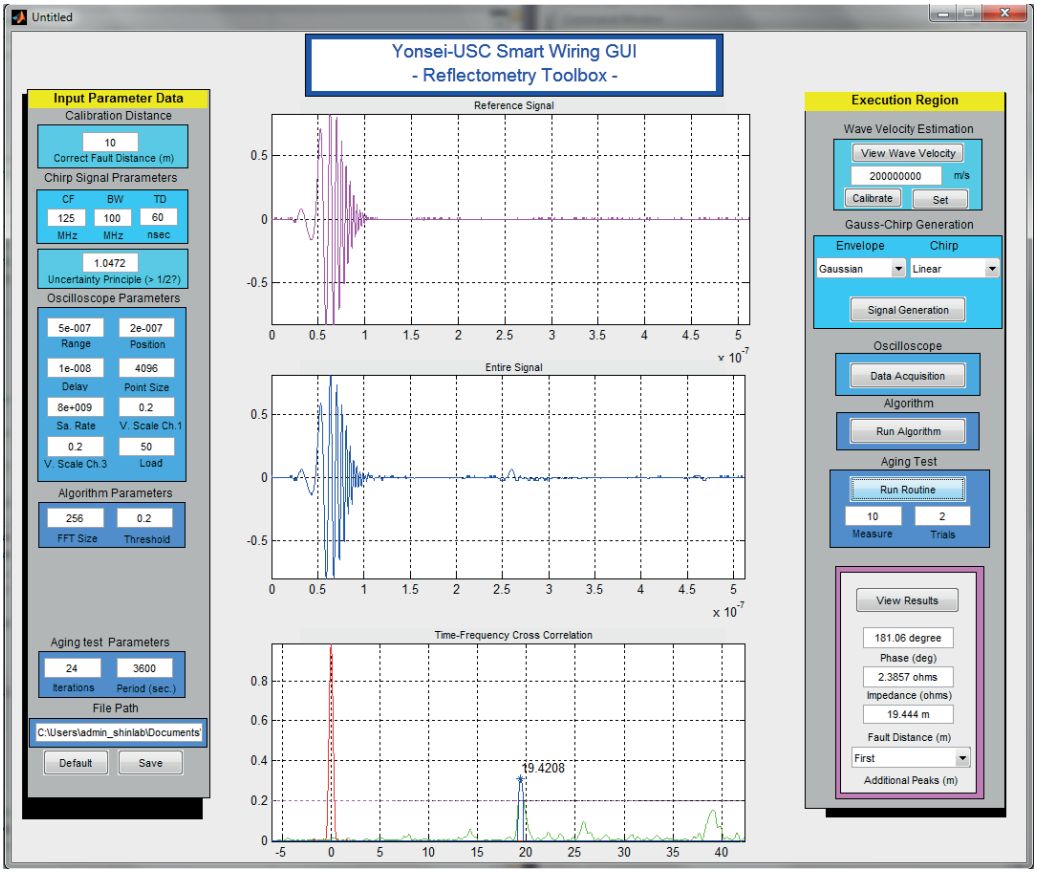

Figure A.1: Graphical user interface of the smart wiring program.

button with a user selected number of data acquisition repetitions. The reference signal axis and the entire signal axis of the MATLAB GUI will then be updated with the most current data from the oscilloscope. Running the time-frequency cross-correlation (TFCC) algorithm then provides a means of assessing defect severity and location using advanced signal processing.

The third or bottom-most axis is where the TFCC graph resides. Algorithm parameters include the FFT size for spectrogram computation of windowed FFTs and a threshold for filtering the output TFCC metric. The output here is on the same time scale as the incident and reflected waveforms, however, it is scaled by the propagation velocity of the cable provided in the execution region. The graph here plots the auto-correlation of the reference signal in red and the cross-correlation of the incident and reflected signal above the user-defined threshold in blue. Additionally, the subthreshold TFCC values are shown in green

and maximum peaks above the threshold are labeled by blue markers. These maximum peak values are scaled by the propagation velocity and the location value is labeled on the graph. After the TFCC algorithm has been computed using the "Run Algorithm" button, the results of fault distance estimation, impedance assessment and phase, and additional peak values can be viewed in the bottom right hand corner of Figure A.1.

APPENDIX B

AUTOMATED DETERMINATION OF OPTIMAL REFERENCE - MEMBERSHIP FUNCTIONS FOR FUZZY LOGIC

In sections 2.4 and 2.5 of Chapter 2, the determination of the optimal reference for JTFDR was automated using a set of fuzzy logic inference rules. The rules provided in 2.1 listed the important factors in determining the optimal reference in terms of "fuzzified" variables. These variables were derived by use of gaussian membership functions and the range of each membership function was tuned to best emulate the choices an operator would use when selecting the reference signal. Figures B.1 - B.6 show the exact range definitions for the parameters used in selecting the best reference signal. Labels are given for each gaussian distribution forming a membership function. The ideal condition for each case is typically highlighted in each figure, however, some parameters (such as correct cable estimation distance or attenuation) vary based on cable length or cable type.

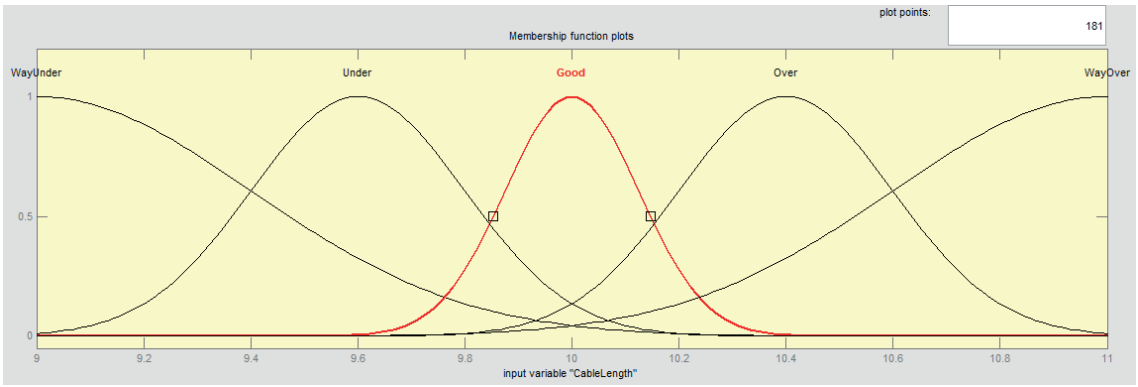

Figure B.1: Membership function for the estimated cable length from JTFDR for a baseline cable sample.

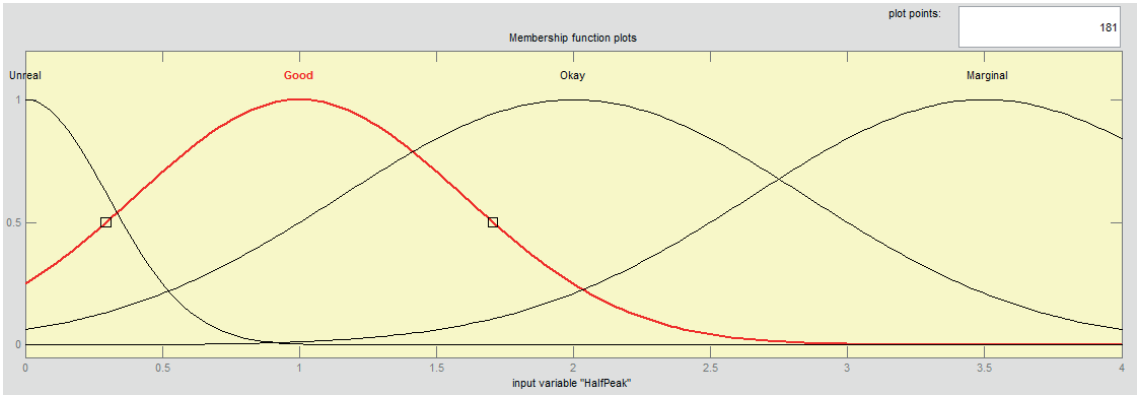

Figure B.2: Membership function for the peak width resolution of TFCC peaks for a baseline cable sample.

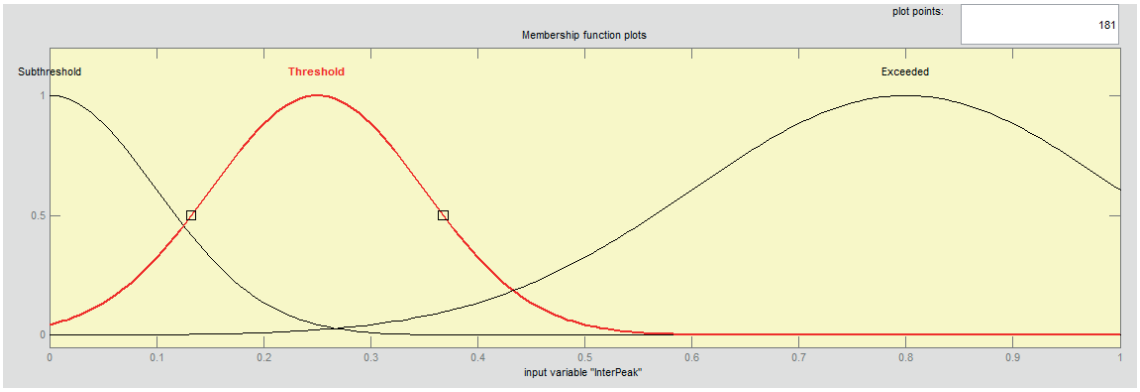

Figure B.3: Membership function for the summation of the noise or false peaks between reflection at the end of a baseline cable sample.

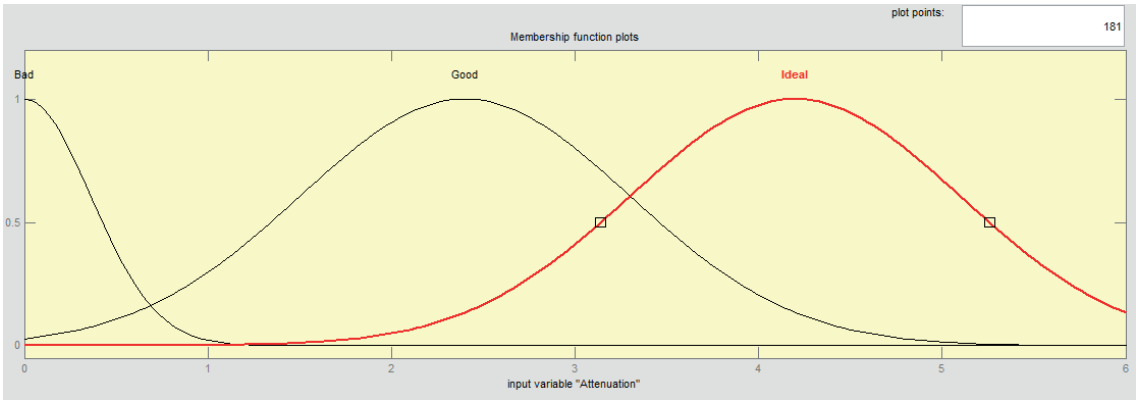

Figure B.4: Membership function for the number of reflections of the end of a baseline cable sample measurable by JTFDR above a user specified threshold.

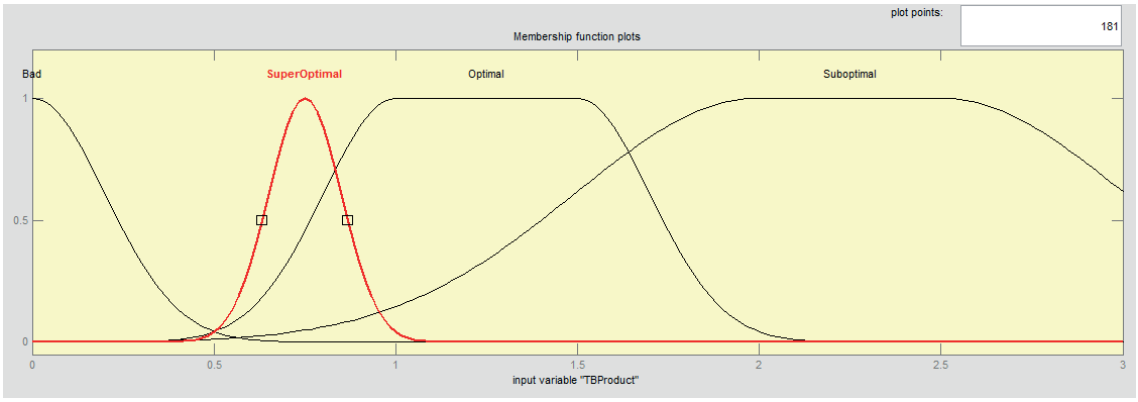

Figure B.5: Membership function for the time-bandwidth product obtained for a given time duration, bandwidth and center frequency of the optimal reference signal.

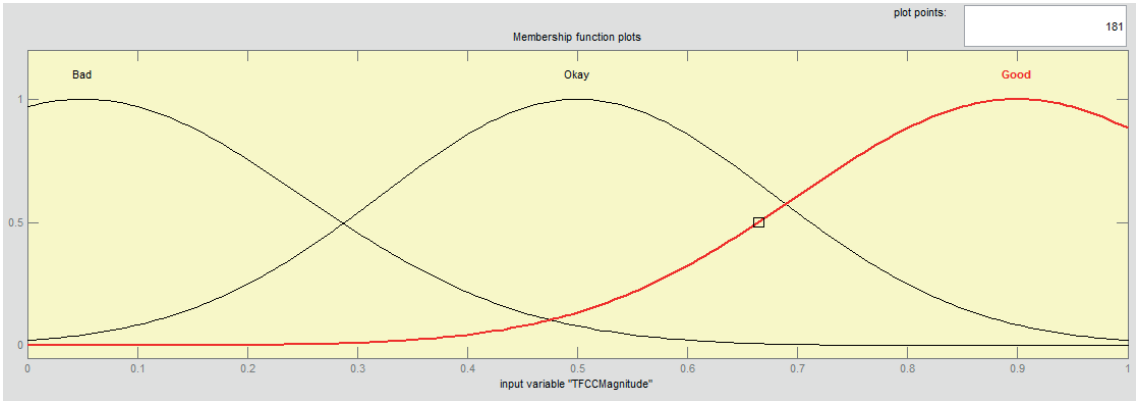

Figure B.6: Membership function for the time-frequency cross correlation magnitude at the end of a baseline cable sample.